escola superior de tecnologia e gestão
instituto politécnico de leiria

DISSERTAÇÃO

Mestrado em Engenharia Eletrotécnica - Eletrónica e Telemocmunicações

Simulation framework for multigigabit applications at 60 GHz

PEDRO ALEXANDRE SEABRA PIRES

Leiria, março de 2017

MASTER DISSERTATION

Electrical Engineering - Electronics and Telecommunications

Simulation framework for multigigabit applications at 60 GHz

PEDRO ALEXANDRE SEABRA PIRES

Master dissertation performed under the guidance of Professor Rafael Ferreira da Silva Caldeirinha of Escola Superior de Tecnologia e Gestão of Instituto Politécnico de Leriria and Rodolfo Vitorino Gomes of University of South Wales, UK.

Leiria, March 2017

Acknowledgments

I would like to thank to everyone that help during this work, and that make it possible to accomplish.

I would like to express my gratitude to my advisers Professor Rafael Ferreira da Silva Caldeirinha and Rodolfo Vitorino Gomes, that guided me in this project. I am thankful for their guidance and availability that were essential for the conduct of this work. I also would like to thank to the research group of Antennas and Propagation from the Instituto de Telecomunicações de Leiria for sharing their knowledge that help this research work.

I want to thank the opportunity of working as researcher in this project that had an important role in my professional an personal progress, and to thank Instituto de Telecomunicações and Escola Superior de Tecnologia e Gestão of IPL, for the laboratory facilities, that gave me conditions to accomplish this work.

Finally, I also want to express my gratitude to my parents, Arlindo and Maria, and brothers Diogo, Alexandre and sister Sara to whom I owe all that I have become. Thank you for being there, without you all my accomplishments would not be possible.

Abstract

This dissertation describes the implementation of a OFDM-based simulation framework for multigigabit applications at 60 GHz band over indoor multipath fading channels. The main goal of the framework is to provide a modular simulation tool designed for high data rate application in order to be easily adapted to a specific standard or technology, such as 5G. The performance of OFDM using mmWave signals is severely affected by non-linearities of the RF front-ends. This work analyses the impact of RF impairments in an OFDM system over multipath fading channels at 60 GHz using the proposed simulation framework. The impact of those impairments is evaluated through the metrics of BER, CFR, operation range and PSNR for residential and kiosk scenarios, suggested by the standard for LOS and NLOS. The presented framework allows the employment of 16 QAM or 64 QAM modulation scheme, and the length of the cyclic prefix extension is also configurable. In order to simulate a realistic multipath fading channel, the proposed framework allows the insertion of a channel impulse response defined by the user. The channel estimation can be performed either using pilot subcarriers or Golay sequence as channel estimation sequences. Independently of the channel estimation technique selected, frequency domain equalization is available through ZF approach or MMSE. The simulation framework also allows channel coding techniques in order to provide a more robustness transmission and to improve the link budget.

Keywords: multigigabit, 60 GHz, OFDM, mmWave, simulation framework, multipath fading channels.

List of Figures

List of Tables

List of Abbreviations

mmWave	millimeter wave
5G	**5**th **G**eneration
ITU	**I**nternational **T**elecommunications **U**nion
MIMO	**M**ultiple-**I**nput **M**ultiple-**O**utput
MU-MIMO	**M**uliple-**U**ser MIMO
SDR	**S**oftware **D**efined **R**adio
OFDM	**O**rthogonal **F**requency **D**ivision **M**ultiplexing
PHY	**Phy**sical layer
LDPC	**L**ow-**D**ensity **P**arity-**c**heck codes
RS	**R**eed-**S**olomon codes
UM	**U**sage **M**odel
SC	**S**ingle-**C**arrier
MCS	**M**odulation and **C**oding **S**chemes
PAPR	**P**eak-to-**A**verage **P**ower **R**atio
QAM	**Q**uadrature **A**mplitude **M**odulation
PSK	**P**hase **S**hift **K**eying
QPSK	**Q**uadrature **P**hase **S**hift **K**eying
OOK	**O**n-**O**ff **K**eying
ISI	**I**nter-**s**ymbol **I**nterference
ICI	**I**nter-**c**arrier **I**nterference
FDM	**F**requency **D**ivision **M**ultiplexing
PL	**P**ath **L**oss
PDP	**P**ower **D**elay **P**rofile
RMS	**R**oot **M**ean **S**quare
SNR	**S**ignal-to-**N**oise **R**atio
BER	**B**it **E**rror **R**ate
FEC	**F**orward **E**rror **C**orrection codes
CFR	**C**hannel **F**requency **R**esponse
CIR	**C**hannel **I**mpulse **R**esponse
AWGN	**A**dditive **w**hite **G**aussian **N**oise

CP	**C**yclic **P**refix
MSE	**M**ean **S**quared **E**rror
PSNR	**P**eak **S**ignal-to-**N**oise **R**atio
WPAN	**W**ireless **P**ersonal **A**rea **N**etwork
LOS	**L**ine **o**f **S**ight
NLOS	**N**on **L**ine **o**f **S**ight
EIRP	**E**quivalent **I**sotropically **R**adiated **P**ower
MMSE	**M**inimum **M**ean **S**quare **E**rror
ZF	**Z**ero-**F**orcing
LS	**L**east-**S**quare
CES	**C**hannel **E**stimation **S**equence
GCS	**G**olay **C**omplementary **S**equences
TX	Transmitter
RX	Receiver

Contents

Chapter 1

Introduction

1.1 Motivation

The growth in the number of mobile subscribers and the need for higher transmission data rates systems has led to the interest of using the unlicensed millimeter wave (mmWave) spectrum (especially the 60 GHz band) [1]. Although radio communication systems at 60 GHz can enable multigigabit transmission rates, they are characterized by high free space losses. Thus, such wireless communication systems aim to cover less distance range in comparison with the ones operating at lower frequencies, making a mmWave system more appropriate for short range applications, i.e., indoor scenarios communications. The interest in 60 GHz band led to the establishment of several standards, e.g. IEEE 802.15.3c [2] and IEEE 802.11ad [3]. The IEEE 802.15.3c was the first standard addressing multigigabit short-range applications [1], targeting kiosk, residential, desktop and office as propagation environments.

Recently, mmWave spectrum has been appointed as a strong candidate to support 5G technologies for high data rate transmission in short-range applications [4, 5]. Several research projects addressing multigigabit data rates employing new waveforms, multicarrier modulation schemes, high-order modulations, Multiple-Input Multiple-Output (MIMO) techniques and adaptive channel estimation or equalisation, are being frequently published. It leads to the need of a simulation environment where these techniques can be tested and validated, in order to assess their viability for implementation on a future 5G wireless communication system.

To provide gigabit data rates it is mandatory the use of spectrally efficient techniques. OFDM is a well-known multicarrier communication technique adopted by most

of the newly wireless communication standards [1], due to its capability of converting a frequency selective channel into several flat-fading subchannels [6]. Accordingly, this OFDM feature allows the utilization of simple one-tap equalization methods, which consequently reduces the receiver complexity. However, OFDM is effective only when the receiver is capable to estimate the Channel Frequency Response (CFR). Despite the existence of a large number of published articles addressing channel estimation techniques at 60 GHz, to the authors' knowledge, none of them present a detailed performance comparison of those techniques using CES and pilot subcarriers for both coded an uncoded system transmission. For example, references [7, 8, 9, 10, 11, 12] focus their study only in Golay channel estimation sequences (CES) at 60 GHz without performing a comparison with other channel estimation techniques. Pilot allocation schemes in OFDM systems have been also studied in the last years in order to improve the channel estimation performance on behalf of a reduced overhead [13, 14, 15, 16, 17, 18, 19, 20, 21]. However none of the publications considers an pilot allocation scheme optimization base in the multipath channels proposed by TG3c group [22].

1.2 Aims and Objectives

This dissertation presents the implementation, validation and performance evaluation of a OFDM-based simulation framework for multigigabit applications at 60 GHz band. The simulation framework aims to be modular and scalable in order to meet easily with different requirements and techniques. Thus, it can be easily adapted to work with future standard requirements as 5G or other communication systems designed for mmWave transmission. Next, the main objectives of the dissertation are described.

- Identification of the stat-of-the-art in terms of multigigabit prototyping platforms and the requirements for further 5G mobile communication systems;
- Implementation of a simulation framework based on OFDM modulation for multigigabit applications at mmWave frequencies;
- Test and validation of the simulation framework;
- Study of the impact of wireless multipath fading channels in a mmWave-based system;
- Study of the impact of cyclic prefix extension in the system's performance;

- Assessment of the impact of channel estimation techniques and forward error correction codes in the performance of the communication system.

1.3 Structure of the document

This document contains six chapters and they are organized as follows. The current chapter introduces the work by presenting its context, motivation and objectives. It is also presented the main contributions that have resulted from the work described further.

The second chapter review the state-of-the-art related to the implementation of multigigabit prototype systems addressing different MIMO techniques, in order to contribute for a future 5G wireless communication system. After being presented, the different prototyping systems are compared in terms of spectral efficiency. This chapter also presents the main standards available for 60 GHz band and their PHY layer design modes.

Chapter 3 aims to provide all the theoretical fundamentals needed for the implementation of the multigigabit framework.

In chapter 4 the implementation of each block of the framework is presented and detailed. The validation of the framework is shown in the end of the chapter, where the simulation results are compared with the theoretical ones.

Chapter 5 presents the performance results of the simulation framework based on the IEEE 802.15.3c standard specifications. The simulation results are discussed in the end of the chapter and several consideration are duly justified.

Finally, chapter 6 concludes this dissertation and presents some suggestions for future work.

1.4 Main contributions

The work presented in this dissertation contributed for the publication of the following paper.

R. Gomes, R. Caldeirinha, A. H. Hammoudeh and P. Pires, Performance Evaluation of 60 GHz OFDM Communications under Channel Impairments over Multipath Fading Channels at 60 GHz, *Sensors & Transducers*, vol. 204, pp. 29-38, Sept. 2016.

Chapter 2

Review of the state-of-the-art

2.1 Introduction

The constant growth of internet, wireless communication technologies and the user requirements lead to new consumer oriented high data rate applications [23]. The telecommunication industry is converging on a common set of 5G requirements which includes network speed as high as 10 Gbps, cell edge rate greater than 100 Mbps and latency of less than 1 ms [24]. The implementation of such wireless communication systems requires the availability of large bandwidths.

Recently, the International Telecommunication Union (ITU) has defined the key requirements related to the minimum technical performance of IMT-2020 (commonly related to 5G) candidate radio interface technologies [24]. The ITU report defines a minimum peak data rate for a single mobile station of 20 Gbps for downlink and 10 Gbps for uplink applications. The required peak spectral efficiency for downlink is 30 bit/s/Hz and for uplink it is expected a maximum of 10 bit/s/Hz. These values were defined assuming 8×4 MIMO. According to ITU, a latency of 1 ms must be achieved and communications at up to 500 km/h should be guaranteed. To this extent, the development of technology capable of providing such applications, is timely and topical. In this context, many advanced communication techniques are under investigation. However, the proposed new communication techniques are often studied and analysed at the algorithmic level considering mainly the quality of the communication link, i.e. quality of service. Although this remains as one of the main Key Performance Indicators (KPI), the related hardware and energy efficiencies are becoming increasing crucial requirements for future mobile terminals and networks [25]. Thus, the availability of new rapid design, validation flows and related prototyping experiences are of

high interest for performance validation and proof of concept of the diverse proposed communication.

2.2 5G prototyping systems

The future 5G at mmWave will require MIMO operation to support multiple independent data streams and enhance spectral efficiency [26]. New hybrid MIMO architectures are being studied in [27] as an alternative for fully digital precoding, aiming at the possible reduction in the number of RF chains and ADCs/DACs [28]. Many prototyping testbed approaching massive MIMO technologies have been published in the last years. Argos V2 testbed [29, 30] developed, at Rice University (USA) a massive MIMO 96-antenna base station, based on WARP platform [31], which supports real-time streaming applications to 32 users simultaneously. Argos base station is shown in Figure 2.1.

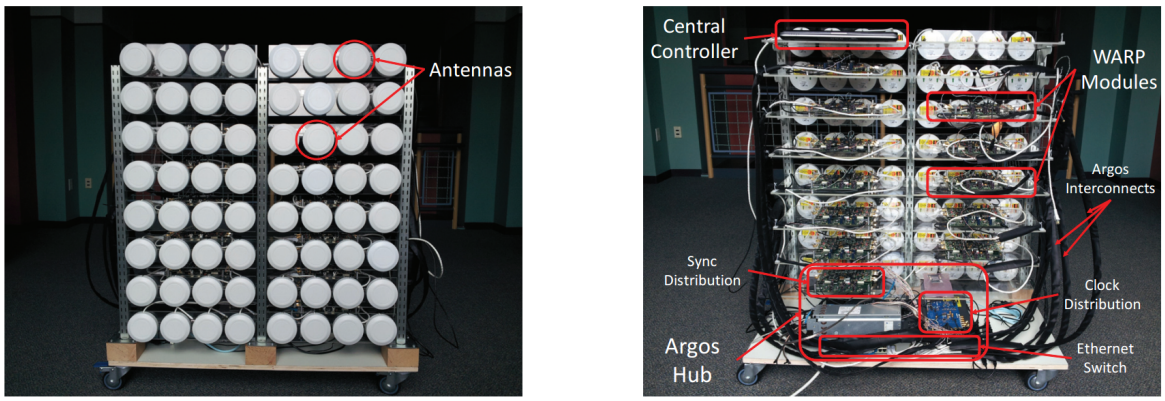

Figure 2.1: Argos massive MIMO testbed [29].

Lund university (Sweden) implemented a 100-antenna testbed for massive MIMO [32] (Figure 2.2) based on National Instruments software-define radios (SDRs) 2953Rs and USRP-RIOs operating at 3.7 GHz with 20 MHz of bandwidth.

In [33], the Ngara Rural Wireless Broadband Access Demonstrator is presented. It employs MU-MIMO OFDM transmission in rural areas where a spectral efficiency of 67.26 bit/s/Hz is achieved in lab environment at 638 MHz band. ZTE implemented a TDD massive MIMO prototype [34] where 64 transceivers served 6 LTE-based handsets, achieving a 300 Mbps sum rate in 20 MHz bandwidth. According to [35], Samsung has been working in a milimiter wave testbed where a throughput of 1Gbps is achieved at up to 2 km range using 28 GHz band. [35] also refers that NTT DoCoMo announced a data rate of 10 Gbps using 400 MHz bandwidth at 11 GHZ band. Finally, University of

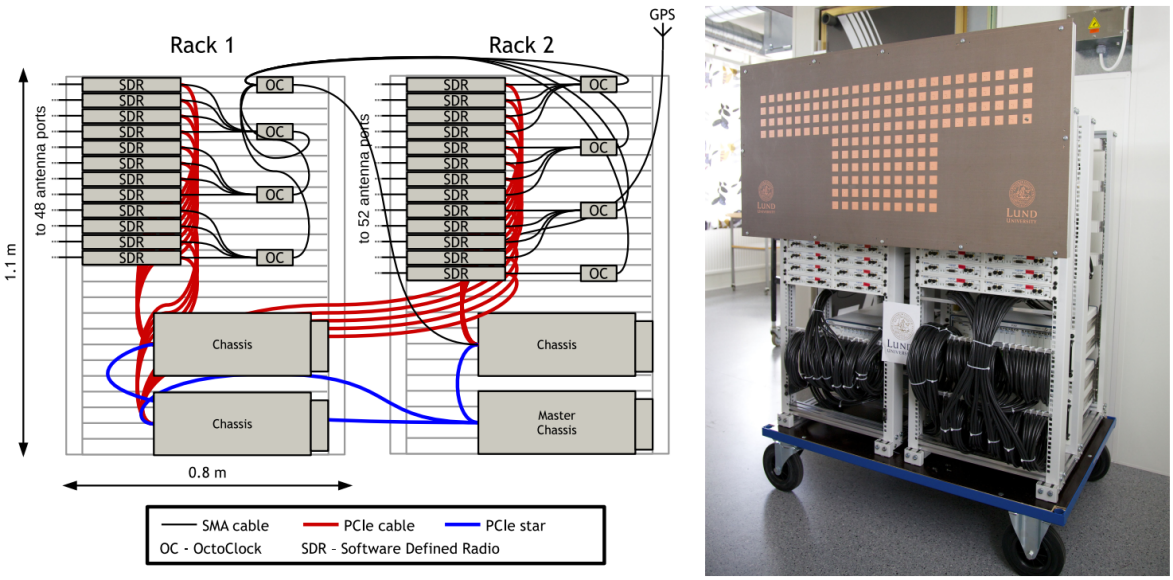

Figure 2.2: Lund University 100-antenna testbed [32].

Bristol (UK) in collaboration with Lund University and National Instruments presented a 128-antenna massive MIMO testbed [36, 37] that can be seen in Figure 2.3.

Figure 2.3: University of Bristol: massive MIMO testbed [37].

The testbed operates in real-time with a LTE-like PHY and supports up to 22 users at 3.51 GHz and considering 256 QAM constellations. It corresponds to the highest spectral efficiency achieved, 145.6 bit/s/Hz. Table 2.1 summarizes the main characteristics of the present testbeds.

From Table 2.1 can be seen that all testbeds are characterized for an available bandwidth of a few tens of MHz. This fact is due to the lack of available spectrum in the bands where the testbeds work, which would not be a problem if the prototype

Table 2.1: Main characteristics of prototype massive MIMO testbeds towards 5G communications.

Project /Institution	Frequency (GHz)	# of BS antennas	# of users	Bandwidth (MHz)	Efficiency (bit/s/Hz)
Argos V2 [29, 30]	N/A	96	32	N/A	N/A
Lund University [32]	3.7	100	10	20	N/A
Ngara [33]	0.638	32	12	28	67.26
ZTE [34]	2.6	128	6	20	15
Samsung [35]	28	N/A	N/A	N/A	N/A
NTT DoCoMo [35]	11	N/A	N/A	400	25
Bristol University [36]	3.51	128	22	20	145.6

testbeds were implemented in 60 GHz band.

2.3 Overview of 60 GHz standards

The interest in 60 GHz radio communications resulted in the formation of several international mm-wave standard groups and industry alliances [1]. In this work is presented two of the most popular standards in 60 GHz band: IEEE 802.11.ad (WiGig) and IEEE 802.15.3c. In this section the IEEE 802.15.3c is presented in more detail when compared to IEEE 802.11.ad, since it was the first standard addressing multigigabit short-range applications and for that reason is the reference standard for the following study.

2.3.1 IEEE 802.11ad

Within the IEEE 802.11 working group, Task Group 'ad' (TGad) was tasked with defining modifications to the 802.11 MAC and PHY in order to enable operation in the 60 GHz frequency band capable of a maximum throughput of at least 1 Gbps [38]. In 2009 a proposal based on Wireless Gigabit Aliance (WGA) MAC and PHY was contributed to TGAd as a complete proposal specification. Thus, IEEE 802.11ad specification extends the MAC and PHY definitions as necessary to support short range (1 m to 10 m) at up to 6.75 Gbps in th 60 GHz band. It also supports 2.4 GHz and 5 GHz bands. In this context, Table 2.2 shows typical configuration for several device classes and the expected range and throughput for those classes.

Table 2.2: Typical device configurations for IEEE 802.11ad [3].

Device	**Expected range (m)**	**Expected throughput (Gbps)**	**Traffic type**
AP, Docking station	20	7	Bursty on downlink
Wireless peripherals	0.5 to 2	4.6	Bursty
Wireless display, TV	5 to 10	7	Continuous
Notebook	5 to 10	4.6 to 7	Symetric TX and RX
Tablets	2 to 5	4.6	Symetric TX and RX
Smartphone, camera	0.5 to 2	1.2 to 4.6	Symetric TX and RX

IEEE 802.11ad defines three different PHY layers dedicated to different application scenarios [3]. The Control PHY is designed for low SNR operation prior to beamforming. Single Carrier (SC) PHY enables power efficient and low complexity transceiver implementation. The low-power SC PHY replaces the LDPC encoder by a Reed Solomon encoder for further processing power reduction. The OFDM PHY layer provides high performance in frequency selective environments. Despite having different PHYs, all of them share the same packet structure with common preamble properties. Also a common rate 3/4 LDPC is used for channel coding purposes.

The standard defines a single bandwidth of 2.16 GHz, which is 50 times wider than the channels defined in IEEE 802.11ac. A single IEEE 802.11ad packet structure [3] is shown in Figure 2.4 which consists in a short training field (STF) and a channel estimation field (CEF) that is also used for auto-detection of the PHY type. The packet is also composed by The PHY header, PHY payload (protected by cyclic redundancy check (CRC)), automatic gain control (AGC) and training (TRN) fields.

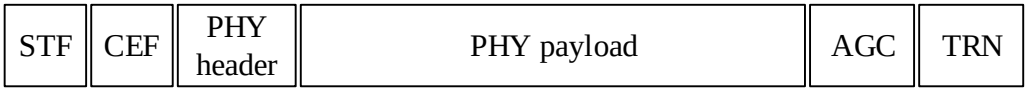

Figure 2.4: IEEE 802.11ad packet structure.

2.3.2 IEEE 802.15.3c

The IEEE 802.15.3c Task Group (TG3c) was formed in 2005 to develop a mm-wave based alternative for the existing IEEE 802.15.3-2003 WPAN standard. IEEE 802.15.3c standard is aimed at supporting a minimum data rate of 2 Gbps for short-range applications and it is the first standard that addresses multi-gigabit wireless systems

[1]. The 802.15.3c Task Group presents five usage models (UMs) related to the possible consumer applications in the 60 GHz band [39]: **UM 1) Uncompressed video streaming:** The bandwidth available in the 60 GHz band enables sending HDTV signals without the needing for video cables. It is expected a data rate over 3.5 Gbps in a 10 m range with a pixel error rate below 10^{-9}. **UM 2) Uncompressed multivideo streaming:** The 802.15.3c system should be able to provide video signals for at least two 0.62 Gbps streams. **UM 3) Office desktop:** This UM enables the communication between a personal computer and other external peripherals, including printers and hard drives. **UM 4) Conference and hadoc:** This UM considers a scenario where several computers are communicating between each other using one 802.15.3c network. **UM 5) kiosk file downloading:** TG3c group assumed electronic kiosks that enables, for example downloading video and music files at 1.5 Gbps at 1 m range.

The IEEE 802.15.3c channel modelling subcommittee has defined a new channel model in regard of the Saleh-Valenzuela (S-V) model previously used in IEEE 802.11. The new model combines a line-of-sight (LOS) component using a two-path model with de NLOS reflective clusters of the S-V model [40].

The target applications of the standard have different requirements and for that reason 802.15.3c Task Group has developed three different PHY modes: Single Carrier mode (SC PHY), High-Speed Interface mode (HSI PHY) and Audio-Visual mode (AV PHY). The SC PHY is most suitable for office desktop (UM3) and kiosk file downloading (UM5) usage models. The HSI PHY mode is designed for bidirectional, NLOS, low-latency communication scenarios, which is the case of the conference and hadoc usage model (UM4). The AV PHY is designed to provide high throughput video streams (usage models 1 and 2). A comparison of this three PHY modes is given in Table 2.3 [41].

Table 2.3: Comparison of the PHY modes provided by the standard.

Modes	**SC PHY**	**AV PHY**	**HSI PHY**
Main usage model	UM3 and UM5	UM1 and UM2	UM3 and UM4
Data rate	0.3 Mbps - 5.28 Gbps	0.95 - 3.8 Gbps	1.54 - 5.78 Gbps
Constellation	BPSK, QPSK, 8-PSK, 16-QAM	QPSK, 16-QAM	QPSK, 16-QAM, 64-QAM
Transmission scheme	SC	OFDM	OFDM
Forward error control	RS/LDPC	RS	LDPC
Block size	512	512	512

The main difference between this physical layer modes is the modulation scheme.

While SC PHY uses single carrier (SC) modulation, AV PHY and HSI PHY uses OFDM. SC modulation allows lower complexity and low power operation, whereas OFDM is more appropriated in high spectral efficiency and NLOS channel conditions. Further the three PHY layers are explained in detail according to [41] and [2].

2.3.2.1 Single Carrier PHY

SC PHY provides three classes of modulation and coding schemes (MCSs) focusing on different wireless connectivity applications. Class 1 addresses kiosk file downloading and low-power mobile market with data rates of up to 1.5 Gbps. Class 2 aims to achieve data rates up to 3 Gbps and is defined for office desktop. Class 3 is specified for supporting high-performance applications with data rates exceeding 3 Gbps. The MCs dependent parameters for SC PHY is shown in Appendix A. In SC PHY the support of $\pi/2$-shifted binary phase shift keying ($\pi/2$ BPSC) is mandatory for all devices since it improves the peak-to-average power ratio. Other supported modulation schemes are $\pi/2$ QPSK, $\pi/2$ 8-PSK, $\pi/2$ 16 QAM, OOK and DAMI. In IEEE 802.15.3c, data is divided into blocks, each block is divided in subblocks and each subblock consists of pilot word and data, as presented in Figure 2.5.

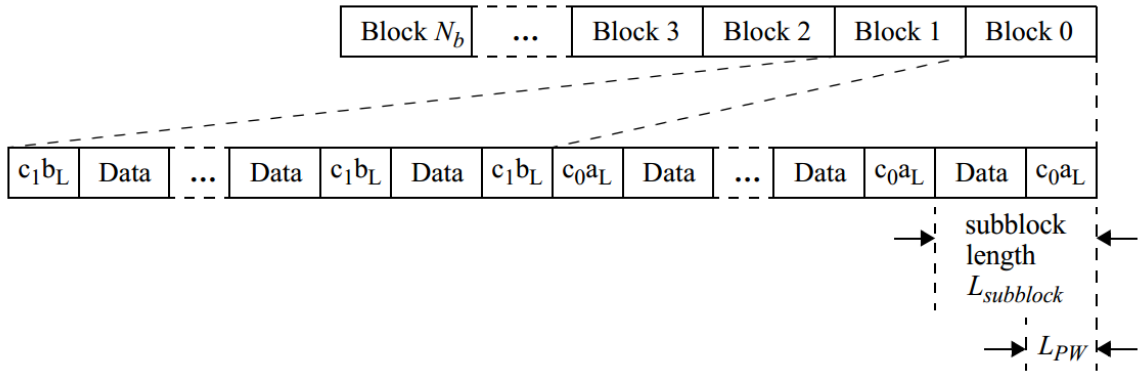

Figure 2.5: Block structure for IEEE 802.15.3c PHY layers [2].

A block contain 64 subblocks with the exception of the last block i.e., the $N_b{}^{th}$ block. A subblock is formed by appending a pilot word to the data. The possible pilot word lengths are 0, 8 and 64. Frame-related parameters and time-related parameters for SC PHY can be found in Appendix A.

The standard defines two main FEC schemes: Reed Solomon block codes and LDPC block codes. RS codes are selected for their low complexity in high-speed communications. RS(255,239) is the main FEC and is used for payload protection. The RS code

use the generator polynomial given by

$$g(x) = \prod_{k=1}^{16}(x + \alpha^k) \tag{2.1}$$

, where α=0x02 is a root of the binary primitive polynomial $p(x) = 1+x^2+x^3+x^4+x^8$.

The mapping of the information octets m to codeword octets c is achieved by computing polynomial $r(x)$:

$$r(x) = \sum_{k=0}^{15} r_k x^k \;\; = \;\; x^{16} m(x) mod(g(x)) \tag{2.2}$$

, where $m(x)$ is the information polynomial given by

$$m(x) = \sum_{k=0}^{238} m_k x^k \tag{2.3}$$

The message order is as follows: m_{238} is the first octet of the message and m_0 is the last one. In Figure 2.6 the structure of the Reed Solomon encoder adopted by the IEEE 802.15.3c standard is depicted.

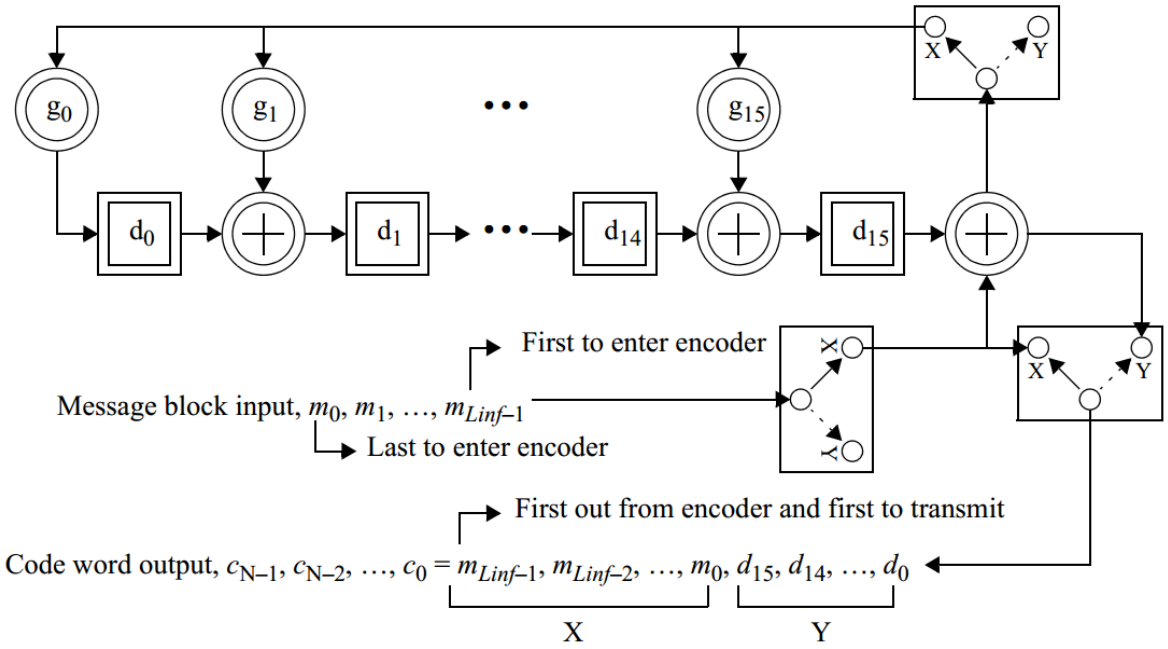

Figure 2.6: Reed Solomon encoder [2].

Four LDPC coding schemes with different coding rates are specified to provide higher coding gain with reasonable implementation complexity, they are LDPC(672,336),

LDPC(672,504), LDPC(672,588) and LDPC (1440,1344). The LDPC encoder is systematic, i.e., it encodes an information block of size k, $i = (i_0, i_1, ..., i_{k-1})$ into a codeword c of size n, where $c = (i_0, i_1, ..., i_{k-1}, p_0, p_1, ..., p_{k-1})$, by adding $n - k$ parity bits obtained so that $Hc^T = 0$, where H is an $(n - k) \times n$ parity check matrix.

Each parity check matrices can be partitioned into submatrices of size $z \times z$ ($z = 21$). These submatrices are either cyclic permutation of the identity matrix or null submatrices. The cyclic-permutation matrix p^i is obtained from the $z \times z$ identity matrix by cyclically shifting the columns to the left by i elements. The matrix p^0 is the $z \times z$ identity matrix. An example of cyclic-permutation matrices with $z = 21$ is shown in (2.4). The matrix p^1 and p^2 are produced by cyclically shifting the columns of the identity matrix $I_{21\times21}$ to the left by 1 and 2 places, respectively. Note that due to the cyclic permutation, $p^{21} = p^0 = I_{21\times21}$.

$$p^0 = \begin{bmatrix} 1 & 0 & \dots & \dots & 0 \\ 0 & 1 & 0 & \dots & 0 \\ \dots & 0 & \dots & 0 & \dots \\ 0 & \dots & 0 & 1 & 0 \\ 0 & \dots & \dots & 0 & 1 \end{bmatrix}, p^1 = \begin{bmatrix} 0 & \dots & \dots & 0 & 1 \\ 1 & 0 & \dots & \dots & 0 \\ 0 & 1 & 0 & \dots & 0 \\ \dots & 0 & 1 & 0 & 0 \\ 0 & \dots & 0 & 1 & 0 \end{bmatrix},$$
$$p^2 = \begin{bmatrix} 0 & \dots & 0 & 1 & 0 \\ 0 & \dots & \dots & 0 & 1 \\ 1 & 0 & \dots & \dots & 0 \\ 0 & 1 & 0 & \dots & 0 \\ 0 & 0 & 1 & 0 & 0 \end{bmatrix} \tag{2.4}$$

Figure A.4, Figure A.5 and Figure A.6 from Appendix A, displays the matrix permutation indices of parity check matrices for all three FEC rates with clock length = 672 bits, LDPC(504,672), LDPC(336,672) and LDPC(588,672), respectively. The $'-'$ entries in the table denote null submatrices.

In the receiver for the LOS environment, conventional matched filtering is sufficient for achieving acceptable performance, but for NLOS environment, frequency domain equalization may be included to mitigate multipath fading.

2.3.2.2 Audio/Visual PHY

Within AV PHY two different sub-PHY modes are considered: high-rate PHY (HRP) for video transmission and low-rate PHY (LRP) for the control signal. Both sub-PHY use OFDM. The HRP mode has an FFT length of 512 and uses all the channel bandwidth available, delivering data rates of 0.952, 1.904 and 3.807 Gbps as can be seen in Appendix B.1. On the other hand, the LRP mode occupies only 98 MHz bandwidth and three LRPs are arranged per HRP channel. This allocation aims to accommodate three different networks in one channel.

The AV PHY uses RS codes as the outer code and convolutional coding as the inner code in HRP mode. Only convolutional coding is used in LRP mode. The convolutional encoder considered in this PHY layer use length $K = 7$, delay memory 6, generator polyonmial $g0 = 133o, g1 = 171o, g2 = 165o$ and code rate 1/3.

Modulation schemes used are limited to QPSK and 16 QAM and the corresponding modulation parameter are presented in Appendix B.2.

2.3.2.3 High-Speed Interface PHY

As stated before, the HSI PHY is designed mainly for computer peripherals that require low-latency bidirectional data, focusing on the conference hadoc UM, and uses OFDM, where the FFT size is 512.

As OFDM modulation has an inherent complexity due to the IFFT and FFT operations, only the LDPC coding scheme is used in the HSI PHY. Four FEC rates are obtained using LDPC(336,672), LDPC(504,672), LDPC(588,672) and LDPC(420,672) codes which allows code rates of 1/2, 5/8, 7/8 and 3/4, receptively. The LDPC encoding process for HSI PHY is the same as explained in Section 2.3.2.1 where the first three matrix permutation of the block codes for HSI were introduced. The matrix permutation indices of the parity check matrix for LDPC(420,672) is depicted in Appendix C.4.

In terms of modulation, three modulation schemes are selected: QPSK, 16 QAM and 64 QAM, which allow data rates up to 5.775 Gbps, as can be seen in detail in Appendix C.1. The standard suggests that the conversion from binary data to complex symbols shall be performed according to Gray-coded constellation mapping as shown

in Figure C.5. After the modulation, a normalization factor K_{MOD} are applied to the complex values and it is dependent of the selected modulation scheme (Table 2.4), where d can be either 1 or 1.25 if normal or skewed constellation is considered.

Table 2.4: Normalization factor of digital modulation [2].

Modulation	K_{MOD}
QPSK	$1/\sqrt{1+d^2}$
16 QAM	$1/\sqrt{5(1+d^2)}$
64 QAM	$1/\sqrt{21(1+d^2)}$

Both timing-related parameters and frame-related parameters of the HSI PHY layer can be found in Appendix C.2 and Appendix C.3, respectively. A summary of those parameters are shown in Table 2.5.

Table 2.5: Summary of the main parameters of HSI PHY.

Parameter	**Value**
FFT size block (N_{FFT})	512
Cyclic prefix (N_{CP})	64 samples
Sampling rate	2640 MHz
Sub-carrier bandwidth	5.15 MHz
Cyclic prefix time	24.24 ns
Symbol time	218.18 ns
Modulation	16 and 64 QAM
Nominal used bandwidth	1.815 GHz

The IEEE 802.15.3c standard suggests the implementation of a comb type pilot arrangement. It means that in the case of HSI PHY in all OFDM symbols, sixteen of the subcarriers shall be dedicated to pilot signals and shall be placed in the logical indexes according to the information in Table 2.6. The standard suggests that the information for the m^{th} pilot subcarrier of each OFDM symbol is defined as follows in Eq.2.5 [2].

$$x_p(m) = \begin{cases} (1+j)/\sqrt{2}, & m = 0,3,5,7,9,13,15 \\ (1-j)/\sqrt{2}, & m = 1,2,4,6,8,10,11,12,14 \end{cases} \tag{2.5}$$

In addition to the pilot allocation, the standard have defined also which subcarriers are assigned to guard purposes, null subcarriers and DC subcarriers, as can be seen in Table 2.6. The resulting subcarrier frequency allocation is illustrated in Figure 2.7.

Table 2.6: IEEE 802.15.3c subcarrier allocation in frequency spectrum domain.

Subcarriers type	Number of subcarriers	Logical indexes
Null	141	[-256: -186] ∪ [186: 255]
DC	3	-1, 0, 1
Pilot	16	[-166:22:-12] ∪ [12:22:166]
Guard	16	[-185: -178] ∪ [178: 185]
Data	336	All others

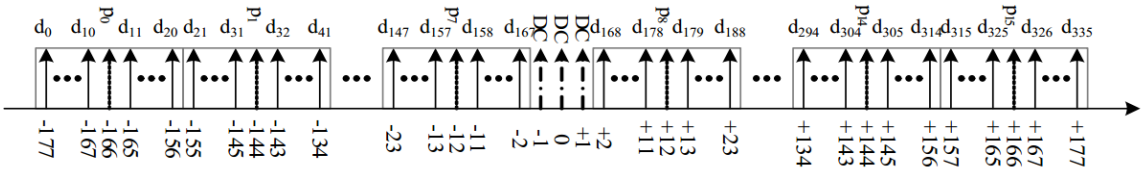

Figure 2.7: Subcarrier frequency allocation according to IEEE 802.15.3c standard [2].

Considering a 512-point IFFT, the subcarriers 2 to 185 are mapped to the same numbered IFFT inputs, while the logical subcarriers -185 to -2 are copied into IFFT inputs 327 to 510. The inputs assigned to null subcarriers are set to zero. The same happens to subcarriers 0,1 and 511 to avoid difficulties in digital to analog (D/A) and analog to digital (A/D) converter offsets and carrier feed through the RF system. This mapping is illustrated in Figure 2.8.

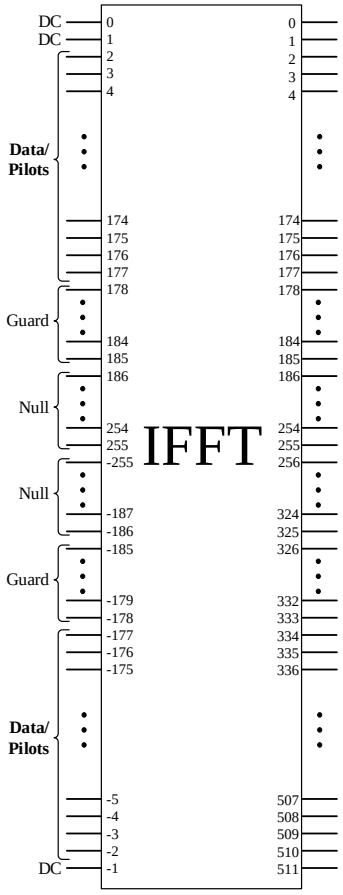

Figure 2.8: Subcarriers allocation in IFFT block, based on IEEE 802.15.3c standard.

2.4 Summary

This chapter presented the main requirements of 5G communication systems, established by the telecommunications institutes at the time of writing the document. In Section 2.2, a review of the different mulitgigabit platforms available in the literature focused on 5G technology is presented. Despite the relatively good spectral efficiency results, non of the prototyping tesbeds operates at 60 GHz spectrum, which could be very profitable due to the available bandwidth in this bands. Section 2.3 presents two of the most known standards at 60 GHz: IEEE 802.11.ad (WiGig) and IEEE 802.15.3c.

Chapter 3

Theoretical Fundamentals

3.1 Introduction to OFDM

Orthogonal Frequency Division Multiplexing (OFDM) is a modulation scheme that is widely used for high data rate transmission in delay dispersive environments, since it split a frequency-selective channel bandwidth into several flat sub-bands [42]. High data rate transmission schemes usually employs single-carrier or multicarrier systems. Since in this work, a multicarrier approach is explored (OFDM), a comparison between those approaches is described next.

3.1.1 Single-carrier vs. multicarrier systems

In a single-carrier system, the transmitted symbol a_n are pulse-shaped by a transmit filter $g_T(t)$ in the transmitter. The period of each symbol is T seconds, which is translated in a data rate of $R = 1/T$. Consider a band-limited channel $h(t)$ with an available bandwidth W. After receiving the symbols through the channel they are processed in the received filter, as shown in Figure 3.1. Let $g_T(t)$, $g_R(t)$, and $h^{-1}(t)$ denote the impulse response of the transmit filter, receive filter and equalizer, respectively.

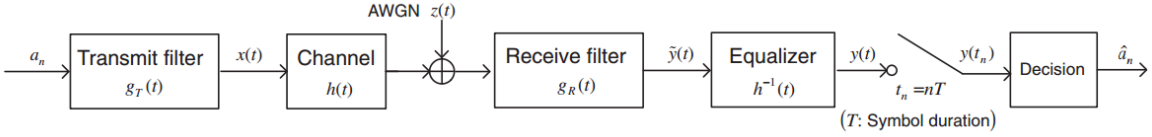

Figure 3.1: Single-carrier baseband communication system [43].

According to [43], the output of the equalizer is expressed as

$$y(t) = \sum_{m=-\infty}^{\infty} a_m g(t - mT) + z(t) \tag{3.1}$$

,where $z(t)$ denotes an additive noise and $g(t)$ the impulse response of a single-carrier system that is given as

$$g(t) = g_T(t) * h(t) * g_R(t) * h^{-1}(t) \tag{3.2}$$

According to Nyquist criterion and in order to support a symbol rate of R_s symbols per second, the minimum required bandwidth is given by $R_s/2$ Hz. It implies that a wide bandwidth is required to support high data-rate over single-carrier transmission mode. Thus, as the symbol rate increases, the signal bandwidth becomes even larger, which leads inter-symbol interference (ISI). Equalizers employed to deal with the ISI incurred by time-varying multipath fading channel are known for high complexity. Due to its complexity, these equalizers are not efficient for implementation in certain devices.

To overcome the frequency selectivity, if the wideband channel experienced by single-carrier transmission, multiple carriers can be used for high rate data transmission. Figure 3.2 shows the concept of a multicarrier transmission system. It can be seen that the wideband signal is divided through multiple narrow band filters into several narrowband signals at the transmitter. In the receiver, the frequency-selective wideband channel can be approximated by multiple frequency-flat narrowband channels, which allows to reduce the complexity of the equalizer, since equalization is performed for each subchannel. As long as the orthogonality among subchannel is maintained, the inter-carrier interference (ICI) can be suppressed [43].

3.1.2 Orthogonal Frequency Division Multiplexing

OFDM can be seen as an evolution of Frequency Division Multiplexing (FDM). OFDM transforms an high-data rate data stream into N low-data rate parallel streams allocated in different orthogonal subcarriers, which enables the possibility to avoid guard bands between subchannels,when compared with FDM, resulting in a significant improvement of spectral efficiency. Figure 3.3 shows the frequency spectrum comparison between FDM and OFDM modulation schemes. It can be seen that an OFDM system

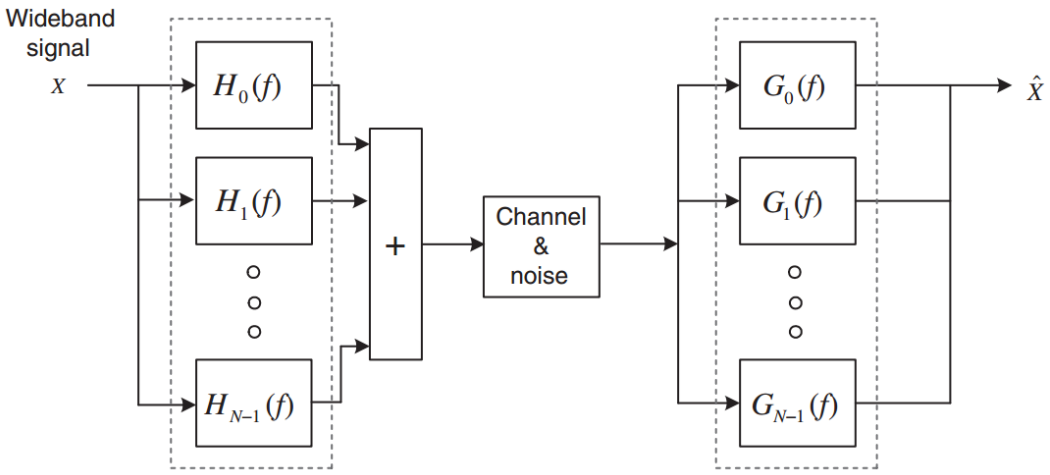

Figure 3.2: Multicarrier baseband communication system [43].

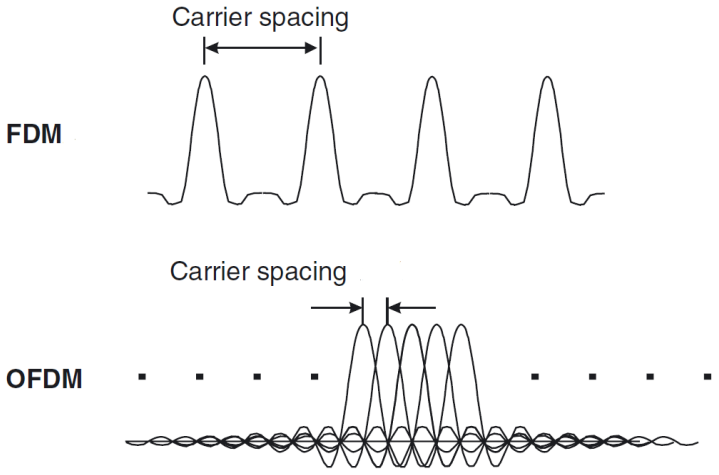

Figure 3.3: Comparison between FDM and OFDM in terms of spectral efficiency. [42]

requires less bandwidth than an FDM system to transmit the same data stream, due to its subcarrier orthogonality. Therefore, with the OFDM modulation scheme it is possible to reduce the space between subcarriers and even reduce ICI.

In a conventional SC transmission, to achieve gigabit data rates, the symbol is in order of nano-secons (ns), which means that the complexity of the channel equalization is, in some cases very high. Since in OFDM systems the transmitting symbol time is much higher than in single carrier, the channel equalization complexity can be significantly decreased.

3.1.2.1 M-ary Digital Modulation

Digital modulation is the mapping of data bits into signal waveforms that can be transmitted over a channel [42]. At the transmitter (TX) the digital modulator has to convert the digital source data into analog waveforms, while at the receiver (RX), the demodulator recovers the bits from the received waveform.

An analog waveform can represent either one bit or a group of bits, depending of the modulation typology. Generally, a group of K bits can be encoded in to a symbol, which is mapped into one out of a set of $M = 2^K$ waveforms. Typically, the waveform corresponding to one symbol is time limited to a time T_S. Therefore, the bit rate is K times the transmission symbol rate.

A typical example of two digital modulation methods are QPSK and QAM. QPSK is a characterized for four ($M = 4$) different waveforms, which result in two ($K = 2$) bits per symbol. Thus the modulated signal is function of the carrier phase and is given by Eq.3.3.

$$s_i(t) = \sqrt{\frac{2E_s}{T_s}} cos(2\pi f_c + (2n-1)\frac{\pi}{4}), n = 1, 2, 3, 4 \tag{3.3}$$

,where $\sqrt{E_s}$ is the energy per symbol and f_c is the carrier frequency.

This yield the four phases $\frac{\pi}{4}$, $\frac{3\pi}{4}$, $\frac{5\pi}{4}$ and $\frac{7\pi}{4}$ and can be represented in a two-dimensional signal space as in Eq.3.4 and Eq.3.5.

$$\phi_1(t) = \sqrt{\frac{2}{T_s}} cos(2\pi f_c t) \tag{3.4}$$

$$\phi_1(t) = \sqrt{\frac{2}{T_s}} sin(2\pi f_c t) \tag{3.5}$$

Eq. 3.4 is used as in-phase component of the modulated signal and Eq.3.5 as in-quadrature component of the signal. Hence, the constellation consists in a 4 signal-space 4 points as shown in Figure 3.4.

QPSK modulation can be seen as a special case of QAM modulation since QPSK is

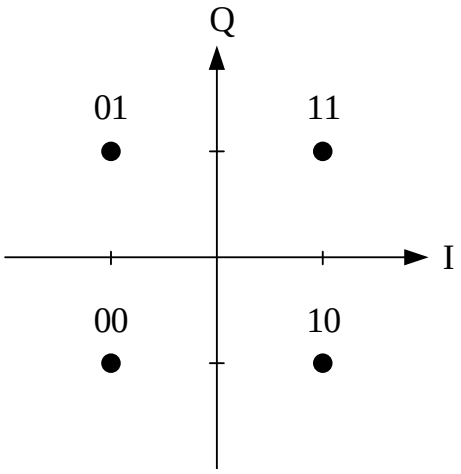

Figure 3.4: QPSK constellation.

not more than a 4 QAM modulation scheme. Thus, 16 QAM follows the same principle than QPSK, except for the fact that in 16 QAM the phase and amplitude is not kept constant. In Figure 3.5 can be seen that the distance of the 16 QAM symbols to the center of the constellation is not constant as happen in QPSK.

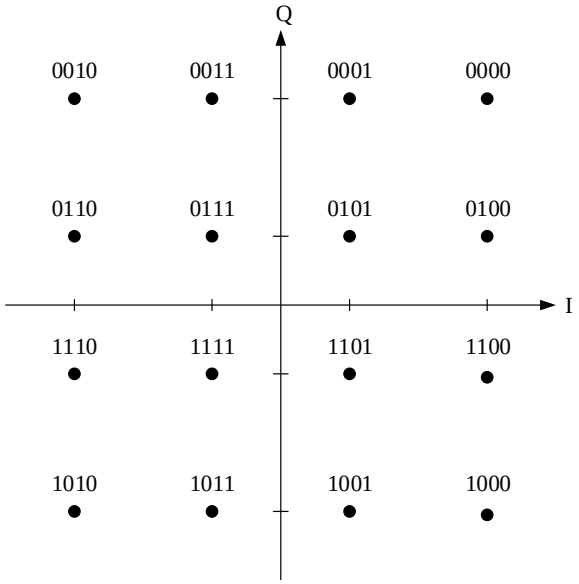

Figure 3.5: 16 QAM constellation.

Larger constellations, including 64 QAM or 256 QAM can be constructed according to similar principles.

3.1.2.2 The OFDM Principle

With a OFDM system it is possible to transmit N parallel data symbols, where each one can be assigned to a subcarrier using a modulation technique, such as QPSK or 16

QAM. The data rate per subcarrier is as slower as the number of subcarriers available in the system, increasing the transmission symbol time in each subcarrier. This fact leads to a lower complexity in the receiver since the consequences of a frequency selective channel are mitigated.

Let $X_n, n = 0, 1, ..., N-1$, be the N data symbols to be transmitted over N subcarriers, where X_n is represented as a complex point in a QAM modulation, for example and f_n be the frequency for the n^{th} subcarrier. The transmitted waveform in time-domain can be written as [1]

$$x(t) = \sum_{n=0}^{N-1} X_n e^{j2\pi f_n t} \tag{3.6}$$

and the corresponding digitally sampled version is given by

$$x(mT_s) = \sum_{n=0}^{N-1} X_n e^{j2\pi f_n m T_s} \tag{3.7}$$

, where $t = mT_s$ represents the sampling points and T_s the sampling period. Considering that the N subcarriers are equally spaced in frequency domain that $f_n = nf_o$, Eq. 3.8 becomes

$$x(mT_s) = \sum_{n=0}^{N-1} X_n e^{j2\pi n f_o m T_s} \tag{3.8}$$

, where $f_o = 1/NT_s$ is the minimum frequency separation to ensure subcarrier orthogonality. Thus, the time-domain samples can be written as

$$x(mT_s) = \sum_{n=0}^{N-1} X_n e^{j2\pi mn/N} \tag{3.9}$$

Analyzing Eq. 3.9 it is seen that is the Inverse discrete Fourier Transform (IFFT) of the N data symbols $(X_0, X_1, ..., X_{N-1})$. Thus, inverse FFT can be used at the OFDM transmitter whereas to recover the N data symbols from the time-domain samples received, FFT operation is performed. Figure 3.6 represents the concept of a OFDM transceiver.

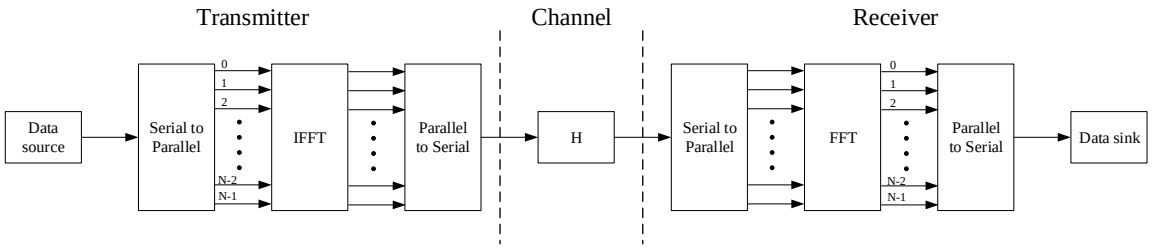

Figure 3.6: Transceiver structure of an OFDM system

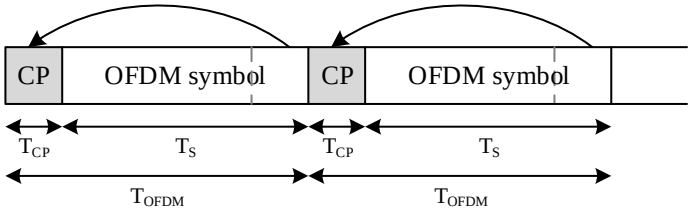

Figure 3.7: Principle of the cyclic prefix.

3.1.2.3 Cyclic Prefix

As already discussed, an OFDM system aims to reduce the negative effects of an high data rate transmission over frequency selective channels, by increasing the symbol time in each subcarrier. However, the effect of delayed OFDM symbols can lead to the loss of orthogonality among subcarriers, increasing ISI and consequently increasing Bit Error Rate (BER).

To overcome this issue, a cyclic prefix (CP) is used. The last N_{CP} samples of the symbol will be cyclically copied in front of the original OFDM signal, causing the OFDM symbol duration (T_{OFDM}) be the sum of the original symbol time (T_S) with cyclic prefix duration (T_{CP}), as shown in Figure 3.7. In the receiver side, the length of the cyclic prefix must be known in order to be properly removed. Figure 3.8 shows the block diagram of a OFDM transceiver with the cyclic prefix blocks.

The drawback of the CP insertion represents overhead for the OFDM system, which

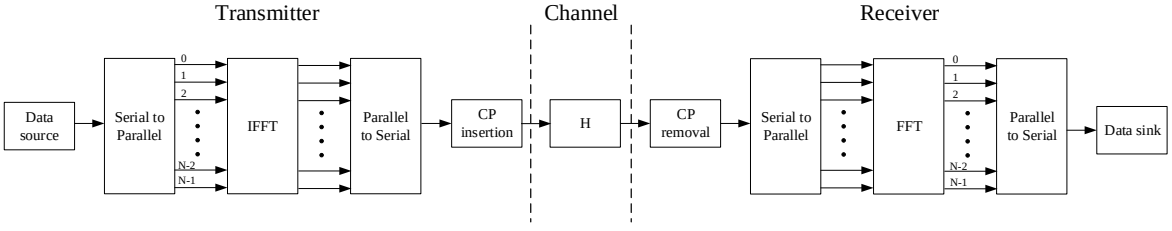

Figure 3.8: Transceiver structure of an OFDM system considering CP insertion.

results in loss of energy (Eq. 3.10) efficiency and system throughput that must be considered [44]. This loss of energy efficient is due to fact that redundant information is being transmitted, increasing the overhead of the system.

$$L_{CP} = 10log_{10}(\frac{T_{OFDM}}{T_S}) \quad [dB] \tag{3.10}$$

3.2 Mobile wireless multipath fading channels

The performance of mobile wireless communication systems is strongly dependent by the wireless channel environment. As opposed to the typically static and predictable characteristics of a wired channel, the wireless channel is dynamic and unpredictable, which makes an exact analysis of the wireless system often difficult [43].

In wireless communications, radio waves are mainly affected by three different modes of physical phenomena: reflection, diffraction and scattering [45], [46]. Reflection occurs when propagating wave impinges upon an object with large dimensions compared to the wavelength, for example, surface of earth or a building. Diffraction occurs when the radio path between transmitter and the receiver is obstructed by a surface with sharp irregularities or small openings. Scattering is the phenomena that forces the radiation of an electromagnetic wave to deviate from a straight path by one or more obstacles, with small dimensions compared to the wavelength. Those obstacles such as street signs or lamp posts are referred to as the scatters.

One of the main source of signal degradation in a wireless channel is a phenomenon called fading, the variation of the signal amplitude over time and frequency domains. Fading may either due to multipath propagation, or to shadowing from obstacles that affect the propagation of a radio wave. the fading phenomenon can be classified into two different types: large-scale fading and small-scale fading. Large-scale fading occurs as the mobile moves through a large distance. It is caused by path loss of signal as a function of distance and shadowing by large objects. Small-scale fading refers to rapid variation of signal levels due to the interference of multiple signal paths (multi-paths) when the mobile station moves short distances.

The frequency selectivity of a channel is characterized (e.g., by frequency-selective or frequency flat) for small-scale fading. Meanwhile, depending on the time variation in a channel due to mobile speed (characterized by Doppler spread) short-term fading

can be classified as either fast fading or slow fading. Figure 3.9 describes the types of fading channels.

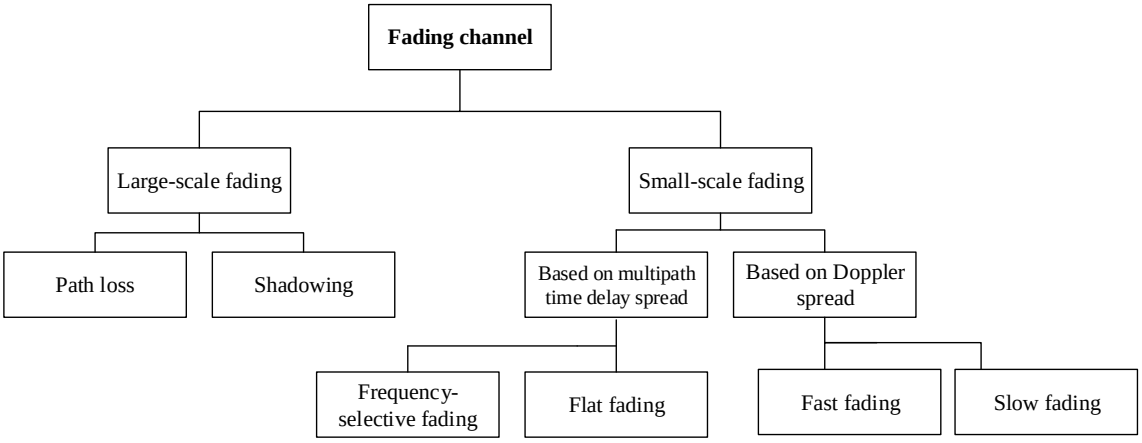

Figure 3.9: Types of fading channels [47], [45].

The relationship between large-scale fading and small-scale fading is illustrated in Figure 3.9. Large-scale fading is determined by the mean path loss and shadowing that varies along the mean path loss. Typically the scattering components incur small-scale fading which yields a short-term variation of the signal that is already experiencing shadowing.

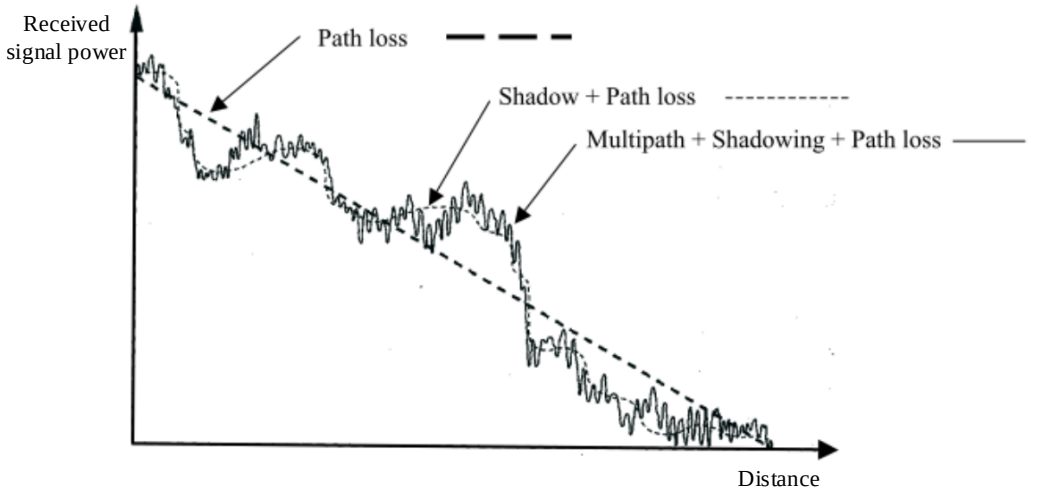

Figure 3.10: Large-scale fading vs. small-scale fading [43].

3.2.1 Large-scale channel fading

As stated above, large-scale fading consists in path loss (PL) and shadowing effects. Next, both fading effects are described.

3.2.1.1 Path loss

The path loss is defined as the ratio of the received signal power to the transmit signal power, which describes the attenuation of the mean power as function of distance between transmitter and receiver. In particular, at mmWave frequencies, the PL is much more severe than at lower frequencies since the free space, for example at 60 GHz, PL increases approximately 22 dB compared to 5 GHz band [1]. Additionally, the path loss at 60 GHz is subjected to additional losses due to oxygen absorption and rain attenuation. This conditions makes 60 GHz bandwidth a promising candidate for multi-gigabit wireless transmission for indoor rather than outdoor applications.

According to [1] and ignoring the PL frequency dependency, the PL as function of distance, d can be given by

$$PL(d) = \bar{PL}(d) + X_\sigma \ \ [dB], \tag{3.11}$$

, where $\bar{PL}(d)$ denotes the average PL and X_σ represents the shadowing fading. In general, $\bar{PL}(d)$ is expressed as

$$\bar{PL}(d) = PL(d_0) + 10nlog_{10}(\frac{d}{d_0}) + \sum_{q=1}^{Q} X_q \ \ [dB], for\ d \geq d_0, \tag{3.12}$$

, where d_0 and n denote the reference distance and PL exponent, respectively. Typically, $d_0 = 1$ m is used as the reference. The term X_q account for the additional attenuation due to specific obstruction by objects.

3.2.1.2 Shadowing

Shadowing effect describes the average signal power receiver over a large area (a few tens of wavelengths) due to the dynamic evolution of propagation paths, whereby new paths arise and old paths disappear [1]. Due to the variation in the environment, the received signal power will be different from the mean value for a given distance, which causes the PL variation about the mean of PL value, as shown in 3.12.

Several measurements have shown that the shadowing fading is log-normally distributed, thus X_q denotes a zero-mean Gaussian random variable with standard devi-

ation σ_S [48]. The value of σ_S is always referred to a specific environment.

3.2.2 Small-scale channel fading and multipath

Small-scale fading is caused by the multipath signals that arrive at the receiver with random phases that add constructively or destructively. It causes rapid changes in signal strength over a small travel distance or time interval, it causes random frequency modulation due to the varying Doppler shifts on different multipath signals, and finally it can cause time dispersion (echoes) caused by multipath propagation delays.

There are many physical factors in radio propagation channels that influence small-scale fading of which stands out the multipath propagation, speed of the mobile and the surrounding objects and the transmission bandwidth of the signal [45].

Next, several parameters that helps to characterize a small-scale channel fading and the multipath phenomenon are described.

3.2.2.1 Doppler shift

Due to the relative motion between a mobile and a base station, each multipath wave experiences a shift in frequency. This shift in received signal frequency is called Doppler shift and it is directly proportional to the velocity and direction of motion of the mobile relatively to the direction of arrival of the received multipath wave.

Considering a mobile moving at a constant velocity v and angle between the direction of the mobile's motion and the direction of arrival of the wave θ (Figure 3.11), the Doppler shift f_d is given by (3.13)

$$f_d = \frac{v}{\lambda} cos(\theta) \tag{3.13}$$

,where λ denotes the wavelength which is

$$\lambda = \frac{c}{f_c} \tag{3.14}$$

,where c is the velocity of the light and f_c represents the transmitter operating frequency

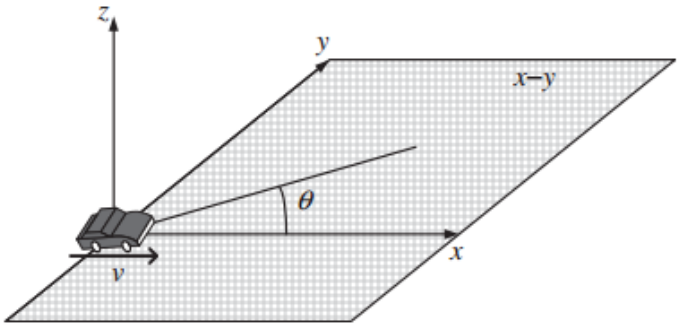

Figure 3.11: Illustration of Doppler effect [49].

[45].

3.2.2.2 Time dispersion parameters

In order to compare different multipath channels, parameters which quantify the multipath fading channel are used. The mean excess delay, RMS delay spread and excess delay spread are multipath channels parameters that can be determined from a power delay profile (PDP).

The mean excess delay is the first moment of the power delay profile and is defined to be [45]

$$\overline{\tau} = \frac{\sum_i P(\tau_i)\tau_i}{\sum_i P(\tau_i)} \tag{3.15}$$

The RMS delay spread is the square root of the second central moment of the PDP and it is defined by

$$\tau_{rms} = \sqrt{\overline{\tau^2} - (\overline{\tau})^2}, \tag{3.16}$$

where,

$$\overline{\tau^2} = \frac{\sum_i P(\tau_i)\tau_i^2}{\sum_i P(\tau_i)}, \tag{3.17}$$

Both RMS delay spread and mean excess delay are defined from a single PDP

which is the temporal or spatial average of consecutive impulse response measurements collected and averaged over a local area.

The maximum excess delay (τ_{max}) of the PDP is defined to be the time delay during which multipath energy is x dB below the strongest arriving multipath signal.

3.2.2.3 Coherence bandwidth

The B_c is a key metric involved in expressing the performance of any digital wireless system over a fading channel, since if the system requires a bandwidth larger than B_c of the channel, amplitude and phase distortion of the signal will occur. In this case, the fading channel is considered as a frequency-selective fading, making the digitally modulated data experience ISI. Coherence bandwidth is normally defined as the maximum frequency difference at which two signals are highly correlated and a correlation of 0.9 ($B_{c_{0.9}}$) is most commonly used. It can be calculated by (3.18), which is the Frequency Correlation Function (FCF).

$$\rho(n) = \sum_{n=0}^{N-h-1} H(n)H^*(n+h) \tag{3.18}$$

where, $H(n)$ is the complex transfer function of the channel, h represents the frequency shift, * denotes the complex conjugate and N is the number of channel realizations.

According to [45], the coherence bandwidth can also be related with the RMS delay spread as

$$B_{c_{0.9}} = \frac{1}{50\tau_{rms}} \tag{3.19}$$

3.2.2.4 Doppler spread and coherence time

Doppler spread and coherence time are parameters used to describe the time varying nature of the channel in a small-scale region. Doppler spread B_D is defined as a range of frequencies over which the received Doppler spectrum is non-zero. If the baseband

signal bandwidth is much greater than B_D the effects of Doppler spread are negligible at the receiver, which means a slow fading channel. Coherence time is the time domain dual of Doppler spread and is used to characterize the time varying nature of the frequency dispersiveness of the channel in time domain. In other words, coherence time measures the time duration over which the channel impulse response is considered invariant. According to [45] and [50] the coherence time (T_{coh}) can be approximated to

$$T_{coh} \approx \frac{1}{2f_d} \tag{3.20}$$

, where f_d denotes the Doppler shift.

3.2.2.5 Indoor multipath fading channel model

It has been verified by several measurements of the indoor channel that arrivals of the multipath-delayed components can be modeled as a Poisson process, more specifically by Saleh and Valenzuela (SV)channel model [51]. Figure 3.12 illustrates the SV channel model with multiple clusters, each of which is associated with a set of rays.

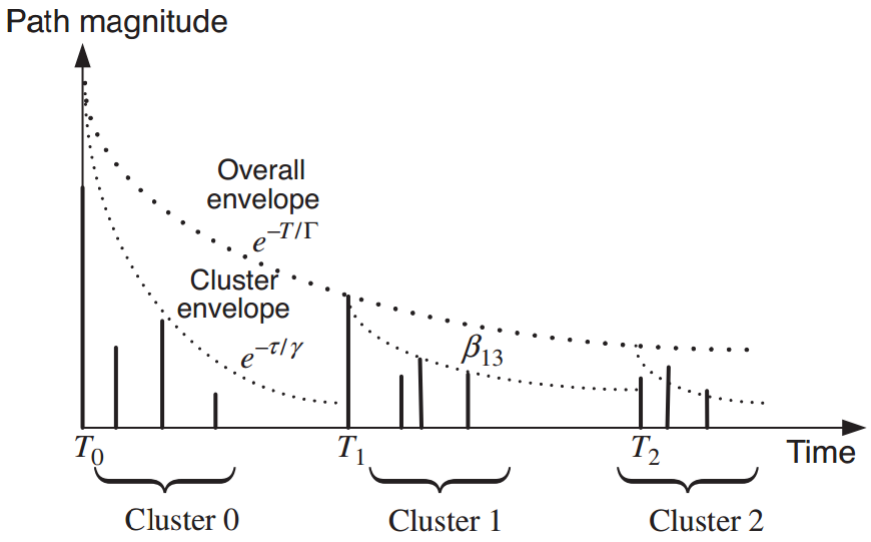

Figure 3.12: Saleh-Valenzuela channel model [51].

The arrival time of the first ray in the l^{th} cluster, denoted by T_l is modeled by a Poisson process with an average arrival rate of Λ while the arrival times of rays in each cluster is modeled by a Poisson process with an average arrival rate of λ. Thus, the distribution of inter-cluster arrival times and inter-ray arrival times are given by the following distributions, respectively:

$$f_{T_l}(T_l|T_{l-1}) = \Lambda e^{[-\Lambda(T_l - T_{l-1})]},\ l = 1, 2, ... \tag{3.21}$$

and

$$f_{\tau_{k,l}}(\tau_{k,l}|\tau_{k-1,l}) = \lambda e^{[-\lambda(\tau_{k,l} - \tau_{k-1,l})]},\ k = 1, 2, ... \tag{3.22}$$

, where $\tau_{k,l}$ denotes the arrival time of the k^{th} ray in the l^{th} cluster. According to [1] and [22], a generic 60 GHz channel model can be characterized based on the clustering phenomenon observed in temporal and spatial domains. Thus, the proposed cluster model is based on the extension of the Saleh-Valenzuela model to the angular domain by Spencer et al. [52] and the complex baseband channel impulse response (CIR) is given by

$$h(t, f) = \sum_{l=0}^{L} \sum_{k=0}^{K_l} \alpha_{k,l} \delta(t - T_l - \tau_{k,l}) \delta(f - \Omega_l - \omega_{k,l}) \tag{3.23}$$

, where $\delta(.)$ is the Dirac delta function, L is the total number of clusters and K_l is total number of rays in the l^{th} cluster. The scalars $\alpha_{k,l}$ and $\omega_{k,l}$ denote the complex amplitude, time of arrival (ToA) and angle of arrival (AoA), respectively. Similarly, T_l, Ω_l represent the mean ToA, and mean AoA of the k^{th} ray of the l^{th} cluster.

According to [22], when directive antennas are used in a LOS scenario, it appears a strong LOS path on top of the clustering phenomenal. This LOS path can be included by adding a LOS component to (3.23) as follows

$$h(t, f) = bd(t, f) + \sum_{l=0}^{L} \sum_{k=0}^{K_l} \alpha_{k,l} \delta(t - T_l - \tau_{k,l}) \delta(f - \Omega_l - \omega_{k,l}) \tag{3.24}$$

, where $bd(t, f)$ represents the LOS component, i.e., the multipath gain of the first arrival path which can be determined using ray tracing or simple geometrical based method or statistically.

Figure 3.13 shows the CIR described in (3.24).

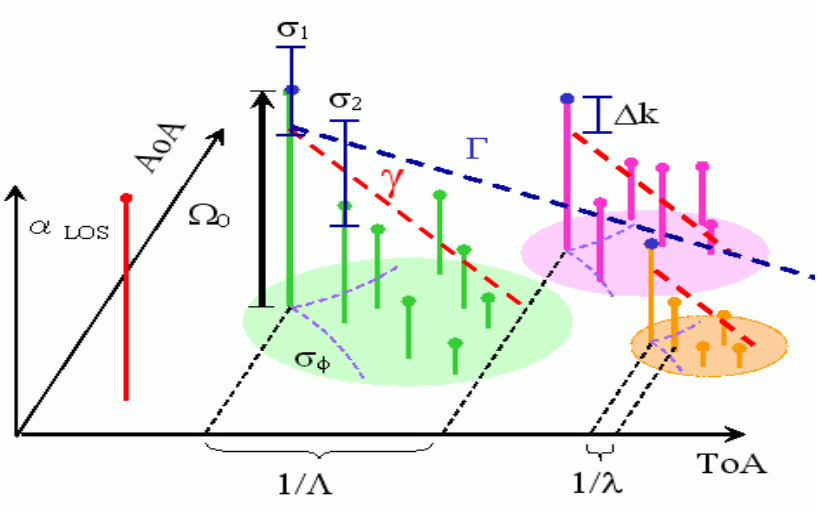

Figure 3.13: Graphical representation of the CIR as function of ToA and AoA [22].

3.3 Channel coding

In a OFDM system, some consecutive subcarriers may suffer from deep fading, in which the received SNR is bellow the minimum-defined SNR, as depicted in Figure 3.14. This fact leads to errors in the subcarriers affected by deep fading, which decreases the communications system performance [43]. In order to avoid it, it is essential to employ FEC (Forward Error correction) codes. The most popular FEC codes associated with coded OFDM systems includes Reed-Solomon (RS) codes convolutional codes and low-density parity-check (LDPC) codes.

One way to classify different codes is to distinguish between block codes, where the redundance is added to blocks of a data and convolutional codes, where redundancy is added continuously. Block codes are well suited for correcting burst errors while convolutional codes have the advantage that they are easily decoded using Viterbi decoder [42]. Convolutional codes also offer the possibility of be concatenated with block codes.

3.3.1 Reed-Solomon (RS) codes

Reed-Solomon codes are non binary block codes with symbols made up of m-bit sequences where m is any positive integer greater than 2. RS(n,k) codes on m-bit symbols

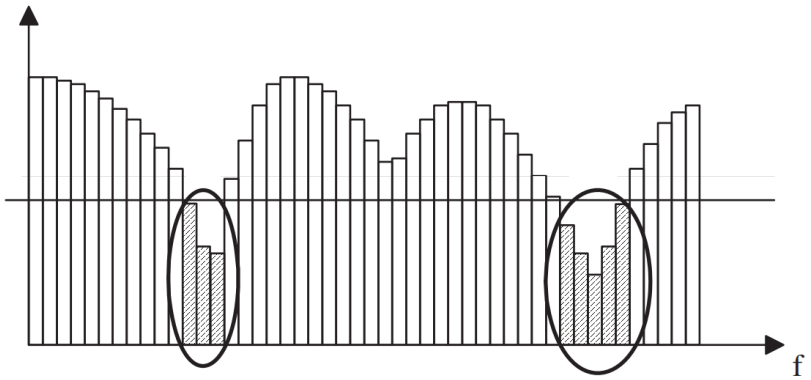

Figure 3.14: Errors due to deep fading [43].

exist for all n and k for which

$$0 < k < n < 2^m + 2 \tag{3.25}$$

,where k is the number of data symbols to be encoded, and n is the total number of code symbols in the encoded block. Typically, n corresponds to $2^m - 1$, while k is given by $2^m - 1 - 2t$, where t is the symbol-error correcting capability of the code, and $n - k = 2t$ is the number of parity symbols. The generating polynomial for an RS code takes the following form [46]:

$$g(X) = g_0 + g_1 X + g_2 X^2 + ... + g_{2t-1} X^{2t-1} + X^{2t} \tag{3.26}$$

Note that the degree of the generator polynomial is equal to the number of parity symbols.

3.3.2 Low-density parity-check (LDPC) codes

The most straightforward encoding is a mapping table, where any K-valued information word is associated with an N-valued codeword. Thus, the table just checks the input, and reads out the associated codeword. However, this method is highly inefficient, since it requires the storing of 2^k codewords. Linear codes considers that any codeword can be created by a linear combination of other codewords, so that is sufficient to store a subset of codewords. Thus, the encoding process using linear codes can be described by a matrix multiplication [42]:

$$x = uG \tag{3.27}$$

, where x denotes the N-dimensional codevector, u is the K-dimensional information vector and G denotes the $K \times N$-dimensional generator matrix.

In order to decide whether the received codeword is a valid codeword, it is multiplied by a parity check matrix H. This results in a $N-K$-dimensional called syndrome vector. If this vector has all-zero entries, then the received codeword is valid. The H-matrix is achieved ensuring that the relationship $H.G^T = 0$ is true [42].

LDPC codes are linear block codes, which means that the original sequence of bits (k) can be segmented into fixed message blocks with length n, where n is composed by k and redundant information. In other words, the LDPC encoder converts each input message block into a code word block.

The LDPC codes are defined via the parity check matrix (H). Besides most of the times the dimensions of matrix H be relatively large, the number of nonzero entries are kept low [42].LDPC codes are characterized by two parameters: p and q and are usually represented as LDPC(p,q), where p denotes the number of 1's in each column of the parity check matrix and q denotes the number of 1's in each row. If all rows are linearly independent, then the resulting code rate is $(q-p)/q$. An example of a parity check matrix from a LDCP(3,4) code is presented bellow [42].

$$\mathbf{H} = \begin{bmatrix}
1&1&1&1&0&0&0&0&0&0&0&0&0&0&0&0&0&0&0&0\\
0&0&0&0&1&1&1&1&0&0&0&0&0&0&0&0&0&0&0&0\\
0&0&0&0&0&0&0&0&1&1&1&1&0&0&0&0&0&0&0&0\\
0&0&0&0&0&0&0&0&0&0&0&0&1&1&1&1&0&0&0&0\\
0&0&0&0&0&0&0&0&0&0&0&0&0&0&0&0&1&1&1&1\\
1&0&0&0&1&0&0&0&1&0&0&0&1&0&0&0&0&0&0&0\\
0&1&0&0&0&1&0&0&0&1&0&0&0&0&0&0&1&0&0&0\\
0&0&1&0&0&0&1&0&0&0&0&0&0&1&0&0&0&1&0&0\\
0&0&0&1&0&0&0&0&0&0&1&0&0&0&1&0&0&0&1&0\\
0&0&0&0&0&0&0&1&0&0&0&1&0&0&0&1&0&0&0&1\\
1&0&0&0&0&1&0&0&0&0&0&1&0&0&0&0&0&1&0&0\\
0&1&0&0&0&0&1&0&0&0&1&0&0&0&0&1&0&0&0&0\\
0&0&1&0&0&0&0&1&0&0&0&0&1&0&0&0&0&0&1&0\\
0&0&0&1&0&0&0&0&1&0&0&0&0&1&0&0&1&0&0&0\\
0&0&0&0&1&0&0&0&0&1&0&0&0&0&1&0&0&0&0&1
\end{bmatrix}$$

Since LDPC codes are defined via their parity check matrix, the encoding process is more complicated when compared to "normal" block codes. For LDPC codes, the generator matrix is not known, but it can be computed using Gaussian elimination and reordering of columns in order to cast the parity check matrix in the form:

$$\tilde{H} = (-P^T \; I) \tag{3.28}$$

The corresponding generator matrix is then

$$G = (I \ P) \tag{3.29}$$

The sparse structure of the parity check matrix is a complex process for decoding purposes. It requires a exact maximum likelihood decoding, which means that it is needed to check all possible codewords, and compare them with the received signal.

3.3.3 Convolutional codes

A convolutional code is generated by passing the information sequence to be transmitted through a linear finite-state shift register. In general, the shift register consists of K stages and n linear algebraic function generators, as shown in Figure 3.15. The number of output bits for each k-bit input sequence is n bits. Consequently, the code rate is defined as k/n.

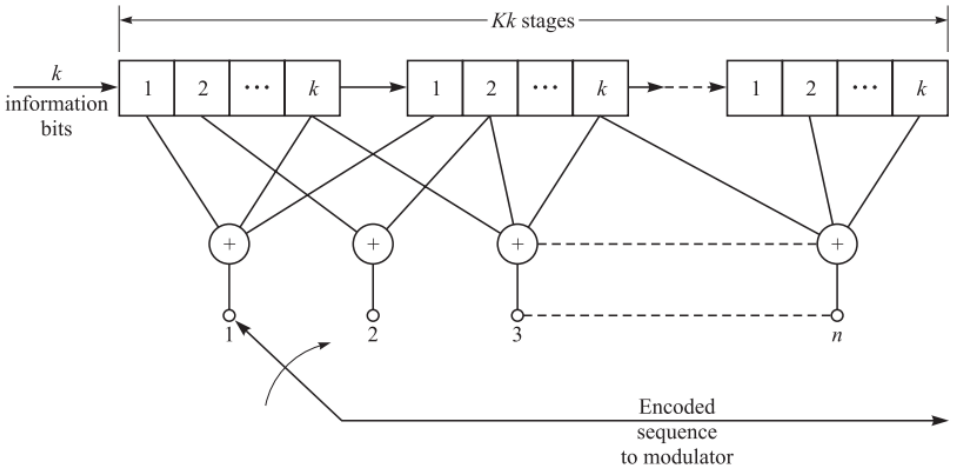

Figure 3.15: Convolutional encoder. [53]

One method to describing a convolutional code is to give its generator matrix, as explained in Section 3.3.2 [53].

3.3.4 Concatenated codes

In concatenated coding two codes, one binary and one non binary are concatenated such that the codewords of the binary code are treated as symbols of non binary code. The binary code that is directly connected to the binary channel is called inner code, and the non binary code is called the outer code.

Figure 3.16 shows a typical concatenated cdingscheme. The codewords are formed by subdividing a block of k K information bits into K groups, called symbols, where each symbol consists of k bits. The K k-bit symbols are encoded into N k-bit symbols by the outer encoder, as is usually done with a non binary code. The inner encoder takes each k-bit symbol and encodes it into a binary block code of length n. Thus, it is obtained a concatenated block code having a block length of Nn bits and containing kK information bits. that means an equivalent (Nn, kk) long binary code.

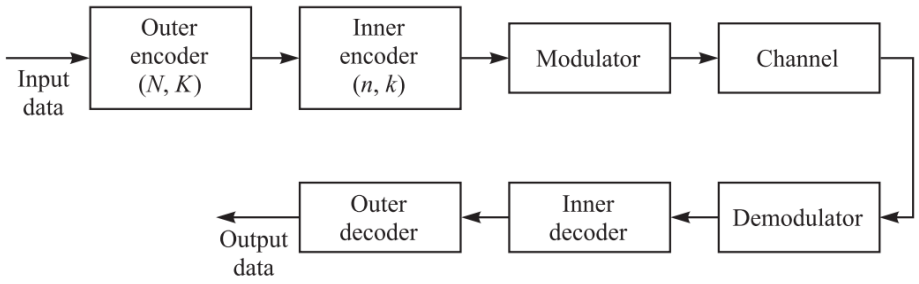

Figure 3.16: Concatenated coding scheme. [53]

Additionally, the rate of the concatenated code is Kk/Nn, which is equal to the product of the two code rates.

A hard decision decoder for a concatenated code is conveniently separated into an inner decoder and an outer decoder (Figure 3.16). Typically, the inner decoder takes the hard decisions on each group of n bits, corresponding to a codeword of the inner code, and makes a decision on the k information bits based on maximum-likelihood (minimum distance) decoding. When a block of N k-bit symbols is received from the inner decoder, the outer decoder makes a hard decision on the K k-bit symbols, also based on maximum-likelihood decoding. Note that soft decision is commonly used over fading channels.

Concatenated codes with Reed-Solomon codes as the outer code and binary convolutional codes as the inner code have been widely used in the design of communication systems over fading channels [53].

3.4 Channel Estimation and Frequency Domain Equalization

In a OFDM system, the received signal is usually distorted by the channel characteristics. In order to recover the transmitted bits, the channel effect must be estimated and compensated in the receiver through a equalization process. In general, the channel can be estimated either using a preamble or interleaving pilot symbols with data symbols known to both transmitter and receiver.

In this work channel estimation using pilot tones and channel estimation sequences (CES) are studied and their performance is compared.

3.4.1 Pilot-based channel estimation

If no ICI occurs, each subcarrier can be seen as an independent channel, and thus the orthogonality among subcarriers is preserved. The orthogonality allows each subcarrier component of the received signal to be expressed as the product of the transmitted signal and channel frequency response (CFR) at the subcarrier [43].Thus, the transmitted signal can be recovered by estimating the CFR at each subcarrier by employing interpolation techniques.

There are three different types of pilot structures that must be considered: block type, comb type and lattice type [43].

3.4.1.1 Block type

In block type, OFDM symbols with pilots assigned at all subcarriers are transmitted periodically for channel estimation purposes, as depicted in Figure 3.17 .This pilot arrangement enables a time-domain interpolation can be performed to estimate the channel along with the time axis. The period of pilot symbols (S_t) must be given by

$$S_t \leq \frac{1}{2f_d} \tag{3.30}$$

, where f_d denotes the maximum Doppler frequency which was described in Section 3.2.2.The block type pilot arrangement is suitable for frequency-selective channels.

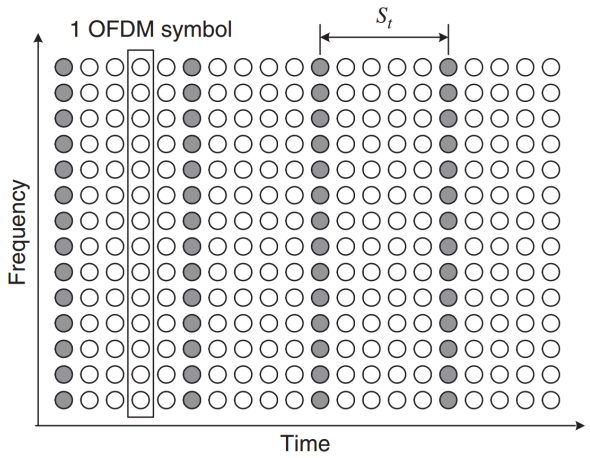

Figure 3.17: Block type pilot arrangement [43]

3.4.1.2 Comb type

With comb type pilot arrangement every symbol has pilot tones at the periodically-located subcarriers (Figure 3.18). Thus, a frequency-domain interpolation is used to estimate the channel along the frequency axis. In order to keep tracking of the frequency selective channel characteristics, the pilot tones must be placed as frequently as coherence bandwidth is. If we consider the coherence bandwidth as the inverse of the maximum delay spread (τ_{max}) [43], the pilot symbol period (S_f) must satisfy the following inequality:

$$S_f \leq \frac{1}{\tau_{max}} \tag{3.31}$$

This pilot arrangement type is suitable for fast-fading channel, but not for frequency-selective channels.

3.4.1.3 Lattice type

The pilot tones in lattice type are scattered in both time and frequency domain, as shown in Figure 3.19. In order to track both time-varying and frequency-selective channel characteristics, the pilot symbol arrangement must satisfy both Eq. 3.30 and Eq. 3.31.

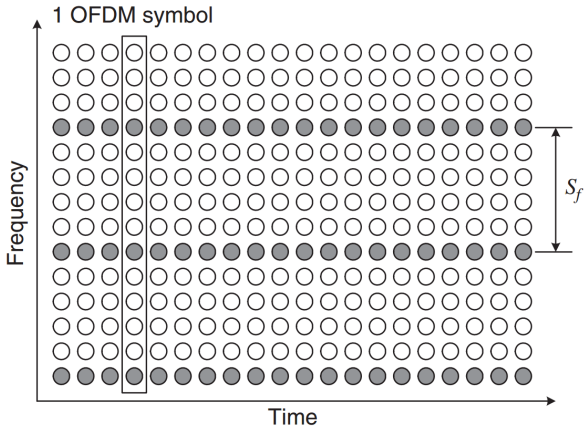

Figure 3.18: Comb type pilot arrangement [43]

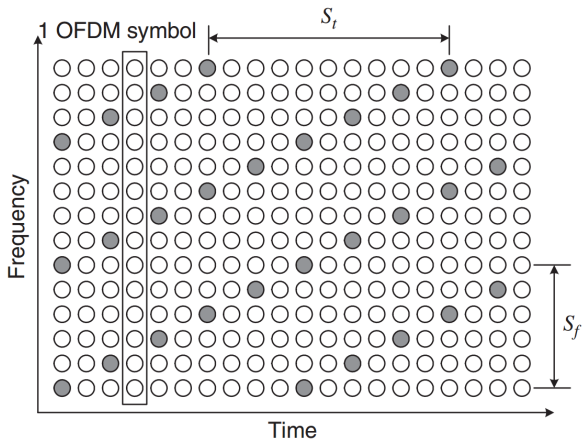

Figure 3.19: Lattice type pilot arrangement [43]

3.4.1.4 LS channel estimation

The least-square (LS) channel estimation method is widely used for channel estimation when training symbols are transmitted, which is the case of pilot tones and CES. Assuming that all subcarriers are orthogonal (i.e., ICI free), the pilot tones for N subcarriers can be represented by the following diagonal matrix [43]:

$$X = \begin{bmatrix} X[0] & 0 & \dots & 0 \\ 0 & X[1] & & \vdots \\ \vdots & & \ddots & 0 \\ 0 & \dots & 0 & X[N-1] \end{bmatrix}$$

, where $X[k]$ denotes a pilot tone at the k^{th} subcarrier, $K = 0, 1, 2, \dots, N-1$. The amplitude of the received pilot subcarriers Y can be represented as

$$Y = XH + Z \Leftrightarrow$$

$$\Leftrightarrow \begin{bmatrix} Y[0] \\ Y[1] \\ \vdots \\ Y[N-1] \end{bmatrix} = \begin{bmatrix} X[0] & 0 & \dots & 0 \\ 0 & X[1] & & \vdots \\ \vdots & & \ddots & 0 \\ 0 & \dots & 0 & X[N-1] \end{bmatrix} \begin{bmatrix} H[0] \\ H[1] \\ \vdots \\ H[N-1] \end{bmatrix} + \begin{bmatrix} Z[0] \\ Z[1] \\ \vdots \\ Z[N-1] \end{bmatrix} \quad (3.32)$$

, where H is the channel vector, and Z represents the noise vector.

The LS estimator finds the channel estimate $\hat{H}$ in a way that the cost function (3.33) is minimized as shown in (3.34)

$$\begin{aligned} J(\hat{H}) &= ||Y - X\hat{H}||^2 \\ &= (Y - X\hat{H})^*(Y - X\hat{H}) \\ &= Y^*Y - Y^*X\hat{H} - \hat{H}^*X^*Y + \hat{H}^*X^*X\hat{H} \end{aligned} \quad (3.33)$$

, where * denote the complex conjugate.

$$\frac{\partial(J(\hat{H}))}{\partial(\hat{H})} = 0 \quad (3.34)$$

From (3.34) it is obtained the following equality:

$$X^*X\hat{H} = X^*Y \quad (3.35)$$

which gives the solution for the LS channel estimation as stated in [43], [54]

$$\hat{H}_{LS} = (X^*X)^{-1}X^*Y = X^{-1}Y \quad (3.36)$$

This channel estimation technique is a more appropriated approach in terms of low computational requirements, compared with other methods [55] [56].

3.4.1.5 Interpolation techniques

In comb-type pilot-based channel estimation the amplitude of data symbols between pilot subcarriers must be estimated in order to have a fully estimated frequency response of a transmission channel. For that, interpolation techniques are applied to the estimated pilot subcarriers. Popular interpolation methods include linear interpolation, second order interpolation, and cubic spline interpolation [43].

According to [57] ,the channel estimation at the data subcarrier k using linear interpolation is given by Eq.3.37.

$$\begin{aligned} \hat{H}(k) &= \hat{H}(mL+n) \\ &= [\hat{H}_{LS}(m+1) - \hat{H}_{LS}(m)]\frac{n}{L} + \hat{H}_{LS}(m) \end{aligned} \tag{3.37}$$

where $mL < k < (m+1)L$ and $0 \leq n < L$ and $m = 0, 1, \ldots, N_p - 1$, where N_p denotes the number of pilot subcarriers. Note that in this equation only two pilots are used for channel estimation at the data subcarriers.

Second order interpolation performs better than the linear interpolation, since the channel estimation at the data subcarriers is calculated by using a linear combination of three adjacent pilots [58]. The channel estimation of second order interpolation is given by

$$\begin{aligned} \hat{H}(k) &= \hat{H}(mL+n) \\ &= c_1\hat{H}_{LS}(m-1) + c_0\hat{H}_{LS}(m) + c_{-1}\hat{H}_{LS}(m+1) \end{aligned} \tag{3.38}$$

,where

$$\begin{cases} c_1 = \frac{\alpha(\alpha-1)}{2}, \\ c_0 = -(\alpha-1)(\alpha+1), \\ c_{-1} = \frac{\alpha(\alpha+1)}{2}, \\ \alpha = \frac{l}{N} \end{cases} \tag{3.39}$$

Cubic spline interpolation method allows a smooth and continuous polynomial fitted [58] which is given by:

$$\begin{aligned}\hat{H}(k) &= \hat{H}(mL+n) \\ &= \alpha_1 \hat{H}_{LS}(m+1) + \alpha_0 \hat{H}_{LS}(m) + L\alpha_1 \hat{H'}_{LS}(m+1) - L\alpha_0 \hat{H'}_{LS}(m)\end{aligned} \tag{3.40}$$

, where $\hat{H'}_{LS}(m)$ is the first order derivative of $\hat{H}_{LS}(m)$, and

$$\begin{cases} \alpha_1 = \frac{3(L-l)^2}{L^2} - \frac{2(L-l)^3}{L^3}, \\ \alpha_0 = \frac{3l^2}{L^2} - \frac{2l^3}{L^3} \end{cases} \tag{3.41}$$

3.4.2 Golay Complementary Sequences

Golay complementary sequences (GCS) are widely used in the preamble of OFDM and SC systems for synchronization and as channel estimation sequences (CES) for channel estimation purposes [7]. Golay sequences are pair of sequences which has an attractive property that the sum of their auto-correlations has maximum peak with zero side-lobes [59, 7], which allows to remove ISI in order to improve the accuracy of channel estimation. Let a_N and b_N be the pairs of Golay sequences of length equal to $N = 2^M$ (M natural number) and $[R_a, R_b]$ the auto-correlation of each pair respectively, where the sum both auto-correlations is defined by

$$R_{ab}(i) = R_a(i) + R_b(i) = 2N\delta(i) \tag{3.42}$$

$$R_a(i) = \sum_{n=0}^{N-i-1} a_N(n+i) \times a_N^*(n) \tag{3.43}$$

$$R_b(i) = \sum_{n=0}^{N-i-1} b_N(n+i) \times b_N^*(n) \tag{3.44}$$

,where $i \in [0, ..., N-1]$ and $\delta(i)$ denotes the Kronecker delta function.

Golay sequences are generated by delay and weigth vectors and a recursive algorithm, as shown in Figure 3.20

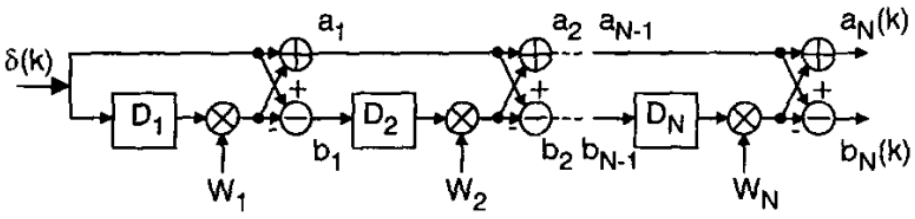

Figure 3.20: Recursive complementary sequence generator [60].

The channel estimation sequence is based on complementary Golay sequences which are made up of two parts: a part and b part. Typically, CES has a regular configuration, namely N_R repetitions of base sequences with length N and cyclic prefix and postfix with length N_{CP}, as shown the example of Figure 3.21. The base sequences for a part and b part are Golay sequences a_N and b_N, respectively.

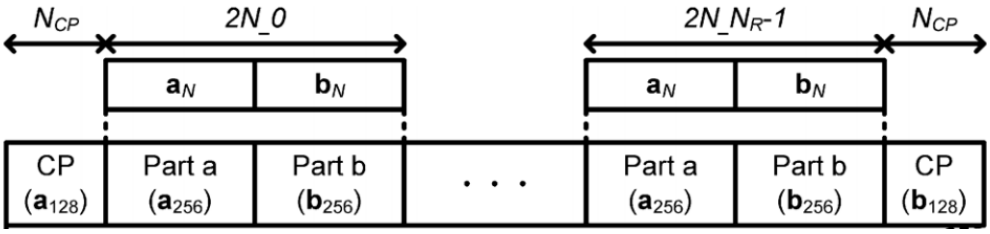

Figure 3.21: CES based on Golay complementary sequences. [9]

The received i^{th} r_{CES} can be expressed as

$$r_{CES}(i) = \sum_{n=0}^{N_{CH}-1} h(n) \times s_{CES}(i-n) + n(i) \tag{3.45}$$

,where s_{CES} is the channel estimation sequence, h is the time domain CIR, N_{CH} is the length of CIR and n represents AWGN noise.

The Golay correlator is used to calculate the correlation values $\alpha(i)$ and $\beta(i)$ between the received CES and Golay sequences. It is implemented according the diagram shown in figure 3.22 and the correlation values can be expressed as (3.46) and shown in (3.47).

$$\alpha(i) = \frac{1}{N} \sum_{n=0}^{N-1} r_{CES}(i+n) \times a_N^*(n) \tag{3.46}$$

$$\beta(i) = \frac{1}{N} \sum_{n=0}^{N-1} r_{CES}(i+n) \times b_N^*(n) \tag{3.47}$$

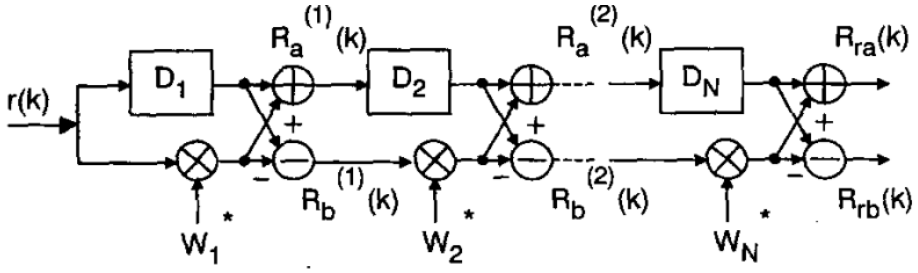

Figure 3.22: Efficient Golay correlator [60].

After removing CP from the correlation values, they are aligned to the beginning of each Golay sequence and denoted as $\hat{\alpha}(i)$ and $\hat{\beta}(i)$. Finally, the estimated channel h_{est} can be acquired as

$$h_e st(i) = \frac{1}{N_R} \sum_{p=0}^{N_R-1} (\hat{\alpha}(i + p \times 2N) + \hat{\beta}(i + p \times 2N)) \tag{3.48}$$

Figure 3.23 shows the auto correlation results of two parts of length 256 and the corresponding sum result [7]. As expected, it can be seen that the sum of the sequences pair has a unique peak and zero side lobes, which improves the channel estimation accuracy.

3.4.3 Frequency Domain Equalization

Wireless channels can exhibit delay dispersion, i.e. multipath components can have different runtimes from the transmitter to the receiver which leads to the existence of ISI. If the delay spread becomes comparable with or larger than the symbol duration, then the BER becomes unacceptably large if no countermeasures are taken. Coding and diversity can reduce, but not completely eliminate, errors due to ISI [42]. Equalizers are receiver structures capable of reduce or eliminate ISI by reversing distortions caused by the channel. If the channel is known and static a hardware-based filter could perform a proper equalization of the transfer function. However, in a real wireless system, the channel is unknown and time variant. The unknown channel problem can be solved by transmitting a training sequence, i.e. a known sequence of bits. The time variance problem can be solved by repeating the transmission of the training sequence at a sufficiently short cadence, so that the equalizer can be adapted to the channel state at regular intervals.

Over the years, many different types of equalizers have been developed. The sim-

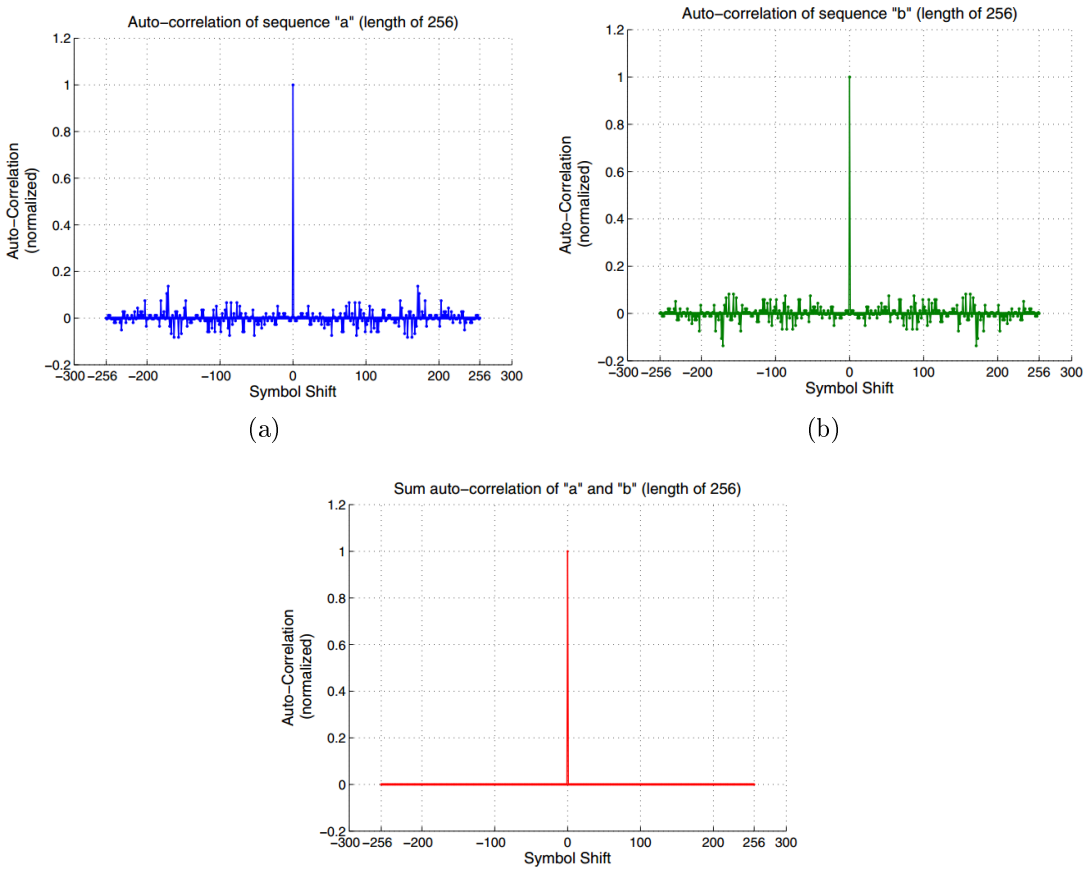

Figure 3.23: Auto-correlation of (a) sequence a and (b) b and (c) their sum auto-correlation [7].

plest is the linear equalizer, which is a tapped-delay-line filter with coefficients that are adapted to the channel state. Decision feedback filters, Maximum Likelihood Sequence Estimation (MLSE) and blind equalizers are also used for equalization purposes. This work will focus only in frequency domain linear equalizers.

Let $Y_l(k)$ be the typical received OFDM signal, in frequency domain, considering that $T_{CP} \geq \tau_{max}$:

$$Y_l(k) = H_l(k)X_l(k) + Z_l(k), \tag{3.49}$$

, where k denotes the subcarrier frequency component index of the l^{th} transmitted OFDM signal. $H_l(k)$ is the channel frequency response and $Z_l(k)$ is the AWGN in the frequency domain, respectively.

The original transmitted information, $X_l(k)$ can be recovered with frequency domain equalization (FDE). FDE can be realized as a K-branch linear feed-forward equal-

izer with $C(k)$ as the complex coefficient at the k^{th} branch (subcarrier). Linear FDE can take the form of either zero forcing (ZF) or minimum mean-square error (MMSE). If ZF equalization is considered, the FDE coefficient $C(k)$ is given by Eq.3.50 [61].

$$C_{ZF}(k) = \frac{\hat{H}(k)^*}{|\hat{H}(k)|^2} \tag{3.50}$$

If MMSE criterion is considered, the FDE coefficient becomes

$$C_{MMSE}(k) = \frac{\hat{H}(k)^*}{|\hat{H}(k)|^2 + 1/\eta} \tag{3.51}$$

, where η, * and $|.|$ denotes SNR, the conjugated transpose and module, respectively.

MMSE equalization is more appealing than ZF equalization since it can make a compromise between the residual inter-symbol interference and noise enhancement. It can minimize the combined effect of ISI and noise, which is important for equalizing the channels of sever frequency-selective fading. Figure 3.24 describes the main difference between ZF and MMSE in terms of noise enhancement [42].

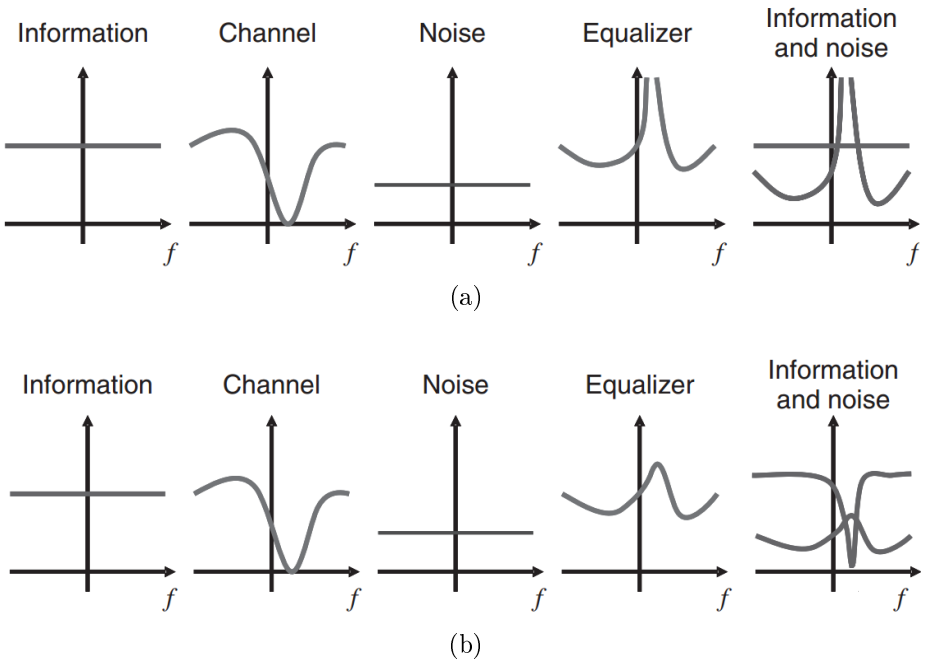

Figure 3.24: Noise enhancement in: a) ZF equalizer b) MMSE equalizer.

However, MMSE equalization needs to estimate SNR (η). Therefore the performance of MMSE-FDE is strongly dependent of the SNR accuracy estimation. In order

to estimate SNR, both signal power and noise power must be estimated. According to [61] the signal power can be estimated as

$$P_s = \frac{1}{MK} \sum_{m=1}^{M} |\hat{H}(k)|^2 \tag{3.52}$$

and the noise power can estimated as

$$P_n = \frac{1}{MK} \sum_{m=1}^{M} \sum_{k=1}^{K} |\hat{W}(m,k)|^2 \tag{3.53}$$

,where $\hat{W}(m,k) = \hat{H}(k) - \hat{H}(m,k)$, m is the index of the channel estimation sequence received and K is the FFT length.

Finally, the estimated SNR becomes

$$\hat{\eta} = \frac{P_s}{P_n} \tag{3.54}$$

Substituting $\hat{\eta}$ into (3.51), MMSE FDE coefficients results in the following equation:

$$C_{MMSE}(k) = \frac{\hat{H}(k)^*}{|\hat{H}(k)|^2 + 1/\hat{\eta}} \tag{3.55}$$

3.5 Summary

Chapter 3 presented an overview of the theoretical fundamentals considered for the presented work. The first section gives a short description of OFDM concepts as a multicarrier scheme for high data rate applications. Section 3.2 introduces the concepts related to multipath fading channels. The fading channel is subdivided in large-scale fading effects and small-scale fading effects and the parameters used to characterize this two categories of fading channel response are detailed. In Section 3.3, the most commonly used channel coding approaches are presented and the basic analytic expressions are drawn. Finally, the theoretical aspects of channel estimation based on both

pilot subcarriers and Golay sequences and frequency domain equalization are discussed in Section 3.4.

Chapter 4

Proposed OFDM-based simulation framework at 60 GHz

4.1 Introduction

In this section the OFDM-based multigigabit simulation framework is presented. First, a general description of the main blocks of the framework is described according to its block diagram, depicted in Figure 4.1. The following section refer to the detailed description of the implementation process of each block presented before. The final Section discuss the validation of the proposed simulation framework. The validation is performed through the comparison between simulation results and analytic expressions.

4.2 General overview of the proposed framework

At the transmitter, the data source block is responsible for generating binary data that are coded using a Forward Error Correction coding block. The coded bits are then mapped into a constellation of M QAM complex symbols. Next, an arrangement of the complex symbols and interleaved pilot signals are computed to generate a data sequence of length K. The K-points IFFT block transforms the data sequence into K subcarriers. Then, the CP is inserted between data in order to maintain orthogonality between subcarriers. This framework also allows the insertion of a channel estimation sequence as a prefix of the payload sequence. Finally, data is transmitted over a mmWave quasi-static multipath fading channel.

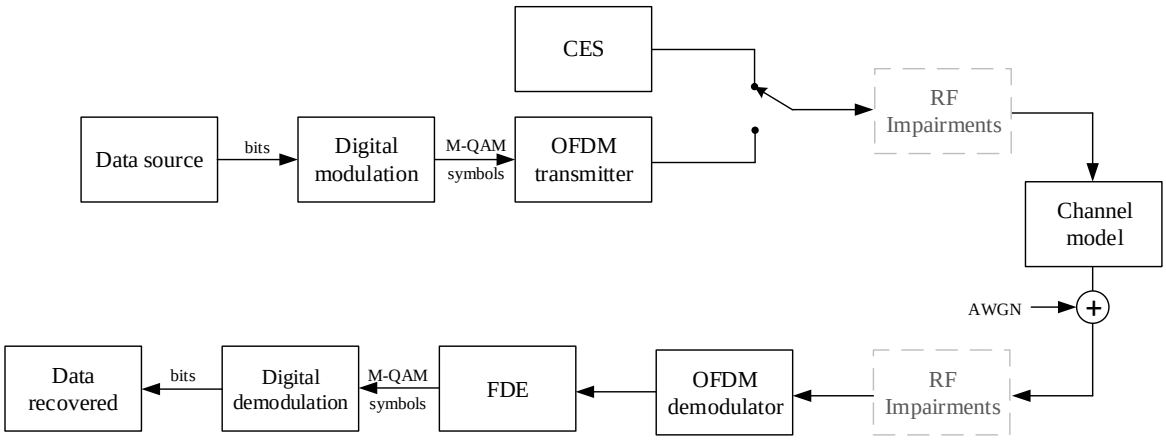

Figure 4.1: OFDM multigigabit framework block diagram.

At the receiver, a AWGN block is added in order to vary the SNR of the transmission. After removing the CP of the OFDM symbol, the received data passes through the channel estimation process that can be performed either by pilot subcarriers or through the auto-correlation of a preamble. consequently, the received data passes through a frequency-domain equalizer and then data is demapped, uncoded and finally synchronization techniques are applied.

Since the performance of OFDM at mmWave is severely affected by non-linearities of the RF front-end, the proposed framework may be extended to include RF impairments, such as phase-noise, mixer IQ imbalances, and power amplifier non-linearities.

The implementation of the simulation framework model has been performed using Simulink from Matlab, since it is a common used software tool for fast prototyping of wireless communication systems, using Digital Signal Processing (DSP) techniques [62, 63].

4.3 Data source

Data source block is composed by two main subsystems: the binary data generator and the channel coding block. Binary data can be either provided by a pseudo-random binary generator or by a multimedia binary raw file data. The proposed multigigabit framework allows the selection of either uncoded or coded transmission. If channel coding block is considered, either concatenated encoder (composed by Reed-Solomon and convolutional encoder) or LDPC coding can be employed. Figure 4.2 shows a detailed block diagram of the data source block.

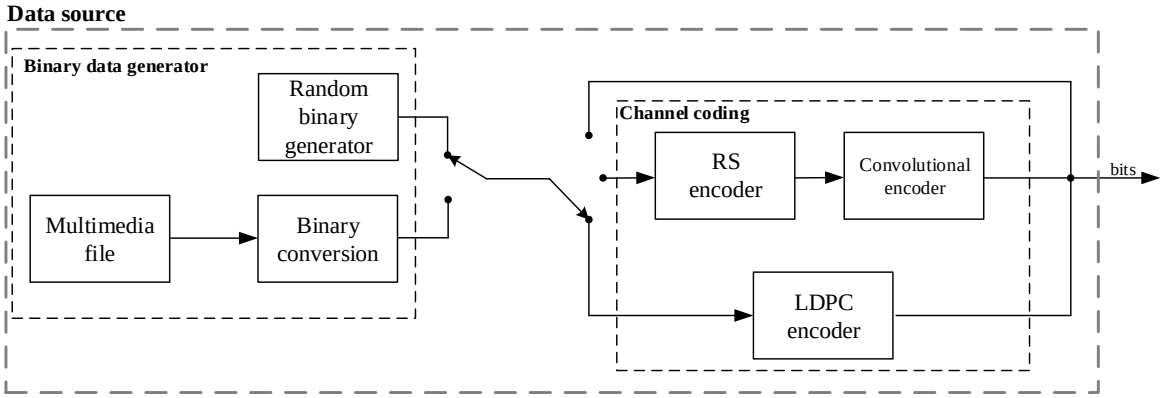

Figure 4.2: Data source block diagram.

The simulation method used in the proposed framework is frame-based, which means that data is transmitted in frames, contrary to what happens when considering sample-based method, where each sample is transmitted sequentially. Frame-based signals are obtained by buffering a batch of N samples. Thus, the output rate of the sequential frames is $1/N$ times the sample rate of the original signal [64]. Due to this fact, for computational efficiency simulation purposes, frame-based is the most suitable approach. The main parameter that must be known in order to create a frame if the size of the buffer (N) which gives the length of the frame. In this work the length of the frame ($FrameLength$) is given by the number of bits buffered before the transmission and depends on the code rate applied ($CodeRate$), the modulation order M and the number of available subcarriers for data allocation (N_{data}), as shown in (4.1). In Figure 4.3 a typical sequence of frames is depicted.

$$FrameLength = N_{data} \times log_2(M) \times CodeRate \tag{4.1}$$

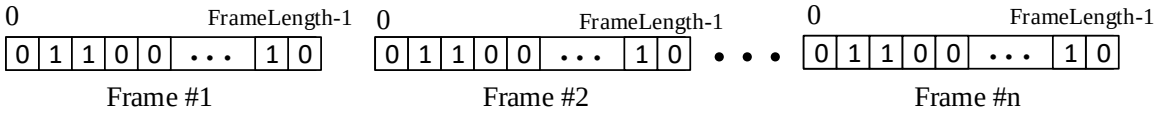

Figure 4.3: Frame sequence.

4.3.1 Binary data generator

The pseudo-random binary generator is implemented by Bernoulli Binary Generator block (Figure 4.4). It generates random bits where the probability of get a '0' is the same for generating a '1' , which is 50%. This block has as input parameters the

sample time and the number of samples per frame. The sample time describes the transmitted bit time interval, while samples per frame value indicates the number of bits contained in each frame (Figure 4.3). From Figure 4.4 can be seen that the sample time considered for the framework implementation, is given by a division between the OFDM symbol time (4.2) and the value of $FrameLength$.

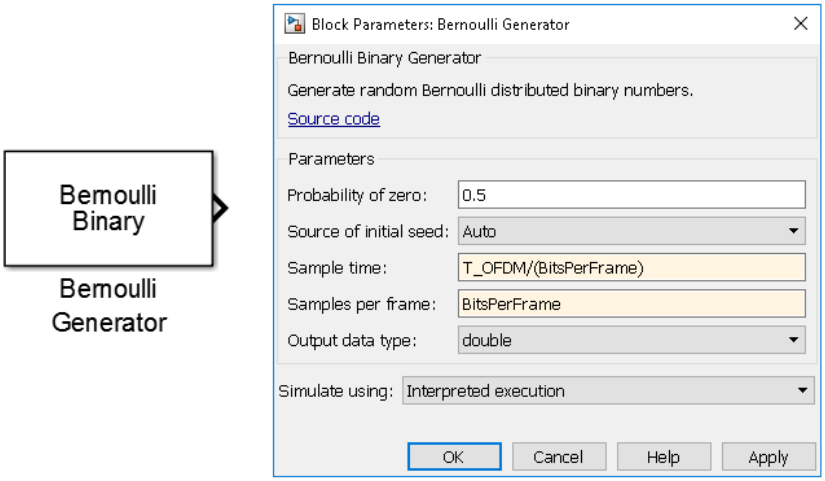

Figure 4.4: Bernoulli Generator block.

$$T_{OFDM} = N_{FFT} \times T_S + T_{CP} \tag{4.2}$$

N_{FFT} denotes the length of the FFT, T_S is the considered sampling time and T_{CP} denotes the cyclic prefix time.

Moreover, if a multimedia content is used as data source, such as a video file, the frames content must be processed ir order to be transmitted in the proposed framework. Figure 4.5 shows the typical conversion process of a video file content raw yuv data to a binary matrix of transmitted OFDM frames. Let consider that the video sequence can be divided in several frames and each frame is composed by $w \times h$ pixels. Assuming that each pixel can be represented by 255 levels (8 bits), the frame is represented by a binary matrix of $w \times h \times 8$ bits. Since the framework works in a frame-based setup, the binary data must be divided in frames with length $FrameLength$ (Eq. 4.1). This process is repeated cyclically, according to the number of frames contained in the video file.

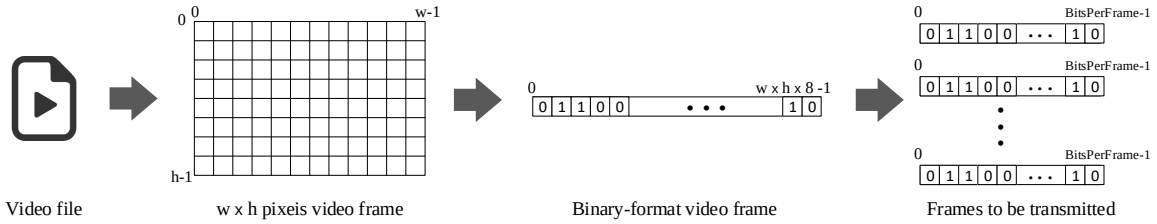

Figure 4.5: Video frame conversion.

4.3.2 Channel coding

As explained in Section 3.3, the implementation of channel coding in a wireless system aims to improve the system performance even if the subcarriers are affected from deep fading. The proposed framework allows coded transmission employing two approaches: the use of concatenated codes and LDCP FEC codes. These channel coding techniques were already presented in Section 3.3. Figure 4.6 shows in detail the concatenated encoder block diagram which consists in a concatenation of Reed-Solomon outer code and convolutional inner code.

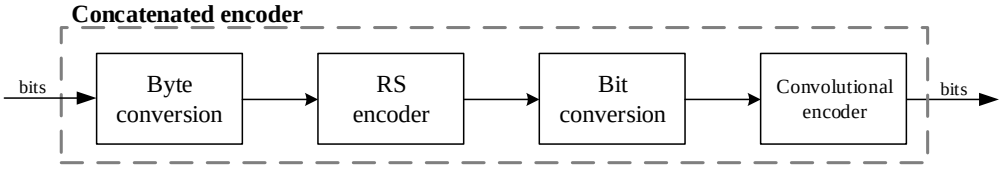

Figure 4.6: Concatenated encoder block diagram.

An implementation example of RS and convolutional coding can be seen in Figure 4.7 and Figure 4.8, respectively and it is implemented according to Section 3.3. In this case, it is considered RS(224,216) outer coding and a convolutional encoder with length 7, generator polynomial $g0 = 133o$, $g1 = 171o$, $g2 = 165o$ and code rate 2/3 [2].

The LDCP encoder has as input parameter the parity check matrix, as shown in Figure 4.9. Appendix A.4 and C.4 presents an example of parity check matrix permutations. The parity check matrix is obtained from parity check permutations using the method explained in Section 2.3.2.

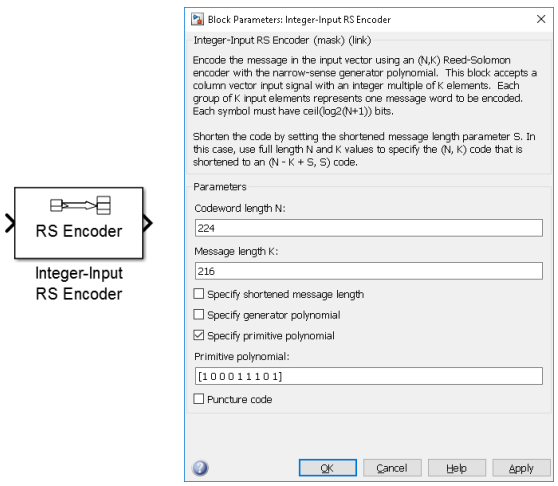

Figure 4.7: Integer-Input RS encoder.

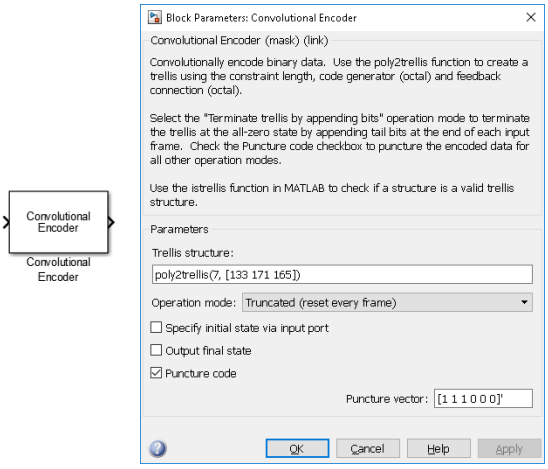

Figure 4.8: Convolutional encoder.

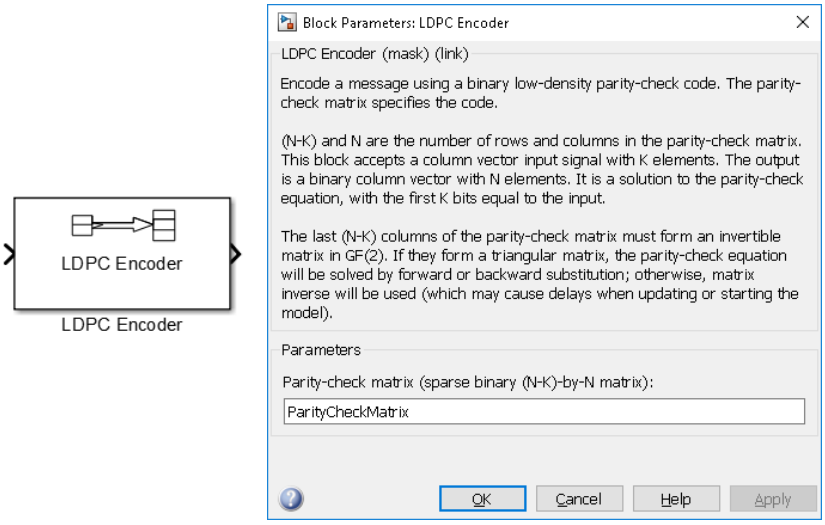

Figure 4.9: LDPC encoder Simulink block.

4.4 Digital modulation

The main goal of the considered framework is to demonstrate the reliability of miltigigabit data rate transmissions at mmWave frequencies. therefore, modulations with high spectral efficiency are preferable, such as QAM, since the throughput is increased by a factor of $log_2(M)$, where M denotes the QAM modulation order. In addition to the modulation order, the constellation mapping of the QAM symbols is also configurable. Figure 4.10 shows the diagram of the digital modulation process. $NormalizationFactor$ depends on the modulation order and its purpose is to achieve a unit average power regardless the M-ary modulation.

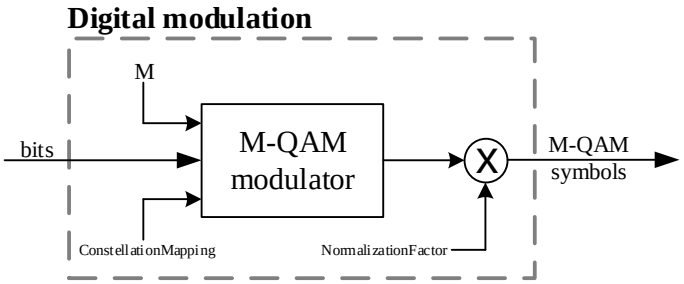

Figure 4.10: Digital modulation block diagram.

The employed QAM modulator is the Rectangular QAM Modulator Baseband block. This block maps the received source bits into M-QAM symbols according to $ConstellationMapping$ value, where it sets the position of each $log_2(M)$ bits in the constellation. The Rectangular QAM Modulator and its configuration for the presented framework is shown in Figure 4.11.

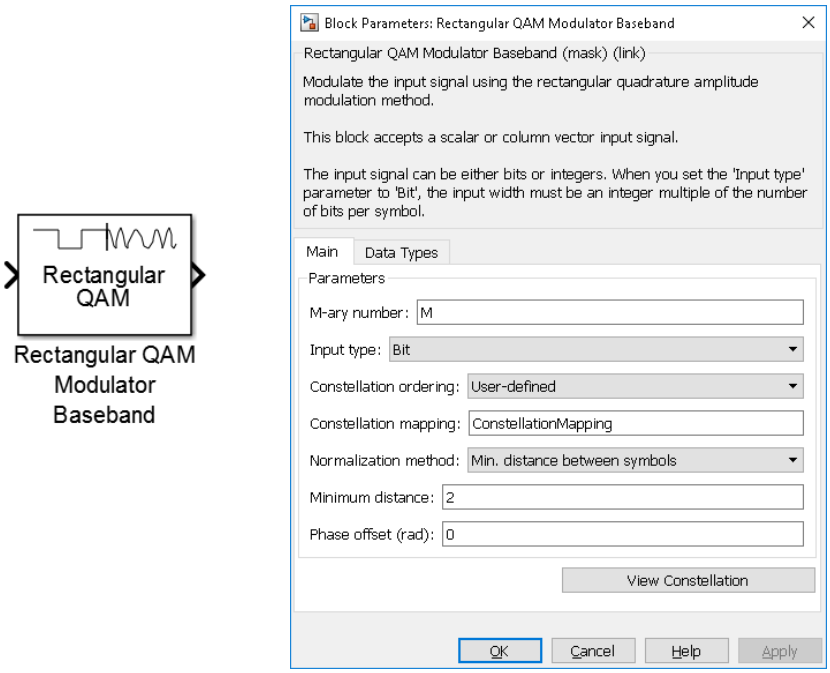

Figure 4.11: Rectangular QAM Modulator.

4.5 OFDM modulator

The OFDM modulator block consists in three main sub blocks: subcarriers allocation block, IFFT and cyclic prefix insertion block. The first one is responsible for shape the spectrum of the transmitted OFDM symbol according to the IFFT positions, illustrated

in the example of Figure 2.8. The subcarriers allocation block aims to assign pilots, virtual subcarriers, such as guard or null, and data subcarriers in the correspondent indexes (up to N_{FFT}), according to pre-defined requirements. It is also responsible for the serial to parallel (S/P) conversion.

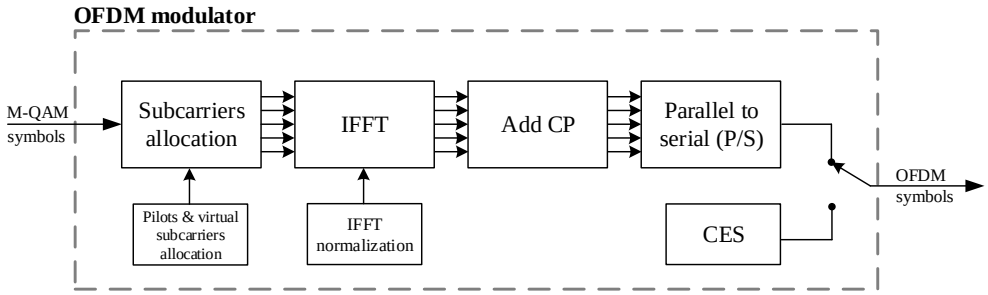

Figure 4.12: OFDM modulator block diagram.

After defining the OFDM symbol shape, it passes through IFFT block provided by Simulink. Since the mathematical expression of IFFT and FFT can affect the amplitude of the signals, it is necessary to normalize the output of these blocks.

Based on the presented in Section 3.1.2, the output of the IFFT block is given by (4.3).

$$y(n) = \frac{1}{N_{FFT}} \sum_{k=0}^{N_{FFT}-1} X_k e^{j2\pi kn/N} \tag{4.3}$$

The average power of the signal $y(n)$ is given by:

$$P_{average} = \frac{1}{N_{total}} \sum_{n=0}^{N-1} |y(n)|^2 \tag{4.4}$$

$$P_{average} = \frac{1}{N_{total}} \sum_{n=0}^{N_{total}} \sum_{n=0}^{N_{used}} (\frac{1}{N_{FFT}^2}) X_k^2 \tag{4.5}$$

Since the average power from the output of the digital modulation is one,

$$P_{average} = \frac{1}{N_{total}} \sum_{n=0}^{N_{total}} \sum_{n=0}^{N_{used}} (\frac{1}{N_{FFT}^2}) \tag{4.6}$$

Considering $N_{total} = N_{CP} + N_{FFT}$,

$$\Leftrightarrow P_{average} = \frac{1}{N_{CP} + N_{FFT}} \times \frac{1}{N_{FFT}^2} \sum_{n=0}^{N_{CP}+N_{FFT}} \sum_{n=0}^{N_{used}} 1 \tag{4.7}$$

$$\Leftrightarrow P_{average} = \frac{1}{N_{CP} + N_{FFT}} \times (N_{CP} + N_{FFT}) \times N_{used} \tag{4.8}$$

$$\Leftrightarrow P_{average} = \frac{N_{used}}{N_{FFT}^2} \tag{4.9}$$

Analyzing expression (4.9), it is seen that to normalize the IFFT signal it is just necessary to multiply the signal by $\sqrt{P_{average}{}^{-1}}$.

The cyclic prefix (CP) is inserted in the OFDM signal after the FFT normalization operations. As stated in Section 3.1.2, the last N_{CP} samples of the OFDM signal with length N_{FFT} are copied to the beginning of the signal. The implementation of this operation is presented in Figure 4.13. Figure 4.14 shows the typical shape of the OFDM frequency spectrum after CP is inserted.

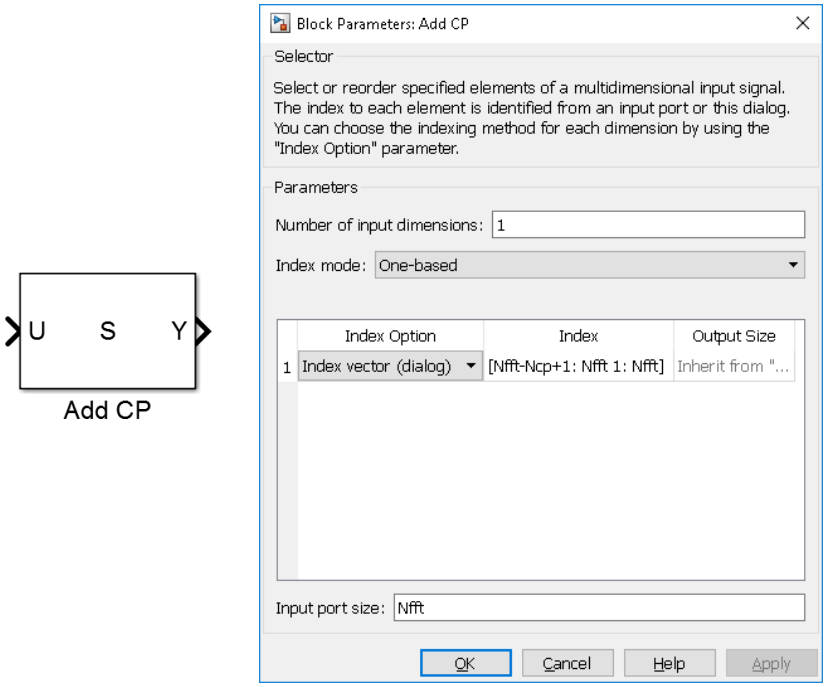

Figure 4.13: Cyclic prefix implementation.

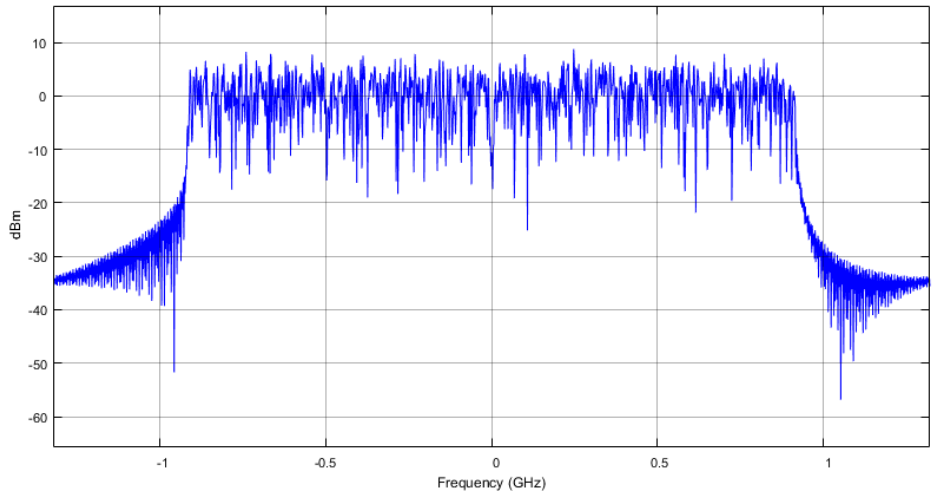

Figure 4.14: OFDM frequency spectrum in the transmitter side.

4.6 Channel

The OFDM symbols are transmitted over a quasi-static multipath fading channel which is obtained by the convolution between data ($x[n]$) and the channel impulse response of the considered channel ($h[n]$). To the result of the convolution it is added additive white Gaussian noise ($w[n]$) in order to vary the SNR of the transmission at the receiver side, as shown in Figure 4.15.

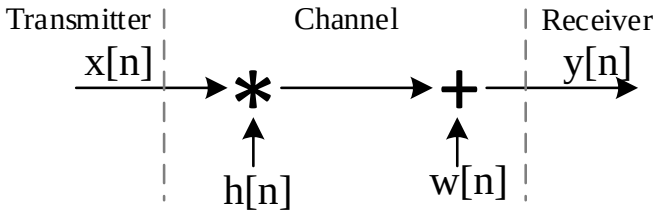

Figure 4.15: Multipath fading channel operations.

In Simulink, the block that models the AWGN has multiple inputs, such as: the ratio of the bit energy to noise power spectral density (E_b/N_0), the number of bits per symbol ($Bits/symbol$), the input signal power and the number of samples per symbol ($Samples/symbol$). $Bits/symbol$ describes the number of bits in one OFDM symbol and it is given by

$$Bits/symbol = log_2(M) \times N_{used} \tag{4.10}$$

$Samples/symbol$ can be interpreted as the length of the OFDM symbol, which

means that it is equal to $N_{FFT} + N_{CP}$.

The input signal power is calculated using the Average Power block (Figure 4.16) according to Eq.4.4.

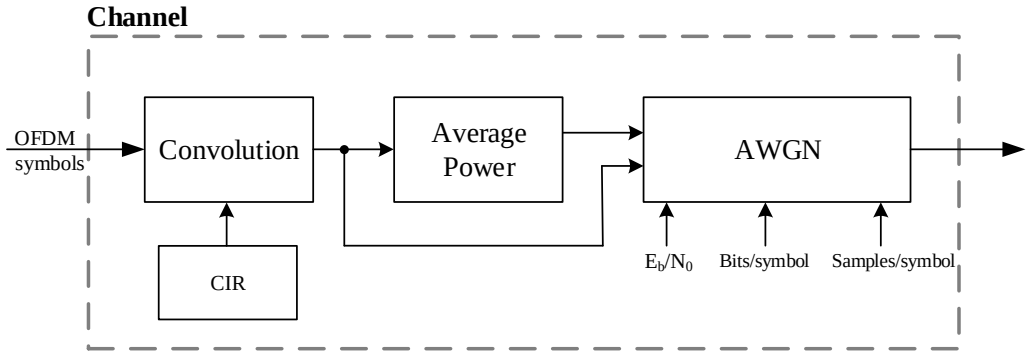

Figure 4.16: Multipath channel block diagram.

4.7 OFDM demodulator

The first stage of the OFDM demodulator consists in the removal of the cyclic prefix. Then, depending on the considered channel estimation technique, the FFT operation is performed before or after channel estimation block, as referred in Section 3.1.2. If a CES-based channel estimation is considered, such as the one presented in Section 3.4.2, and when the CES is transmitted, the FFT is applied after the channel estimation block. Otherwise FFT is performed before any other operations are applied to the received symbols. The overall OFDM demodulator block diagram of the porposed framework is presented in Figure 4.17. Note that in the receiver side the FFT operations are also affected by a normalization factor, as described in Section 4.5.

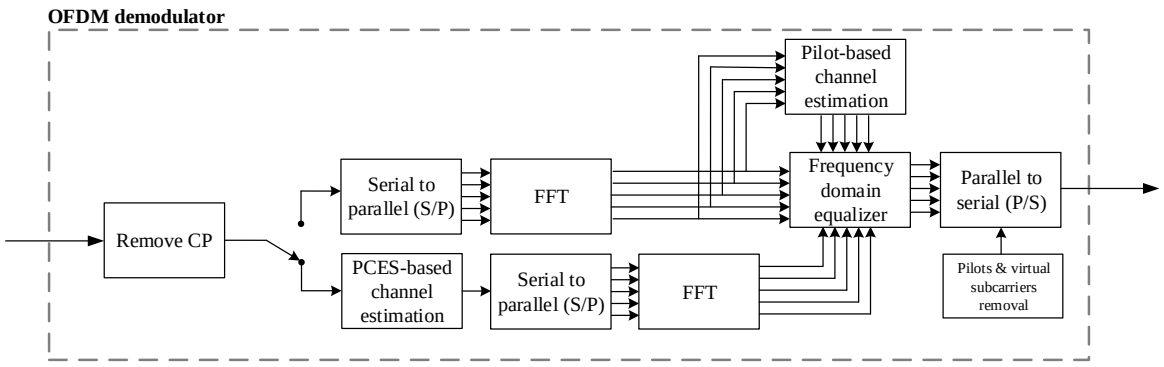

Figure 4.17: OFDM demodulator block diagram.

4.7.1 Channel estimation

The proposed multigigabit simulation framework provides two channel estimation approaches: estimation using pilot subcarriers and using channel estimation sequences. The pilot-based pilot estimation block implements Least-Square estimation technique. The channel estimation based on CES is implemented using Golay sequences, specifically the Golay correlator method presented in Section 3.4.2.

4.7.1.1 Pilot-based channel estimation

The pilot-based channel estimator block is composed by Least-Square (LS) estimation block and the linear interpolation block (Figure 4.18), as presented in Section 3.4.1. Least-Square estimation block is responsible for compensate the effects of the wireless channel comparing the known transmitted pilot subcarriers amplitudes and the received pilots amplitudes distorted by the multipath fading channel. The interpolation block performs a linear interpolation between the already estimated pilot tones in order to build a complete estimated channel frequency response.

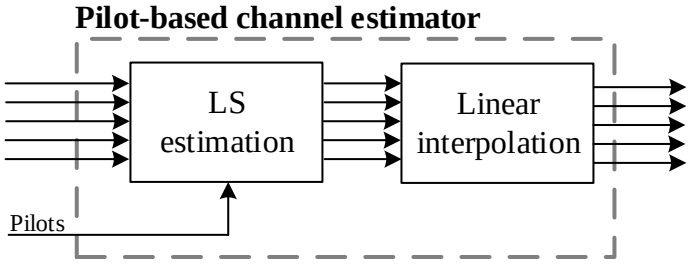

Figure 4.18: Pilot-based channel estimator block diagram.

4.7.1.2 Channel estimation sequence-based channel estimation

As presented in Section 3.4.2, Golay series as preamble channel estimation sequences are very effective for channel estimation purposes. In the proposed framework, Golay sequences of length 256 are implemented as suggested in [60] and [65]. The combination of the pair of sequences that are transmitted is configurable in order to be more suitable for a determined environment. The implementation of Golay channel estimator block in the receiver is presented in Figure 4.19 where can be seen that the auto-correlation is performed for the in-phase (I) component and in-quadrature (Q) component.

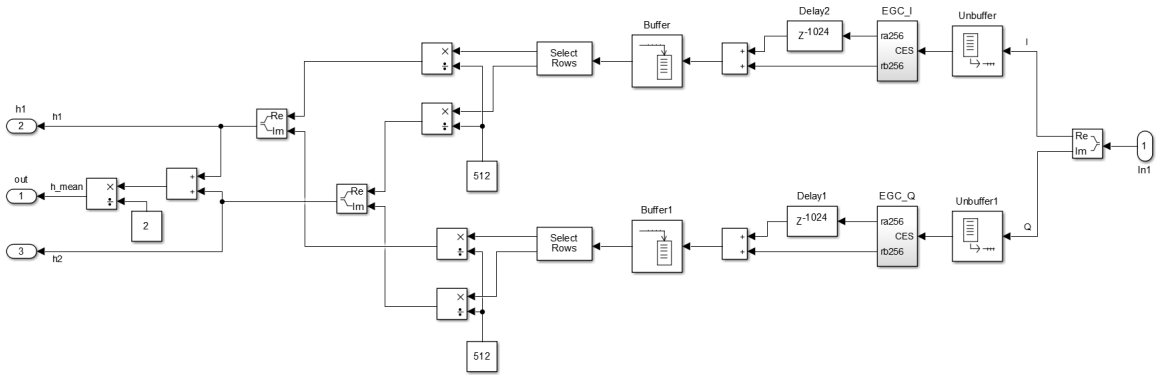

Figure 4.19: Implementation of Golay-based channel estimator.

In Figure 4.20, is shown the implementation of the Golay correlator for sequences of length $N = 256$. Note that, as presented in Section 3.4.2 the correlator is composed by $log_2(N)$ delay stages.

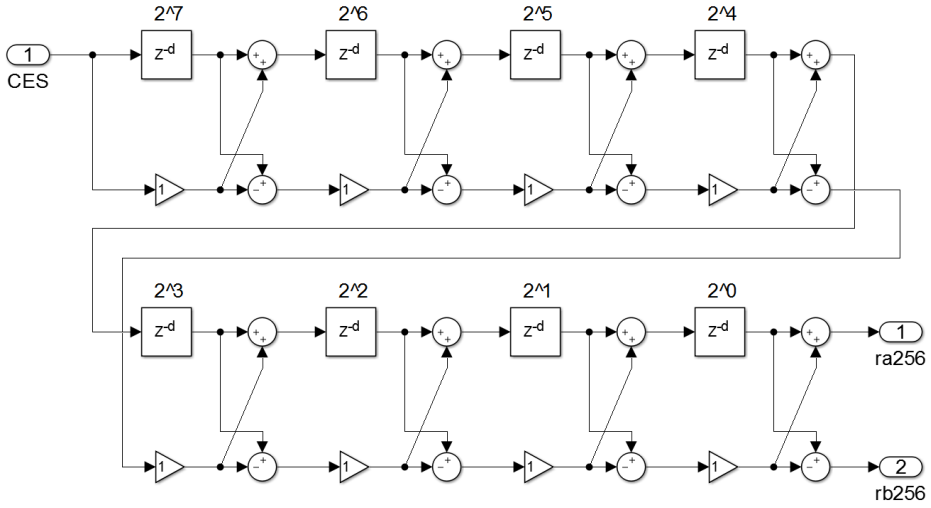

Figure 4.20: Implementation of Golay correlator.

Performing sum of the auto-correlation of transmitted each pair in the receiver, two estimated channel impulse responses, $\hat{h}_1(t)$ and $\hat{h}_2(t)$ are obtained. After an FFT operation on both CIRs, the average CFR is estimated according to:

$$\hat{H}(k) = \frac{1}{M} \sum_{m=1}^{M} \hat{H}(m,k) \tag{4.11}$$

, where $\hat{H}(k)$ is the CFR estimated by averaging the M estimates of CFR at the k^{th} subcarrier, M is the number of Golay pair repetitions in the transmitted CES sequence and m is the index of each pair. In order to estimate the SNR ($\hat{\eta}$), the procedures presented in Section 3.4.3 are employed and shown below.

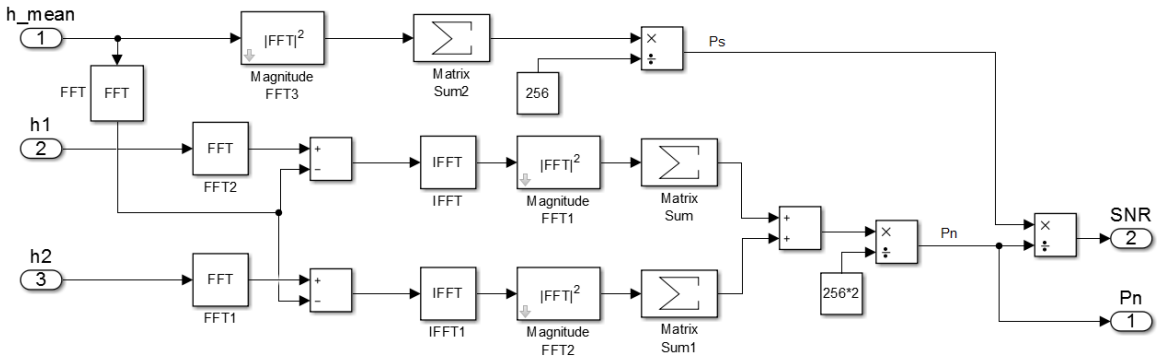

Figure 4.21: Implementation of SNR estimation block.

Additionally, it is proposed an improvement on the Golay estimator to improve its the accuracy on low SNR regimes when MMSE equalization is employed. This is, by comparing the average power estimated on each individual CIR path, $|\hat{h}(k)|^2$, with a certain threshold, λ, only the significant CIR paths are selected as inputs to the K - point FFT. The value of λ is determined by (3.53). Therefore, whose average power estimation are below the threshold are assumed that they contain only noise samples, and thus set to null. The mathematical representation is presented in (4.12).

$$\hat{H}(k) = \begin{cases} \hat{H}(k), & |\hat{H}(k)|^2 > \lambda \\ 0, & otherwise \end{cases} \tag{4.12}$$

4.8 Frequency domain equalizer (FDE)

In the proposed framework both Zero Forcing (ZF) and Minimum Mean Square Error (MMSE) frequency domain equalizers were implemented according to Eq. 3.50 and Eq. 3.51, as shown in Figure 4.22. The estimated SNR used in MMSE-FDE is obtained as shown in Figure 4.21.

The computational effort in the OFDM receiver is something to take into account. Thus, it is important to understand the the relation between performance and computational complexity of the implemented equalization approaches.

According to [61], ZF equalizer can be simplified in order to become

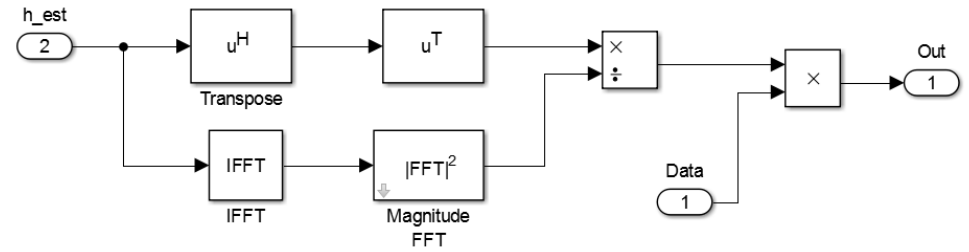

(a)

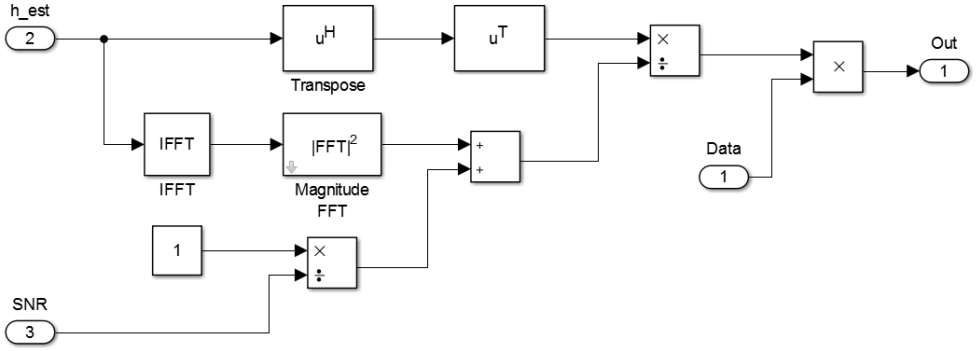

(b)

Figure 4.22: Simulink implementation of a) ZF-FDE and b) MMSE-FDE

$$C_{ZF}(k) = \frac{1}{\hat{H}(k)} \tag{4.13}$$

which in terms of computational demanding it is much lower when compared with MMSE-FDE.

4.9 Digital demodulation and data recovery

This block is responsible for receiving the M-QAM symbols and recover the correspondent transmitted bits. After QAM demodulation process, FEC decoding techniques are employed, considering that C-OFDM transmission has been selected. Figure 4.23 shows the block diagram of QAM demodulation and data decoding.

Note that, as happened in digital modulation the M-QAM symbols are affected by *NormalizationFactor* constant. Despite the QAM demodulator configurations for both uncoded transmission or concatenated coding is similar to the QAM modulator presented in Section 4.4, the QAM demodulator for coded LDPC transmission has different configurations. These differences are due to the use of maximum-likelihood

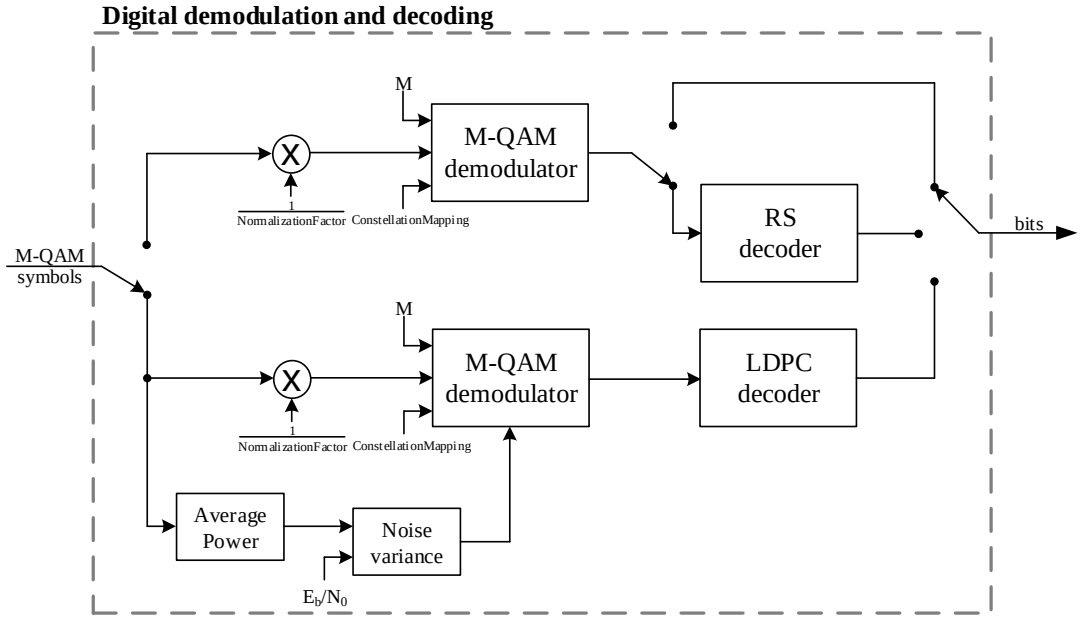

Figure 4.23: Digital demodulation block diagram.

decoding techniques for LDPC codes (refer to Section 3.3.2). As can be seen in Figure 4.24, the decision type configuration of the Simulink block is Approximate log-likehood ratio, which makes necessary to know the noise variance that characterizes the multi-path fading channel. The noise variance of the channel can be determined with E_b/N_0 value. For that, E_b/N_0 must be converted into SNR. Thus, noise variance (σ^2) can be given by:

$$\sigma^2 = \frac{P_{average}}{10^{\frac{SNR}{10}}} \tag{4.14}$$

, where $P_{average}$ is obtained as presented in section 4.4.

Figure 4.25 shows an example of a QAM constellation which symols were tranmitted through a channel charaterixed by a Rayleigh distribution and affected by AWGN for both 16 QAM and 64 QAM.

Note that for both FEC techniques, the decoding process was implemented following the same principle as in the coding stage, which means that the same type of Simulink blocks and parameters were considered. As shown in Figure 4.26, Viterbi decoder block is implemented for inner decoding purposes.

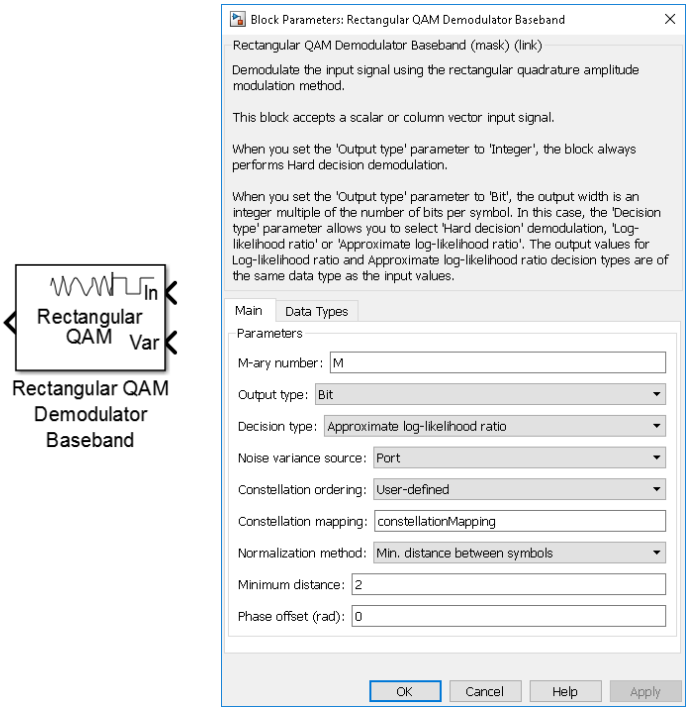

Figure 4.24: Rectangular QAM demodulator.

4.10 Performance evaluation metrics

In order to characterize and evaluate properly the overall performance of the multi-gigabit framework, several metrics should be evaluated. Thus, in this section bit error rate, channel frequency response (CFR), peak signal-to-noise ratio (PSNR), throughput and spectral efficiency are presented as key performance indicators (KPIs) of the proposed framework.

4.10.1 Bit Error Rate (BER)

To evaluate the feasibility of a wireless communications system, BER performance is essential. In the presented framework, BER is assessed using the Error Rate Calculation block from Simulink. This block has two inputs: the binary data transmitted and the binary data recovered in the receiver, as shown in Figure 4.27.

A typical Bit Error Rate evaluation consists in varying the E_b/N_0 at the receiver to evaluate how many errors are obtained. Each BER simulation has as many iterations as the length of the vector that contains E_b/N_0 values. Note that one iteration finishes when $maxNumBits$ are transmitted or when $maxNumErrs$ are detected (see Figure

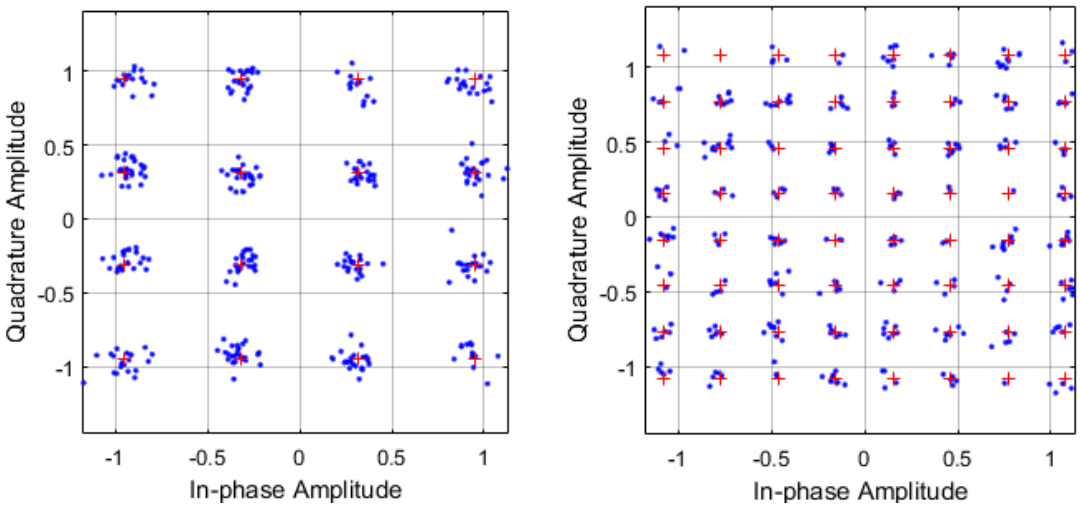

(a) (b)

Figure 4.25: Received QAM constellation for a) 16 QAM and b) 64 QAM.

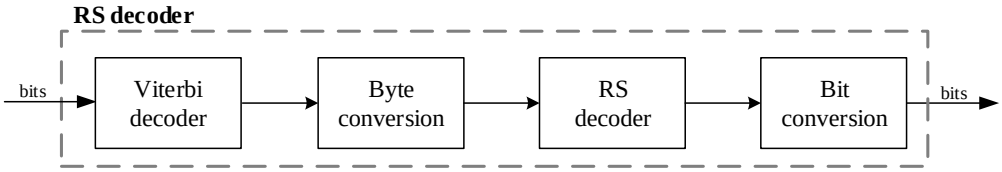

Figure 4.26: Reed-Solomon Decoder block diagram.

4.27). In the proposed framework it was defined a maximum transmitted bits per iteration ($maxNumBits$) of 10^8 bits and a maximum number of error bits per iteration of 200 bits.

In order to validate the proposed framework and the BER assessment method, several simulation were conducted considering both 16 and 64 QAM modulation scheme over AWGN channel. The framework validation is performed through the comparison between the simulated results and analytic expression of error probability over AWGN given by [43]:

$$P_e = \frac{2(M-1)}{M \times log_2(M)} Q[\sqrt{\frac{6 \times E_b}{N_0} \times \frac{log_2(M)}{M^{2-1}}}] \tag{4.15}$$

, where $Q(.)$ is defined as

$$Q(x) = \frac{1}{\sqrt{2\pi}} \int_x^{\infty} e^{-t^2/2} dt \tag{4.16}$$

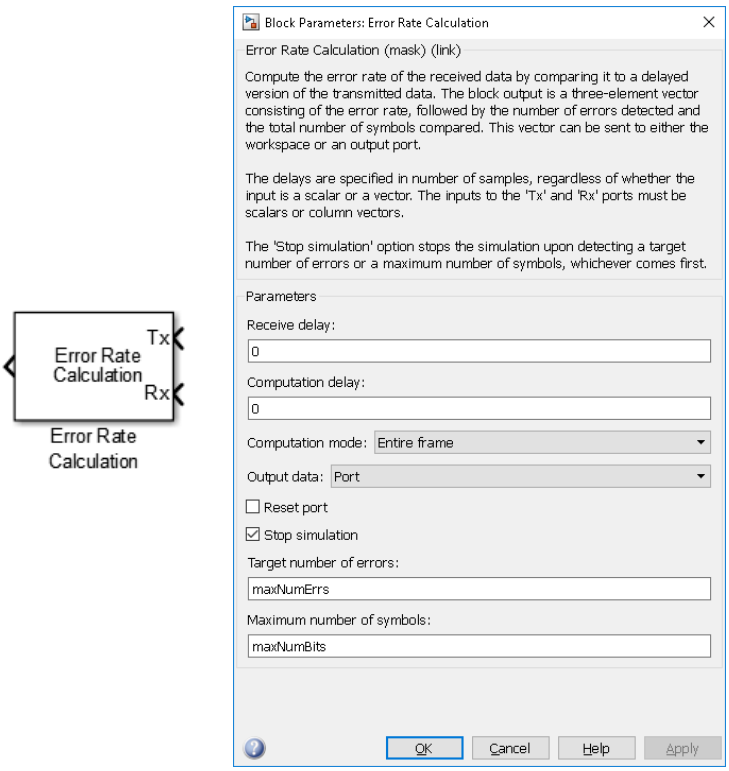

Figure 4.27: Error rate calculator.

Figure 4.29 shows the comparison BER results for both modulation schemes.

4.10.2 Channel Frequency Response (CFR)

The frequency response is used to characterize how frequency selective a channel is. It is computed by applying a FFT operation to the channel impulse response of that channel. Therefore,

$$H(k) = FFT\{h(n)\} = \frac{1}{N}\sum_{n=0}^{N-1} h(n)e^{-j2\pi n/N} \tag{4.17}$$

,where $K = 0, 1, ..., N-1$ and N denotes the length of the FFT.

CFR can be also very important to evaluate the performance of a channel estimation method, since it is possible to compare the real CFR with the estimated one.

A typical CFR representation for the proposed framework is shown in Figure 4.28. Note that de magnitude of the channel coefficients are given by Eq. 4.18.

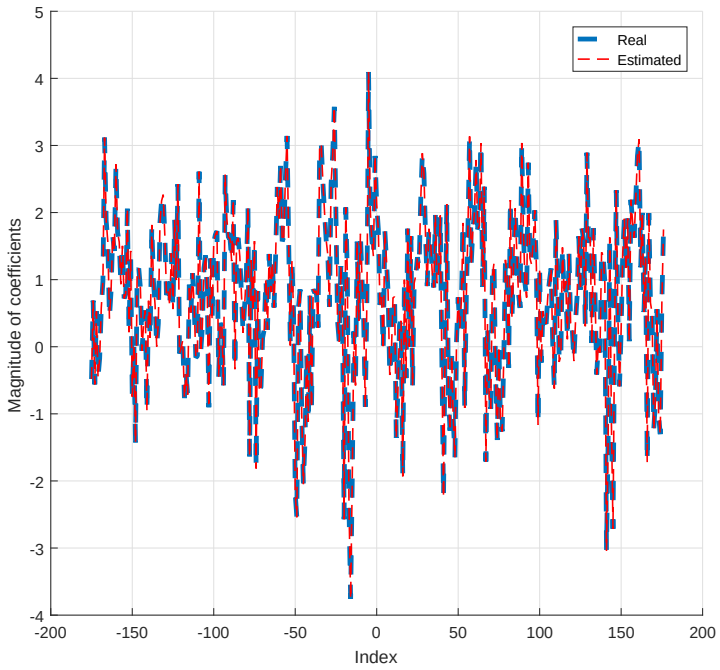

Figure 4.28: Real CFR vs. estimated CFR.

$$H_{dB}(k) = 10log_{10}(|H(k).\bar{H(k)}|) \tag{4.18}$$

In order to compare the estimated channel frequency response with the real CFR, the mean-square error (MSE) is computed according to:

$$MSE_{dB} = 10log_{10}(\frac{1}{N}\sum_{i=0}^{N-1}(f_i - y_i)^2) \tag{4.19}$$

,where N is the number of samples, and f_i is the estimation sample of y_i.

4.10.3 Peak Singal-to-Noise Ratio (PSNR)

The Peak Signal-to-Noise Ration (PSNR) is an expression for the ratio between the maximum possible value of a signal and the power distortion noise that affects the quality of its representation [66]. Knowing that the visual quality of a digital image is subjective (it can vary from person to person), PSNR is commonly used to evaluate objectively quality of a video frame, for example.

The mathematical expression for PSNR is as follows:

$$PSNR = 10log_{10}(\frac{{MAX_f}^2}{MSE}) \tag{4.20}$$

,where MSE in this case is given by

$$MSE = \frac{1}{mn}\sum_{i=0}^{m-1}\sum_{j=0}^{n-1}(f(i,j) - y(i,j))^2 \tag{4.21}$$

, m represents the number of rows of pixels of the image and i is the index of that row, while n represents the number of columns of pixels of the image and j is the index of that column. f and y represents the matrix data of the original and degraded image, respectively. Note that ${MAX_f}^2$ describes the maximum signal value known in the image.

4.10.4 Throughput and Spectral Efficiency

The spectral efficiency of a communication system can be seen as the ratio between throughput and bandwidth of the transmitted signal. In a real system this ratio tends to be lower than one since it is necessary to introduce overhead in order to improve the system performance.

The bandwidth of a OFDM symbol (W) is given by the product between the subcarrier spacing (Δf) and the number of subcarriers in the system (N_{FFT}: length of the IFFT block):

$$W = \Delta f \times N_{FFT}[Hz] \tag{4.22}$$

In order to ensure orthogonality among subcarriers $\Delta f = \frac{1}{T_S}$, therefore Eq. 4.22 can be rewritten as:

$$W = \frac{1}{T_S} \times N_{FFT}[Hz] \tag{4.23}$$

In a real system not all the subcarriers are used to allocate information, thus the bandwidth can be written as:

$$W = \frac{1}{T_S} \times N_{used}[Hz] \tag{4.24}$$

, where N_{used} represents the number of subcarriers that carry information.

The throughput can be achieved by applying the following equation:

$$Throughput = \frac{N_{used} \times b}{T_S + T_{CP}} \times FEC_{rate}[bits/s] \tag{4.25}$$

, where b is the number of bit per symbol and FEC_{rate} represents the Forward Error Correction (FEC) rate.

Finally , the spectral efficiency is given by

$$\beta = \frac{Throughput}{W} = \frac{b \times FEC_{rate} \times T_S}{(T_S + T_{CP})}[bits/s/Hz] \tag{4.26}$$

4.11 Framework validation

This section presents several simulation results that aim to validate the proposed framework. The main goal is to show that the framework is working as expected and it can be verified by comparing some simulation results with the theoretical ones.

4.11.1 BER performance

In this section, the comparison between the BER simulation results and the analytic expressions reported in Section 4.10.1 is presented. As it can be seen, the simulation results fairly fits whit the theoretical ones. Analyzing Figure 4.29 can be concluded that, for uncoded transmission and over an AWGN channel, it is necessary to ensure a E_b/N_0 of 14 dB for 16 QAM modulation to obtain a error probability of 1 bit per 1 million bits transmitted. As expected, considering 64 QAM modulation scheme, it is required to guarantee a better singal-to-noise ratio (E_b/N_0 of about 18 dB) to obtain similar BER results.

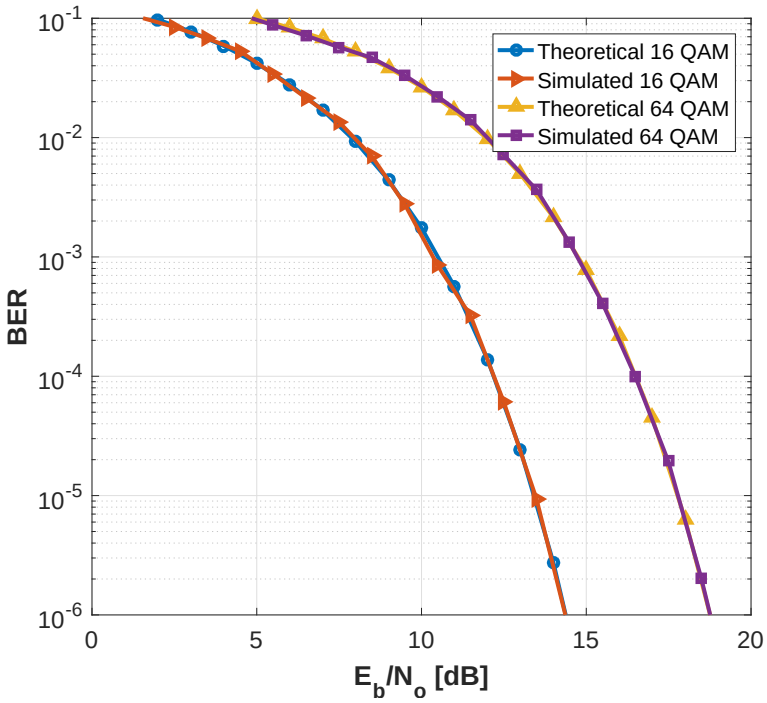

Figure 4.29: Comparison of the theoretical and simulated E_b/N_o results for uncoded OFDM, using 16 and 64 QAM modulations, over an AWGN channel.

4.11.2 Channel estimation

4.11.2.1 Pilot-based channel estimation

The validation of the channel estimator based on pilot subcarriers was performed under a typical Rayleigh channel [43]. Figure 4.30 compares the output of the LS estimation block with the CFR of the considered Rayleigh channel. Note that for simulation purposes it was implemented a OFDM transmission with IFFT length of 512. For CFR analysis, a bandwidth composed for 352 subcarriers are considered and the pilot subcarriers are uniformly distributed along with those available subcarriers. Figure 4.30 a) shows the estimation results for 10 pilot subcarriers while in Figure 4.30 b) 50 pilot subcarriers were considered.

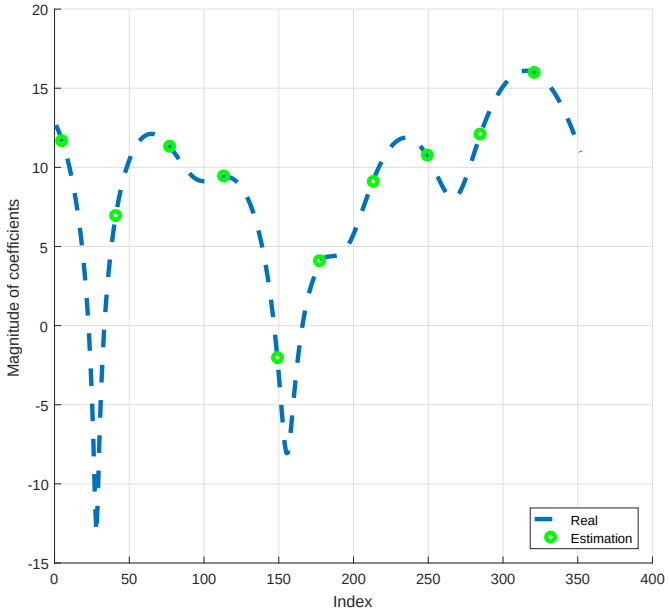

(a)

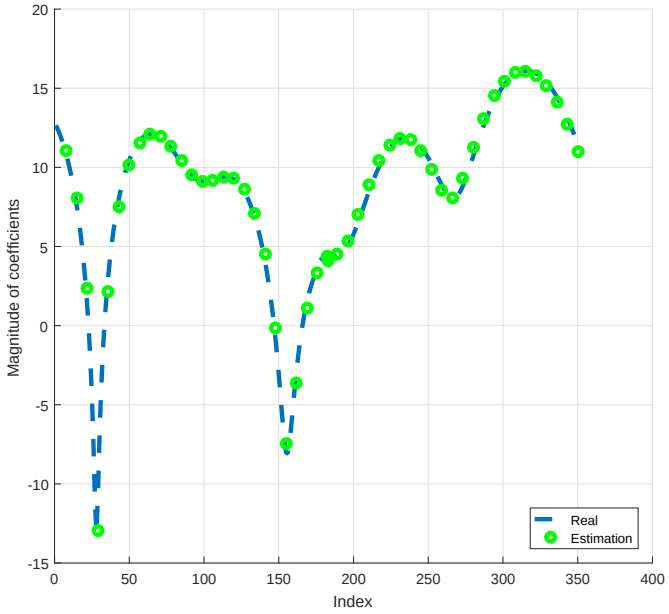

(b)

Figure 4.30: CFR estimation results for a) 10 and b) 50 pilot subcarriers

Then, linear interpolation technique is applied between the estimated pilot tones and the results are depicted in Figure 4.31. It can be seen that the number of pilot subcarriers for channel estimation purposes needs to be attributed according to the channel characteristics. Figure 4.31 (a) shows that, for the Rayleigh channel model considered for this test, 10 pilot subcarriers are not enough to perform a proper channel estimation, since the interpolation function cannot predict the channel variations as

happens with 50 pilot subcarriers (Figure 4.31 (b)).

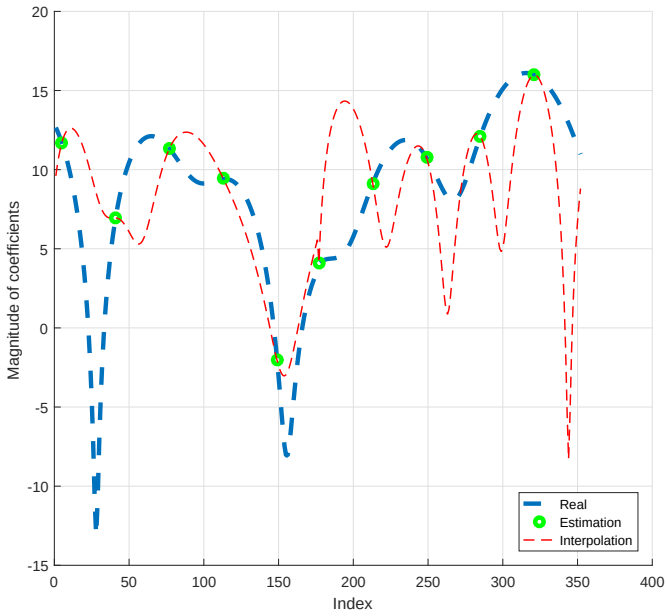

(a)

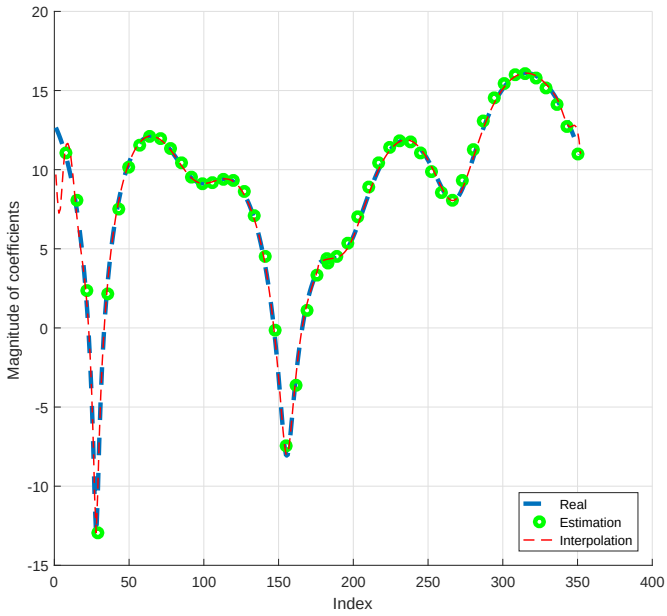

(b)

Figure 4.31: CFR linear intepolation results for a) 10 and b) 50 pilot subcarriers

4.11.2.2 Channel estimation sequences-based channel estimation

In order to evaluate the effectiveness of the channel estimation block based on CES, the Rayleigh channel frequency response presented above was considered. The results of

the estimator validation is present in Figure 4.32, where can be seen that the channel estimation based on Golay sequences are in good agreement with the the theoretical ones.

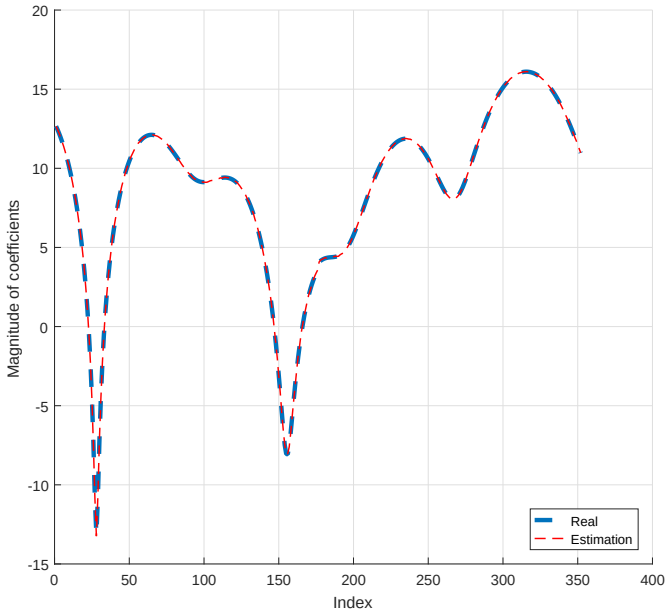

Figure 4.32: Estimated CFR using Golay complementary sequences.

4.11.3 Frequency domain equalizer (FDE)

To evaluate the performance of both equalizers (ZF and MMSE), BER simulations were performed considering an uncoded transmission, ideal estimation, 16 QAM as the modulation scheme and a multipath fading channel which is characterized by Rayleigh distribution as shown in Figure 4.31.

From Figure 4.33 can be concluded that, despite the more complexity implementation and expectable better performance, MMSE-FDE presents similar BER performance compared with ZF-FDE, in terms of BER for highly dispersive channels. Therefore, zero forcing can be seen as the more efficient frequency domain equalizer for the proposed multigigabit framework.

Figure 4.34 shows the eye diagram of the received signal considering 16 QAM modulation, before and after frequency domain equalization, specifically zero forcing. Comparing this two eye diagrams it is clear the effectiveness of the frequency domain equalization stage.

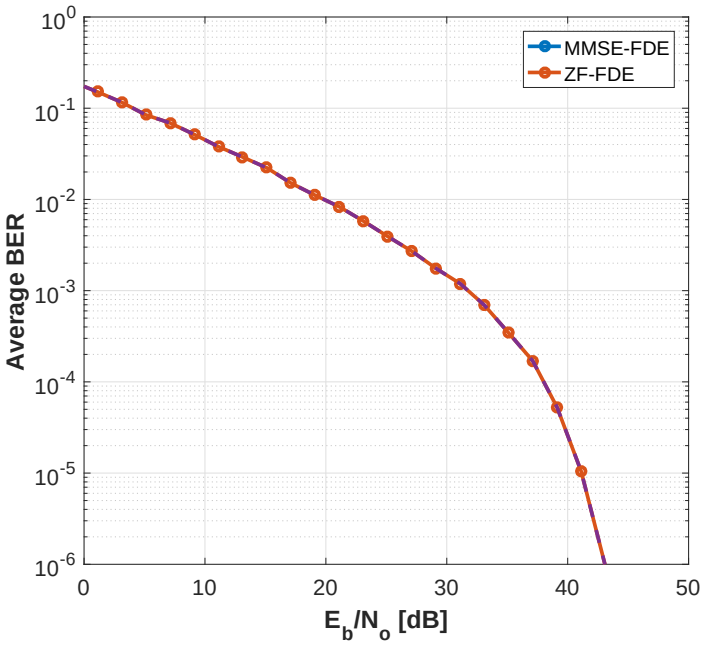

Figure 4.33: BER performance under Rayleigh channel model: ZF equalizer vs. MMSE equalizer.

Table 4.1: Code rates of the considered OFDM FEC schemes.

FEC	Code rate
RS (224,216)	9/14
LDPC (336,672)	1/2
LDPC (504,672)	3/4

4.11.4 Channel coding

In order to validate the implementation of the FEC codes in the proposed framework, several BER simulations were performed. This simulations considers both 16 QAM and 64 QAM modulation scheme and wireless channel which is affected by AWGN. For validation purposes three FEC codes are considered: RS(224,216), LDPC(336,672) and LDPC(504,672) and the corresponding coding rate is presented in Table 4.1.

Shannon limit [67] describes performance boundaries between the maximum possible efficiency of error-correcting methods and the noise level of a wireless transmission. It defines the maximum information transfer rate of a certain channel for a particular noise level and it can be simplified in order to become

$$R = B_W log(1 + \frac{S}{N}) \tag{4.27}$$

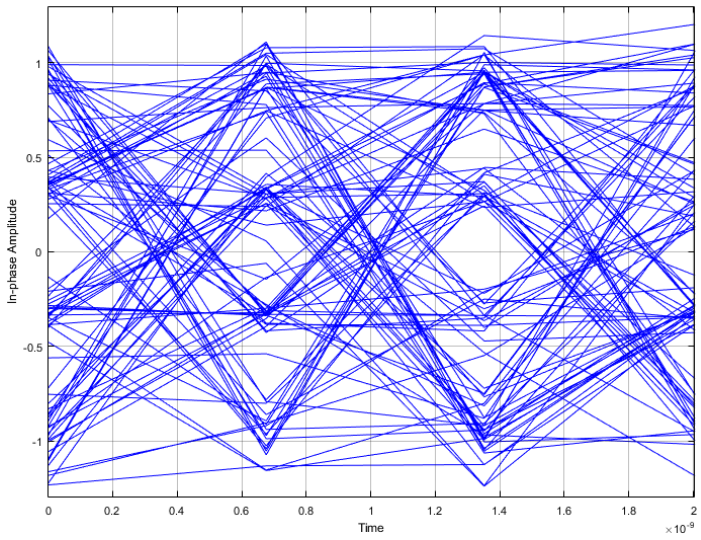

(a)

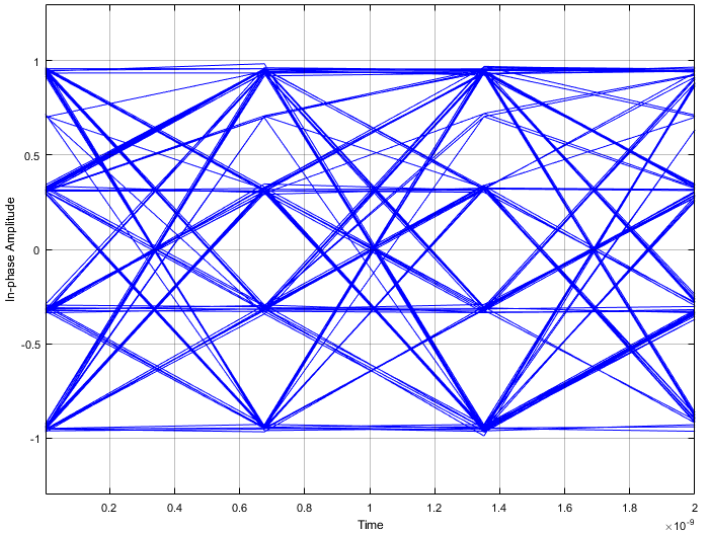

(b)

Figure 4.34: Eye diagram of the received signal (a) before and (b) after FDE process.

,where R denotes the information transfer rate, B_W is the bandwidth of the channel and S/N denotes the signal-to-noise ratio of the communication.

With Shannon limit it is possible to define the minimum SNR of a certain wireless transmission which is characterized by the data rate and FEC code considered. Thus, it is a good metric to evaluate the effectiveness of the implementation of the FEC codes in the proposed simulation framework, since it is expected that LDPC codes are very close to the Shannon coding limit [68], [42].

The BER simulation results for FEC codes validation are depicted in Fig 4.35. From its analysis can be seen that, as expected LDPC outperforms concatenated code

and they are close to Shannon coding Limit.

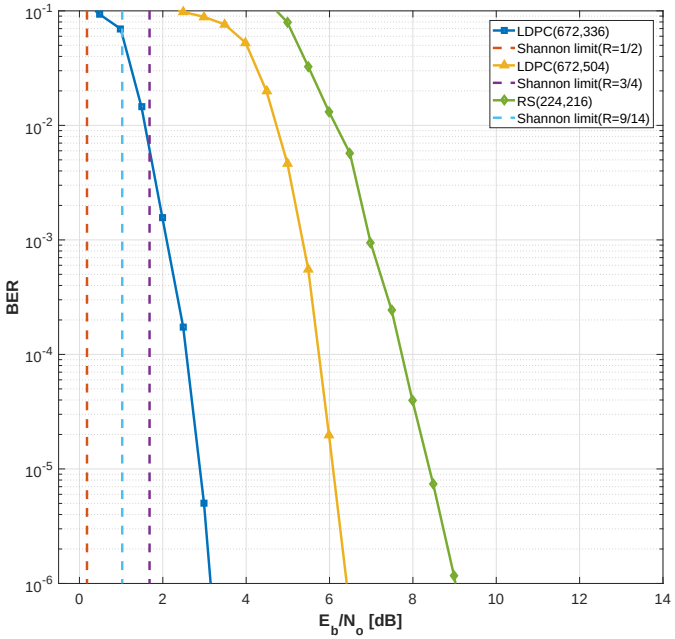

(a)

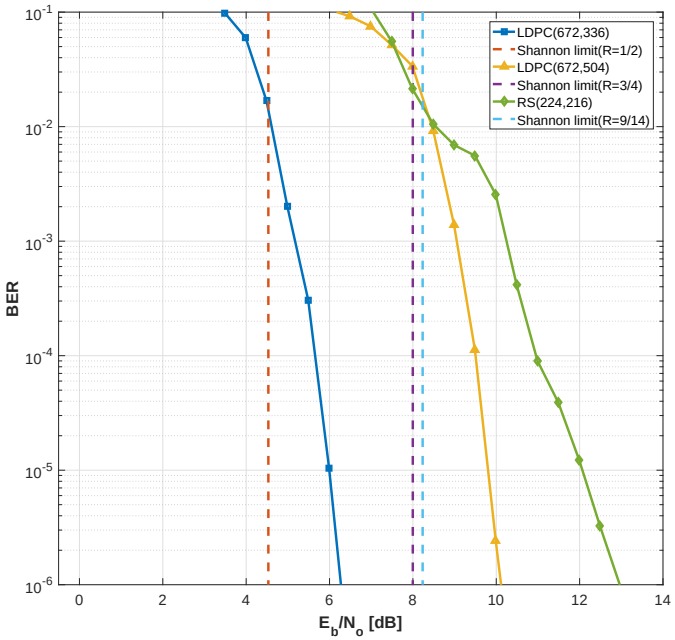

(b)

Figure 4.35: BER performance for coded OFDM: (a) 16 QAM (b) 64QAM.

4.12 Summary

Chapter 4 presented the implementation of the proposed simulation framework. First, the general block diagram of the framework is shown and a quick description of the overall operation is presented. Then, each block of general block diagram is detailed. This Chapter also addresses the performance evaluation metric considered for the work in order to characterize properly the framework performance. Finally, simulation results are conducted in order to validate the simulation tool.

Chapter 5

Performance evaluation of 60 GHz OFDM framework over indoor multipath fading channels

5.1 Introduction

This section aims to present the results of the performance evaluation of the previously presented multi-gigabit simulation framework at 60 GHz towards 5G communications. The objective of this evaluation is to characterize the performance of the simulation environment based on a realistic OFDM transmission at 60 GHz band. For that, the key performance indicator presented in the previous Section are considered.

In order to present a more realistic performance results, the considered multipath fading channels were extracted from real measurements for both LOS and NLOS environments. The need of a quasi-realistic simulation led to consider a stable standard at 60 GHz band, the IEEE 802.15.3c standard which is specified for high rate wireless personal area networks (WPANs) (Section 2.3.2). Thus, in this section several simulation parameters are obtained from the IEEE 50.15.3c standard.

Since the main goal of the proposed framework is to provide a high data rate transmission at 60 GHz, the distance between transmitter and receiver is relatively low. Thus, only indoor scenarios are considered for performance evaluation purposes. Thus, in this section, firstly, the scenarios considered for the performance evaluation are presented and the indoor environments are presented and characterized. Then, the performance results of the uncoded and coded transmission are presented. After

that, a comparative analysis of both channel estimation techniques is shown. Finally, uncompressed video is transmitted over the implemented framework and the results are drawn.

5.2 Study scenarios

The considered indoor scenarios are based on real measurements at 60 GHz band for both LOS and NLOS typologies. In this section the measurement results are shown, as well as the link budget of the considered wireless transmission. It is also taken into account the mobility effect due to the movement of persons in the interior of the building.

5.2.1 Indoor environments

This section presents the channel modeling proposed by TG3c [22] at 60 GHz for the indoor environments: residential, office and kiosk. Each environment can be classified as Line-Of-Sight (LOS) or Non-Line-Of-Sight (NLOS). For LOS, it is considered that there are no objects that block the direct path between the transmitter (T_X) and the receiver (R_X). In an LOS indoor scenario the multipath are mainly from reflected or scattered signals from furniture, the floor and the ceiling. For a NLOS scenario there are no direct path between the transmitter and the receiver antenna.

The residential environment considers, for example, a typical home with multiple rooms and furnished with furniture and TVs sets lounges. The size is comparable to a small office room and the wall is made of concrete or wood. There are also windows and wooden door in different rooms.

Typical office environment contains multiple chairs, desks, computers, and work stations. The walls are made of metal or concrete covered by plasterboard or carpet. This environment type is, typically linked by long corridors.

Kiosk describes a situation where a person is in front of the kiosk serve holding a portable device. Usually, the portable device is pointed to the kiosk server.

For residential environment, both LOS and NLOS scenarios were considered, result-

ing on channel model 1 (CM1) and CM2, respectively. CM3 and CM4 represents the LOS and NLOS link, respectively, for office. For kiosk environment only LOS transmission is considered. Table 5.1 shows the mapping of each indoor channel model to the corresponding environment. The indoor channel models were extracted from measurements and they are characterized by a model parametrization already discussed in Section 3.2.

Table 5.1: Mapping of environment to channel model and scenario [22].

Environment	**Channel Model**	**Scenario**
Residential	CM1	LOS
	CM2	NLOS
Office	CM3	LOS
	CM4	NLOS
Kiosk	CM9	LOS

The TG3c group adopted the generic Complex Impulse Response (CIR) based on the clustering of phenomenon in both time and spatial domains as observed in measurement data [22]. The cluster model is based on the extension of the Saleh-Valenzuela (S-V) model [51] to the angular domain by Spencer [52], as detailed in Section 2.3.2. Hence, the IEEE 802.15.3c channel modelling group [69] proposed a statistical channel model dependent on the temporal and spatial domain, where the signals arrive at the receiver first in a LOS component, calculated with a two-ray model, and then in clusters (modified S-V model).

The residential LOS channel model (CM1) was extracted from the measurement described in [70]. The measurement setup is shown in Figure 5.1. It was considered a range up to 3 m and frequency bandwidth of 3 GHz centered at 62.5 GHz. The measurement results can be found in Table 5.2.

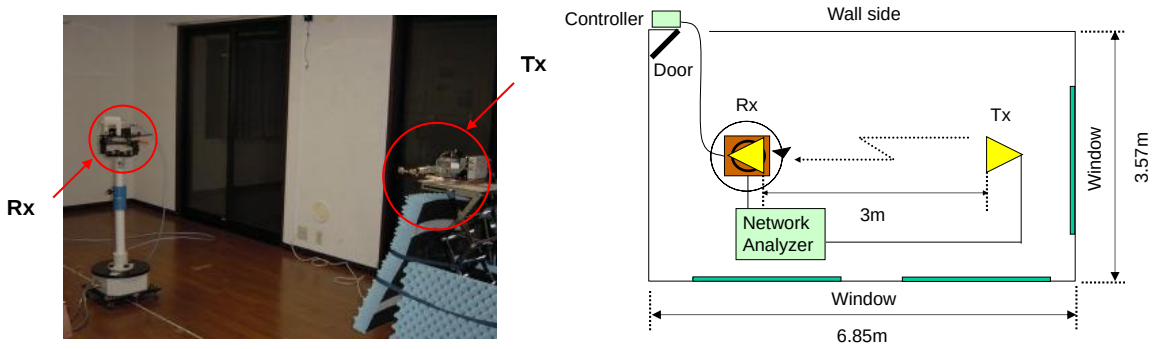

Figure 5.1: Residential LOS channel model measurements setup [70].

The measurement results for CM2 were derived from the LOS channel (CM1). The

generation of NLOS channel is performed by removing the LOS component presence in the statistical LOS channel model derived from the measurements, as reported in [71] and [72].

Channel models for office environment were extracted from two different sets of measurements, for LOS and NLOS transmission. For LOS office, the channel model were extracted on a measurement [73] where it was considered a distance between T_X and R_X of 1-5 m, as shown in Figure 5.2.

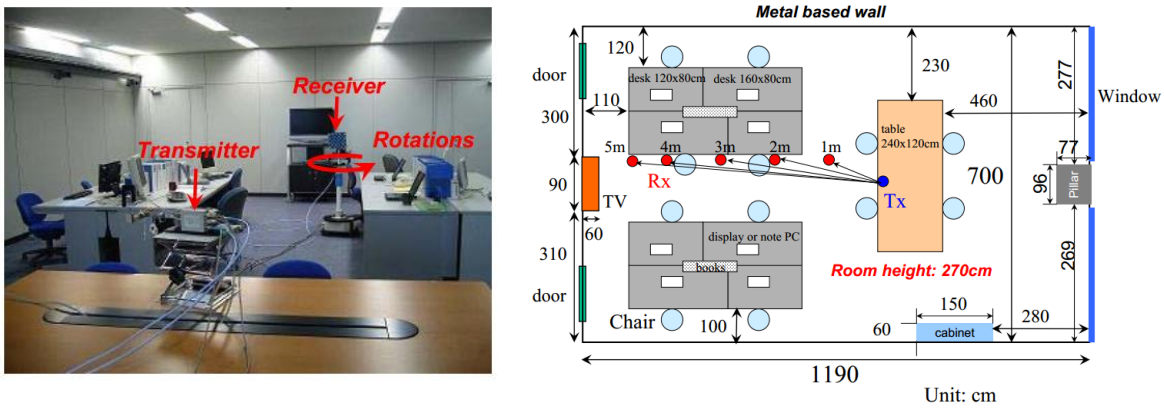

Figure 5.2: Office LOS channel model measurements setup [73].

The NLOS office channel was extracted from measurements that cover a range of 10 m, as can be seen in Figure 5.3. Note that the parameters collected with both measurements are in Table 5.2. As happened with CM1, the modeling of CM3 and CM4 considered a bandwidth of 3 GHz centered at 62.5 GHz.

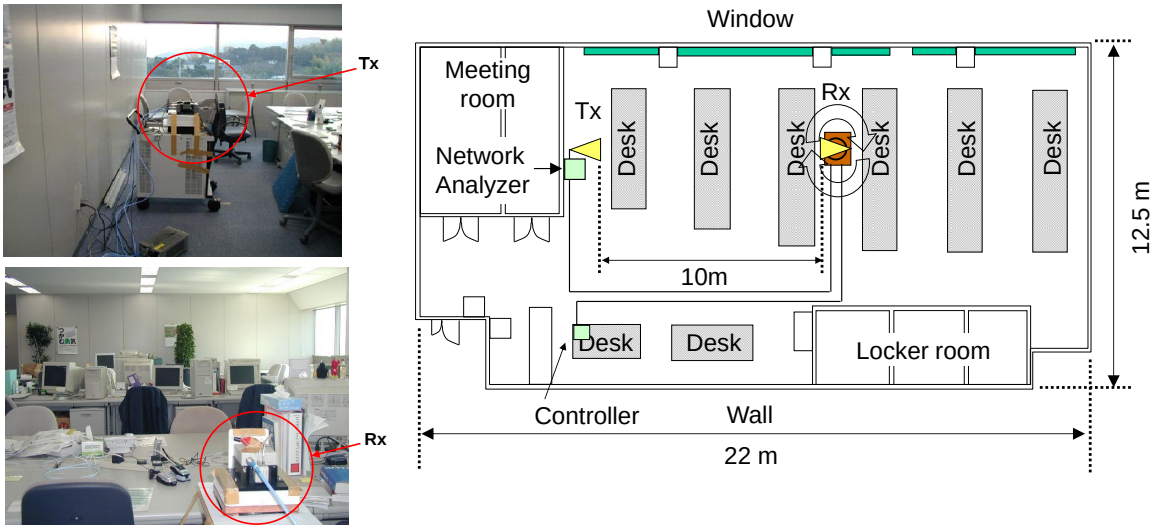

Figure 5.3: Office NLOS channel model measurements setup [74].

The LOS kiosk channel model (CM9) was extracted from measurements that cover

a range of 1 m and frequency bandwidth of 3 GHz centered at 62.5 GHz [22]. The measurement setup is shown in Figure 5.4.

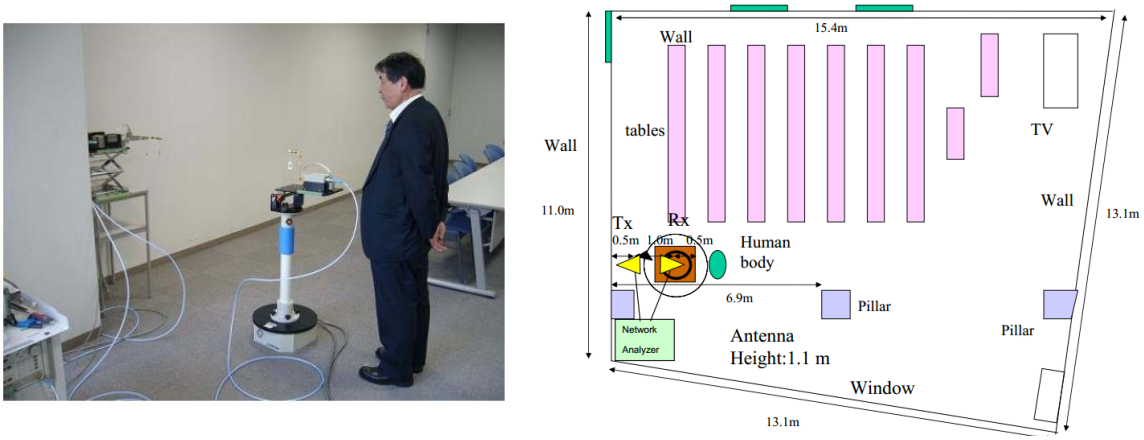

Figure 5.4: Kiosk LOS channel model measurements setup [75].

The Channel Impulse Response of each channel model is generated by a MATLAB tool provided by TG3c group [76] [77].

Table 5.2: Parameters from channel model measurement analysis. [22]

	CM1	**CM2**	**CM3**	**CM4**	**CM9**
Λ (1/ns)	0.191	7.58	0.041	0.028	0.0546
λ (1/ns)	1.22	1.02	0.971	0.76	0.917
Γ (ns)	4.46	6.69	49.8	134	30.2
γ (ns)	6.25	5.62	45.2	59.0	36.5
σ_c (dB)	6.28	4.96	6.60	4.37	2.23
σ_r (dB)	13.0	15.1	11.3	6.66	6.88
σ_ϕ (degree)	49.8	51	102	22.2	34.2
$\overline{L}$	9	9	6	5	5
k (dB)	18.8	22.4	21.9	19.2	11.0
$\Omega(d)$ (dB)	-88.7	-81.9	-89.07	-107.2	-98.0

The Power Delay Profile for each scenario environment is based on the CIR provided in [77] and it is obtained from the average of 100 static channel realizations. I.e, from one realization to another, considering the same channel model, different PDPs are obtained through the variation of the height of the TX and RX antennas, as well as, the scatters position in the multipath environment. Additionally, since this PDP do not take into account neither the Equivalent Isotropically Radiated Power (EIRP), nor the receiver antenna gain, and nor the receiver power sensitivity, two power regimes are considered in this work. Both power regimes are characterized by the EIRP and receiver antenna gain (G_{RX}) for indoor applications. Hence, for indoor applications the

EIRP values considered are 20 dBm and 40 dBm. The G_{RX} considered is 10 dBi for both power regimes, which is the typical value of high gain on-chip antennas at 60 GHz for indoor applications [78]. The dynamic range of each PDP is obtained considering the noise floor as thermal noise, which is defined by:

$$N = k.T.B_{OFDM}\ [W], \tag{5.1}$$

, where N, k, T and B_{SC} are the noise power, Boltzmann constant, temperature in Kelvin and the subcarrier bandwidth of the transmitted OFDM signal, respectively. The system noise floor -81 dBm, considering $T = 290$ K and $B_{OFDM} =$ 1.815 GHz. Additionally, threshold of 10 dB above the noise floor is considered. Figure 5.5 and Figure 5.6 illustrates the used method to obtain the average PDP for the environments cosidered for EIRP of 40 dBm and 20 dBm, respectively.

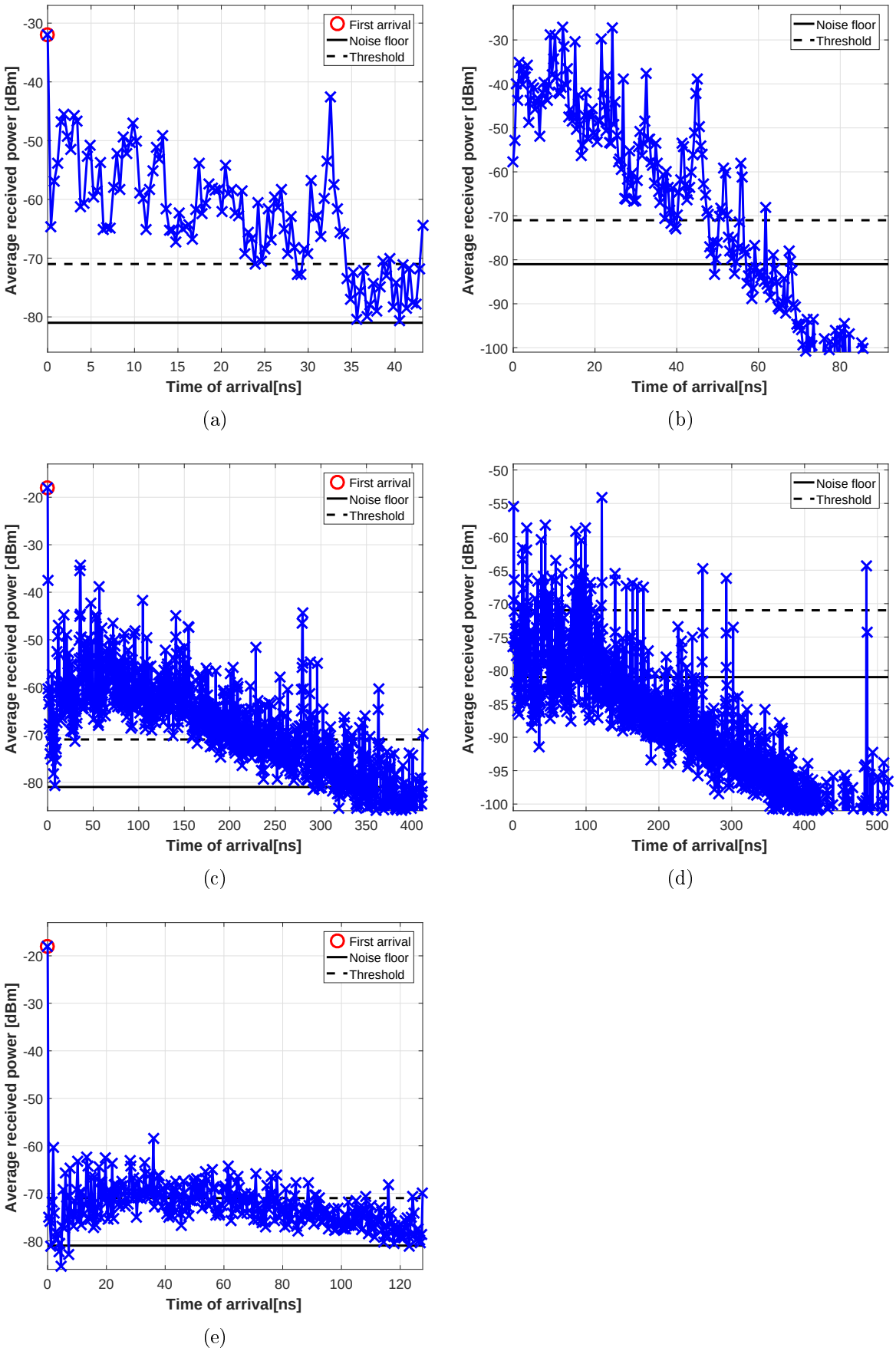

Figure 5.5: PDP for the channel models: a) CM1, b) CM2, c) CM3, d) CM4 and e) CM9 for a EIRP of 40 dBm.

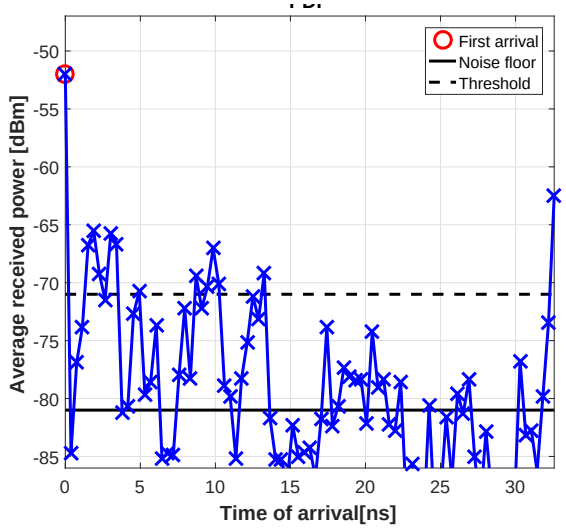

(a)

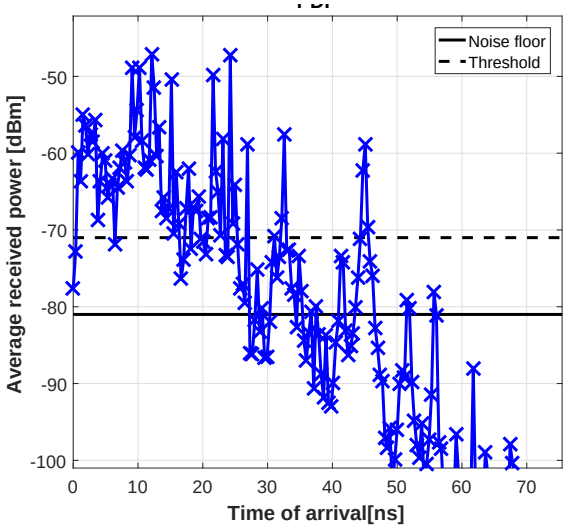

(b)

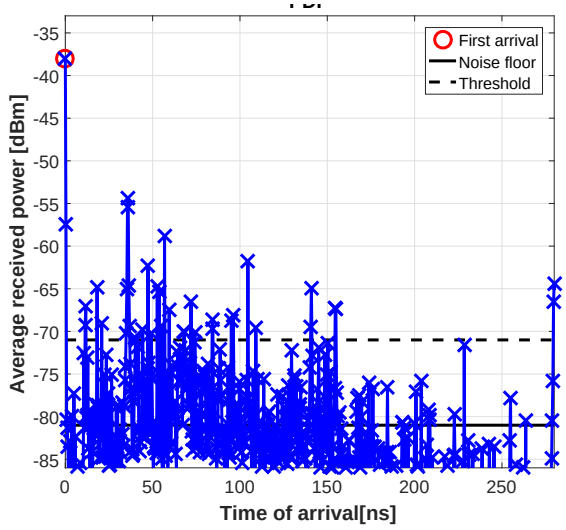

(c)

Figure 5.6: PDP for the channel models: a) CM1, b) CM2 and c) CM3 for a EIRP of 20 dBm.

In order to compare different multipath environments and their performance in a wireless communication system, parameters which quantify the multipath channel are considered. The RMS delay spread (τ_{rms}), maximum delay spread (τ_{max}) and coherence bandwidth B_c are multipath channel parameters that can be determined from a PDP and are explained in Section 3.2.

Figure 5.7 shows the correlation factors in function of the frequency separation for the channel models considered in this work, from which the coherence bandwidth is extracted.

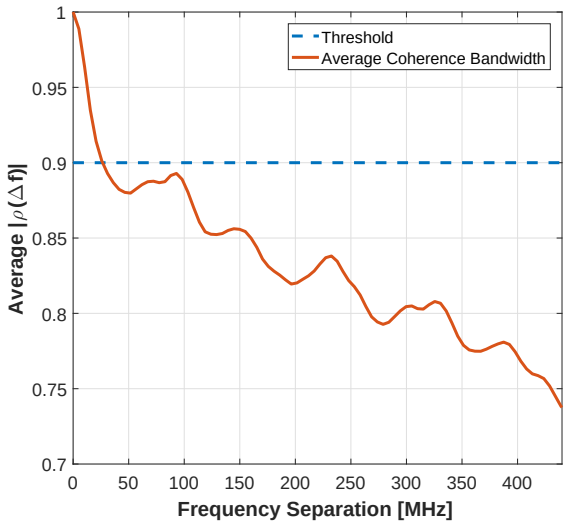

(a)

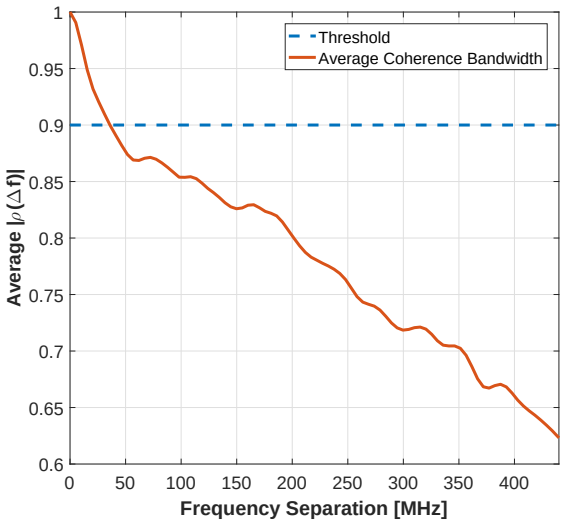

(b)

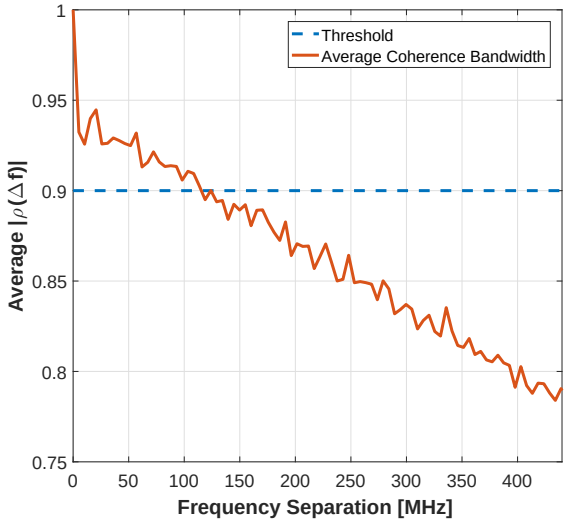

(c)

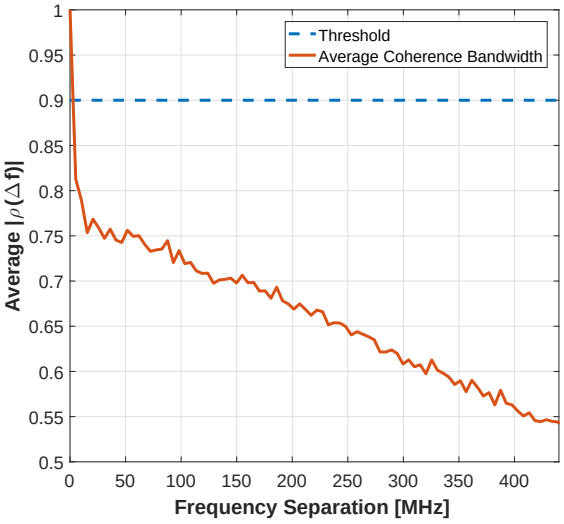

(d)

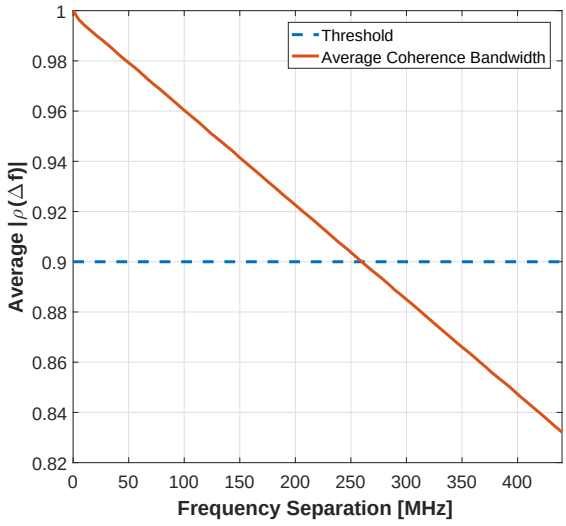

(e)

Figure 5.7: Coherence bandwidth for the channel models: a) CM1, b) CM2, c) CM3, d) CM4 and e) CM9.

Table 5.3 presents the average time dispersion parameters for each multipath environment obtained from the average PDPs, where $\bar{\tau}_{rms}$ is average the RMS delay, $\bar{\tau}_{max}$ represents the average of maximum delay spread, $\bar{B}_{c_{0.9}}$ is the average coherence bandwidth and HPBW is the Half Power Beamwidth of TX/RX antennas. From its analysis, it can be verified that CM4 is strongly characterized by multipath fading, which means that for lower power regimes e.g. EIRP = 20 dBm it is not possible to acquire the time dispersion parameters. Although $\bar{\tau}_{max}$ of CM9 is relatively high, $\bar{\tau}_{rms}$ shows that the last PDP component considered it is not significant and therefore the environment is characterized for low multipath components. If considered a EIRP of 20 dBm the remaining multipath components are masked and then only LOS component is considered which prevents the calculation of the multipath statistical parameters. From Table 5.3, it is also verified that the most frequency selective fading channel is CM4, since the B_c is only 2.76 MHz.

Table 5.3: Statistical parameters for each multipath channel environment.

CM #	**EIRP** (dBm)	$\bar{\tau}_{rms}$ (ns)	$\bar{\tau}_{max}$ (ns)	$\bar{B}_{c_{0.9}}$ **(MHz)**	**HPBW°** **(TX/RX)**
1	40	9.10	43.20	25.83	(360,15)
	20	8.90	32.60	25.83	
2	40	8.23	61.70	36.16	
	20	8.17	45.45	36.16	
3	40	31.60	411.70	123.90	(30,30)
	20	29.80	279.90	123.90	
4	40	75.55	484.80	2.76	(30,15)
	20	N/A	N/A	N/A	
9	40	2.40	127.65	268.65	(30,30)
	20	N/A	N/A	N/A	

5.2.2 Link budget

To find the maximum operation range of a wireless communication, the path loss between the transmitter and receiver must be known. The PL describes the attenuation of mean power as function of distance and it is modeled for 60 GHz signals according to (3.12).

The representation of (3.12) as function of distance traveled is despited in Figure 5.8 for each CM, taking into account the values of each variable presented in Table 5.4. As it can be seen from this figure, the path loss varies from each CM model to

another, where NLOS scenarios, such as CM2 and CM4, are characterized for much higher losses than the other channel models in LOS scenario.

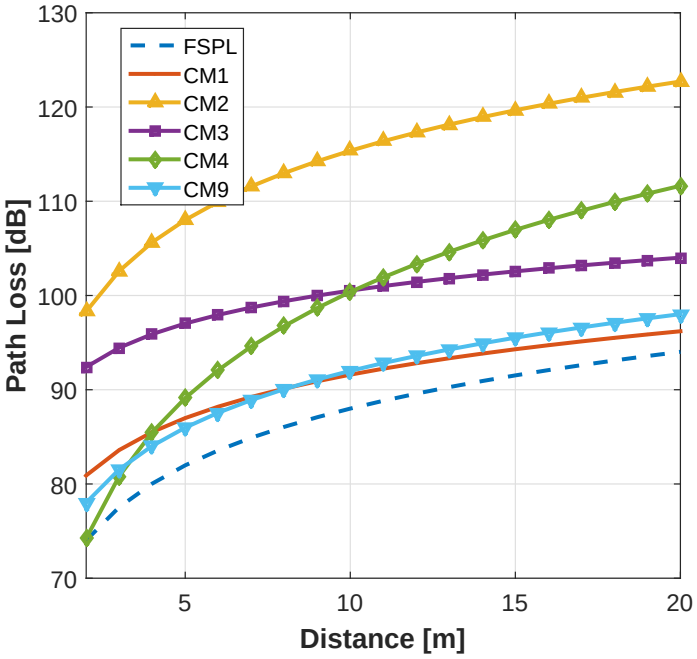

Figure 5.8: Path loss in function of distance for each channel model.

Table 5.4: Typical values of n, $PL_0|_{dB}$ and $X_\sigma|_{dB}$ for different environments and scenarios [1].

CM #	**n**	PL_o **(dB)**	σ_s **(dB)**
1	1.53	75.1	1.5
2	2.44	86	6.2
3	1.16	84.6	5.4
4	3.74	56.1	8.6
9*	2	68	5

* the parameters considered for this CM are the ones suggested by [79].

Consequently, the PL value in its maximum range can also be obtained from a link budget equation, represented in (5.2) [80]:

$$PL = EIRP + G_{RX} - P_N - E_b/N_o - IL - M \ [dB], \tag{5.2}$$

where, $EIRP$ is the Equivalent Isotropically Radiated Power, P_N is the average noise power per bit, where $P_N = N + N_f$ and $N = -174 + 10\log 10(throughput[bps])$, N_f is

the receiver noise figure, IL is the implementation loss of the transceiver and M the 60 GHz link margin. Additionally, N_f and IL are usually characterized by 8 dB and 2 dB, respectively [79].

Finally, relating both equations (3.12) and (5.2), the maximum operation range for a required E_b/N_o is calculated using the following equation [80]:

$$d = 10^{(PL-PL_o)/10n} \ [m] \tag{5.3}$$

Based on the suggested EIRP of 40 dBm [1] and a receiver gain antenna (G_{RX}) of 10 dBi, the maximum operating range can be estimated for a specific E_b/N_o and with either presence or absence of human shadowing.

5.2.3 Mobility

Considering that the transmission channel varies over time due to movements of objects and persons in the environment or moving antennas at the transmitter and/or receiver, the coherence time of the communications system must be considered. According to [50] and as stated in Section 3.4.1, the coherence time T_{coh} is approximately the inverse of the Doppler spread ($2f_d$).

Considering Eq. 3.13 and a carrier frequency $f_c = 60$ GHz, maximum walking speed of 2 m/s and $c = 3 \times 10^8$ m/s, the maximum Doppler shift becomes $f_{Doppler} = 400$ Hz. The presence of many persons moving at various speeds up to 2 m/s results in a Doppler spread of about 800 Hz, which corresponds to a coherence time of 0.625 ms. This means that pilot symbols for channel estimation purposes must be transmitted with a period lower than 0.625 ms.

5.3 Uncoded OFDM system Assessment

As stated before, for performance evaluation purposes, the parametrization used in the proposed framework are the ones suggested by IEEE 802.15.3c [2]. The summary of the considered system parameters are presented in Table 2.5. Note that these parameters are based in the High Speed Interface physical layer (HSI-PHY) of the standard.

Firstly, to ensure that the estimation process was implemented correctly, a group of 100 simulations for each environment was performed. Since the channel impulse response (CIR) is known (Section 5.2.1), it is possible to estimate the channel perfectly. This process was called ideal estimation. In order to unmask any disturbances external to channel estimation imperfections, in this first stage a ideal estimation was considered. Figure 5.9 shows the first of 100 CFR simulations and respectively perfectly estimated response of CM1 and CM9. Mean square error was computed to assess the difference between all 100 simulations. As expected the MSE for this validation returned 0.

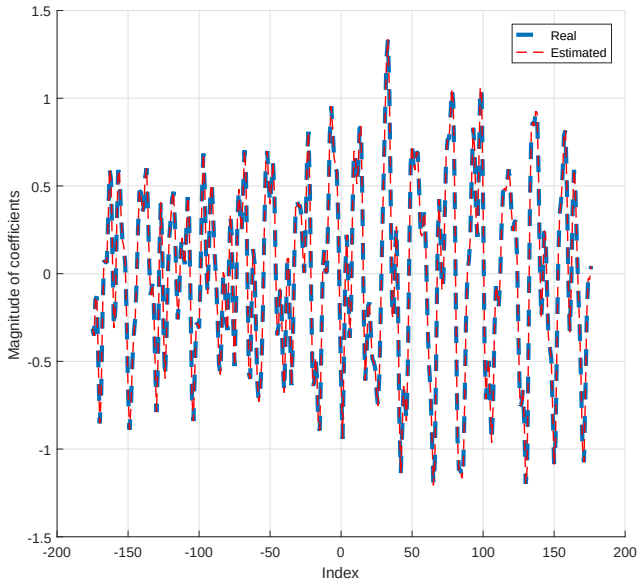

(a)

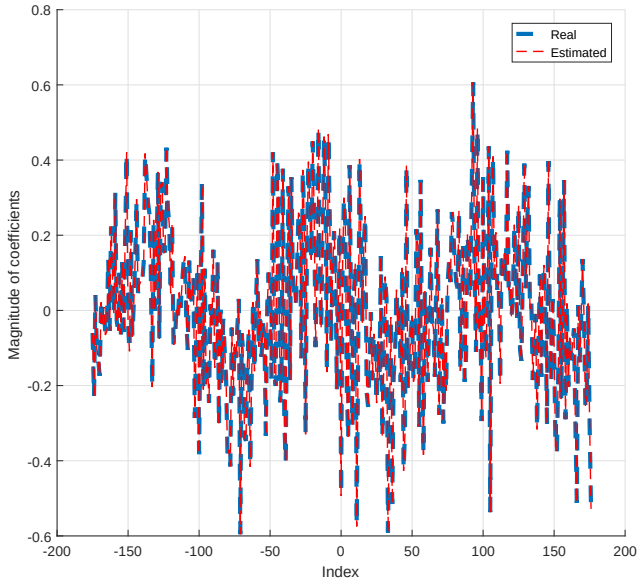

(b)

Figure 5.9: CFR estimation for: a) CM1 and b) CM9 considering ideal estimation.

Although the ideal CFR assessment showed that the estimation process is well implemented, BER performance is also a good metric to validate the system model performance. Thus, BER simulations were conducted for each of the 100 static channel realizations in each channel model. After collecting all 100 BER results, the mean of this curves is calculated. Figure 5.10 shows the BER curves for the uncoded OFDM system considering ideal estimation for all five channel model considered in this work.

Since it is considered ideal channel estimation, it was expected that BER results were similar to the results of a channel affected only by AWGN. Analyzing Figure 5.10, can be seen that only CM9 provides a probability of error close to AWGN channel. Therefore, it is clear that the performance of the system is being affected by other factor than channel estimation inaccuracy.

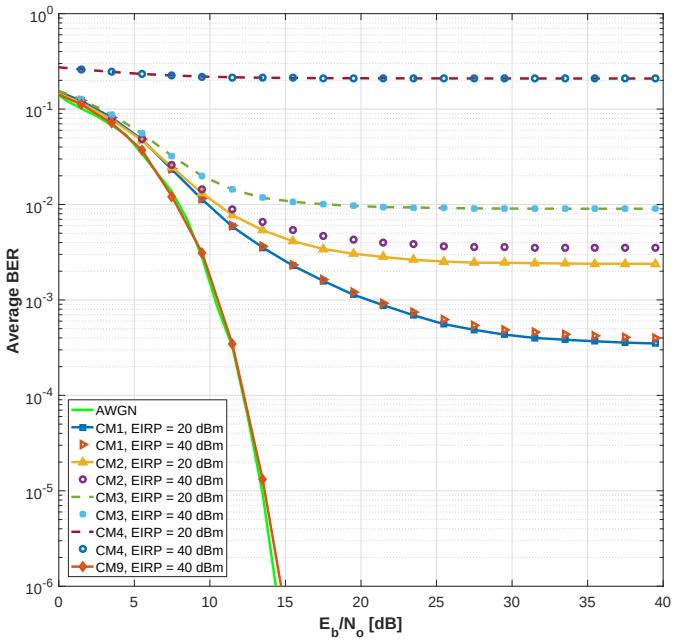

Figure 5.10: BER performance considering ideal estimation.

IEEE 802.15.3c standard suggests a cyclic prefix (CP) of 64 samples. If a sampling frequency of 2.64 GHz is considered, this means a T_{CP} of 24.24 ns (Table 2.5). Comparing the cyclic prefix time and the excess delay of each channel considered (Table 5.3), it can be seen that the condition which limits the T_{CP} to at least the excess delay [45] is not being respected. Therefore, it can be concluded that the orthogonality among subcarriers is not achieved, which means that the cyclic prefix extension length proposed by the standard is not valid for the channels considered in the framework.

5.3.1 Cyclic prefix length: parametric study

In order to improve the performance of the system, larger cyclic prefixes must be considered. Extending the CP leads to an increment of the system's overhead because more redundant information is transmitted, which leads also to a decrement of spectral efficiency. Therefore is mandatory to find a trade-off that ensures good performance with the minimum introduced overhead.

First, is important to assess the impact of the T_{CP} in the BER results for the channel models considered. For that, several simulations varying the T_{CP} were conducted and the result of such simulations are drawn in Figure 5.11. Note that is considered uncoded transmission, 16 QAM modulation, ZF equalization, ideal estimation and a EIRP of 40 dBm. Figure 5.11 shows the different BER results when changing only the CP length. It can be seen that CP strongly affects the overall system performance and needs to be defined based on the environment considered. From Figure 5.11 it is also possible to conclude that, for CM3 and CM4, a CP with the same length as the OFDM symbol is not enough to ensure good results. It means that only CP multiple of the OFDM symbol length could, eventually improve the BER performance og these channel models. Therefore, it would deteriorate significantly the spectral efficiency. For that reason, simulation results referring CM3 and CM4 will not be analyzed in this document. Note that, as expected, the uncoded performance for CM9 is not significantly affected by the length of CP, since for a T_{CP}=24.24 ns (Figure 5.10) it was already obtained good results.

Consider a T_{CP} significantly large comparing to the excess delay (τ_{max}) of the channel may lead to a unnecessary overhead, which compromises the system's throughput. Thus, a parametric study were conducted to find the most suitable length of CP for each environment. From this study it was concluded that consider $T_{CP} \simeq \tau_{max}$ is an appropriate metric since it ensures good BER performance and does not reduce significantly the throughput. The results of the T_{CP} study are drawn in Table 5.5 where can be seen the required E_bN_0 to ensure a BER of 10^{-6} for both 16 and 64 QAM modulation.

Table 5.5: T_{CP} study results.

CM	EIRP (dBm)	Mod.	$\bar{\tau}_{rms}$ (ns)	$\bar{\tau}_{max}$ (ns)	$\bar{B}_{c_{0.9}}$ (MHz)	T_{CP} study		
						T_{CP} (ns)	Throughput ($Mbps$)	EbN0 (dB)
1	40	16 QAM	9.10	43.20	25.83	43.94	5650	41
		64 QAM					8475	46
	20	16 QAM	8.90	32.60	25.83	32.95	5923	42
		64 QAM					8885	47
2	40	16 QAM	8.23	61.70	36.13	62.12	5249	38
		64 QAM					7873	43
	20	16 QAM	8.17	45.45	36.16	45.83	5605	43
		64 QAM					8408	48
9	40	16 QAM	2.40	127.65	268.65	24.24	6160	15
		64 QAM					9240	N/A

In the case of CM9, it does not make sense to assign a CP length in the same order of magnitude of the excess delay, because the last delay component shows to be insignificant if we look at the respective RMS delay spread. Knowing that for CM9, the T_{CP} suggested in the standard ($T_{CP} = 24.24$ ns) meets with the BER requirements (1 bit error per 1 million bits transmitted), it is this that will be considered in all simulations.

Through Figure 5.12 can be seen that despite CM1 and CM2 does not meet with AWGN BER curve, their performance is much better when compared with the results in Figure 5.10. With this improvement is possible to achieve the BER requirement of 10^{-6} for both 16 QAM and 64 QAM modulation.

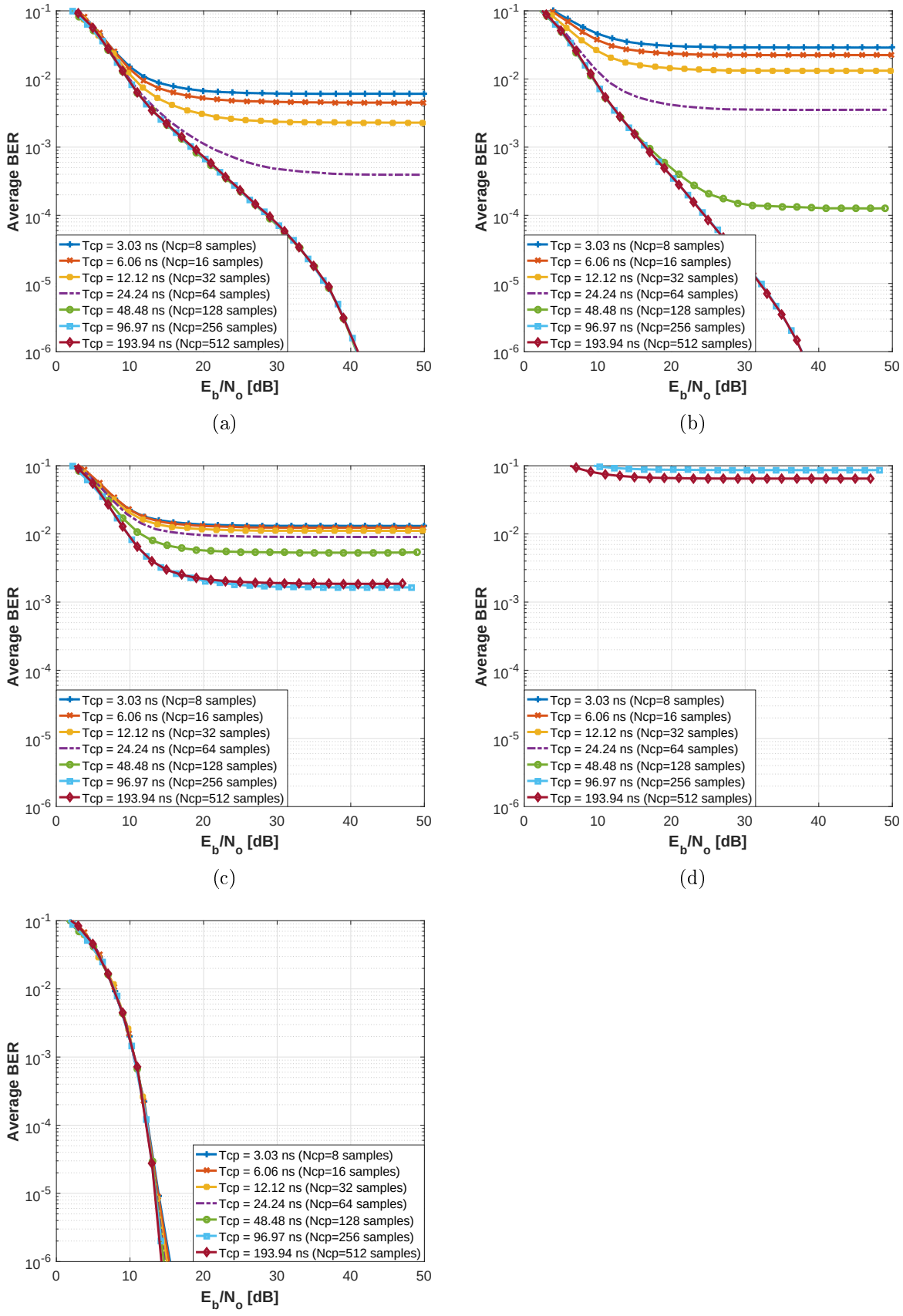

Figure 5.11: Effect of T_{CP} in BER performance for: a) CM1, b) CM2, c) CM3, d) CM4 and e) CM9 for 16 QAM modulation and EIRP of 40 dBm.

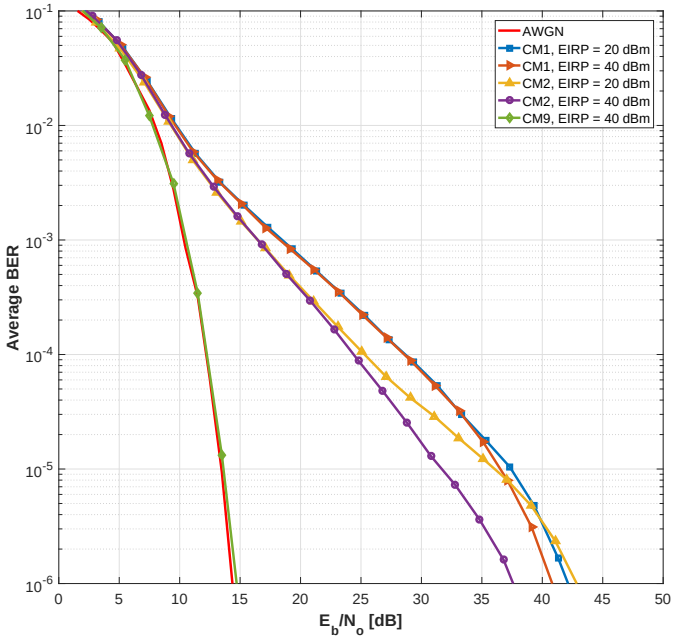

(a)

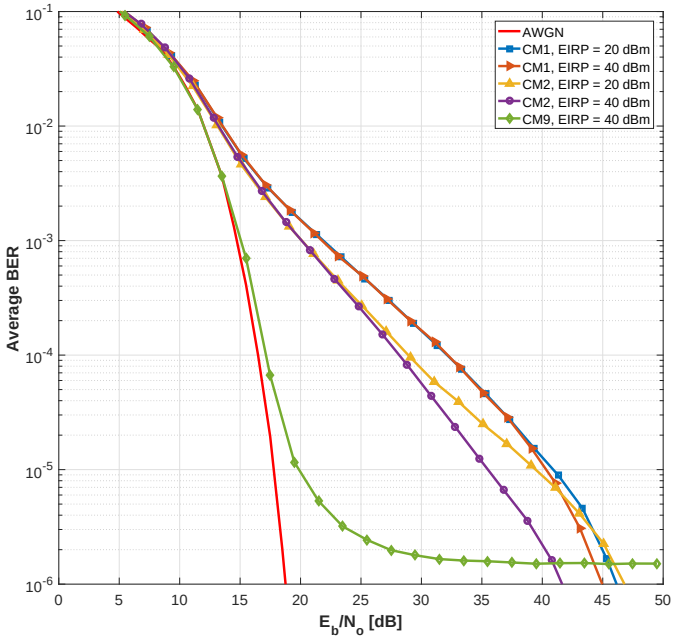

(b)

Figure 5.12: BER results of T_{CP} for a) 16 QAM and b) 64 QAM.

5.3.2 Pilot-based channel estimation

In order to evaluate the performance of the mulitgigabit framework employing channel estimation through the use of pilot tones, three pilot allocation modes were considered.

One of the pilot allocation modes is based on the IEEE 802.15.3c standard [2] suggestion that implements a comb type pilot arrangement, as detailed in Section 2.3.2. The other mode consists also in a comb type allocation, but considering pilot tones equally spaced along with the OFDM symbol. Finally the performance of channel estimation block is assessed applying a block type allocation method.

If pilot tones are inserted into the OFDM symbol according to an uniform distribution, $X_l(k)$ can be expressed by Eq. 5.4 [57].

$$X_l(k) = X_l(mL + n) = \begin{cases} x_p(m), & n = 0 \\ Data, & n = 1, ...L - 1 \end{cases} \tag{5.4}$$

where L represents the number of subcarriers between pilots and $x_p(m)$ the value of the m^{th} pilot subcarrier.

Note that the number of subcarriers between pilots should be limited by the coherence bandwidth of each fading channel model ($B_{c_{0.9}}$) in order to avoid amplitude and phase distortion [45].

If the third pilot estimation method is considered, all the subcarriers available for data and pilots in the OFDM symbol are assigned with pilot signals, constituting a pilot symbol. As defined in section 3.4.1, the pilot symbol must be transmitted with a periodicity lower than the coherence time of the fading channel model (T_{coh}).

Figure 5.13 and Figure 5.14 shows the multigigabit framework performance using channel estimation based on the pilot allocation suggested in IEEE 802.15.3c standard. In Figure 5.13 BER curves are drawn for both power regimes employing 16 QAM modulation scheme for CM1, CM2, CM3, CM4 and CM9. It can be seen that none of the channel models reaches de BER performance goal of 10^{-6}, only CM9 presents a reasonable performance. This poor results shows that the implemented channel estimation block is not suitable for the environments considered, since the number of pilot subcarriers proposed by IEEE 802.15.3c standard for channel estimation is not enough to characterize the multipath channel model.

The other way to asses the poor channel estimation performance for the channel models in this study, is to compare the estimated channel frequency response wit the CFR known. Thus, Figure 5.14 presents the estimated CFR based on the 16 pilot subcarriers inserted according to the standard. It is clear that the estimated CFR is

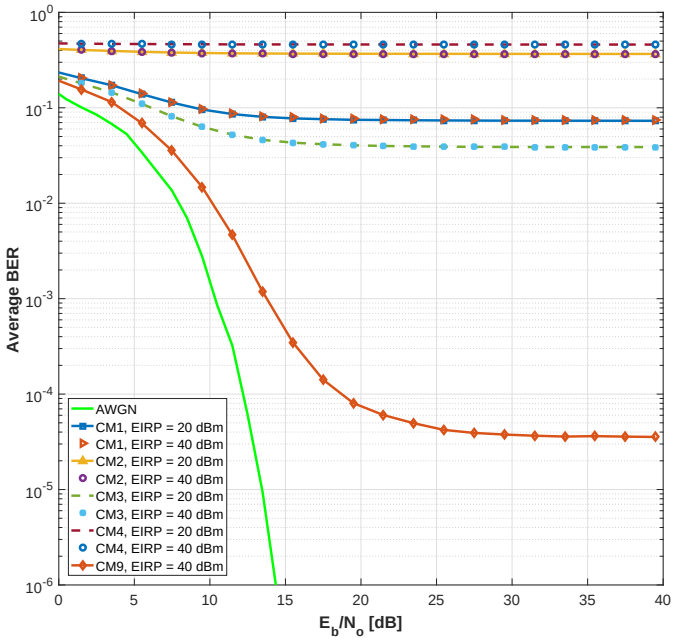

Figure 5.13: BER performance for CM1, CM2, CM3, CM4 and CM9 considering pilot estimation according to IEEE 802.15.3c.

far from the real channel response. The fact that only 16 pilot subcarriers are used for the whole channel which varys in frequency as much as the channel models considered, leads to a significant loss of sampling resolution. From Figure 5.14 can be seen that the estimated channel frequency response is not sensible to the variations that happen in the real channel. Consequently, the resulting mean square error of the estimation is extremely high, as shown in Table 5.6.

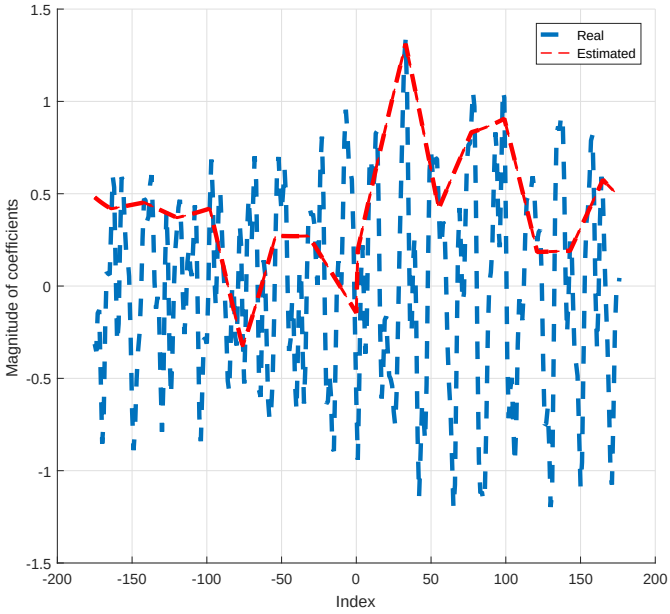

(a)

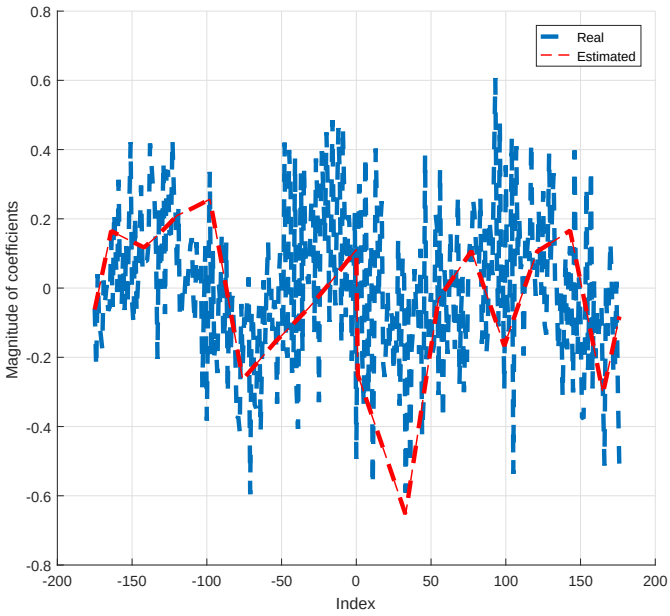

(b)

Figure 5.14: CFR estimation for: a) CM1 and b) CM9 considering pilot arrangement according to IEEE 802.15.3c.

Since neither BER assessment or CFR estimation evaluation meet the minimum requirements for this study, it can be concluded that the pilot allocation suggested in the standard is not suitable for the considered environments. This means that the number of pilot tones within the OFDM symbol must be increased.

Table 5.6: MSE of the channel estimation process according to the suggested in IEEE 802.15.3c standard.

CM #	EIRP (dBm)	MSE (dB)
1	40	-2.58
	20	-3.32
2	40	9.39
	20	9.33
3	40	-2.07
	20	-2.07
4	40	16.31
9	40	-18.33

According to [15], the number of subcarriers spacing between the pilots in frequency domain, D_P, is given by

$$D_P \leq \frac{1}{\tau_{max}\Delta df} \tag{5.5}$$

so that the variations of the channel in frequency can be all captured. Note that Δdf represents the frequency separation between subcarriers.

[19] denotes that in order to meet the frequency domain Nyquist criterion of sampling the channel response, the minimum pilot density, D_P, must be

$$D_P \leq \frac{T_s - T_{CP}}{\tau_{max}} \tag{5.6}$$

, where T_s is the OFDM symbol time.

Comparing pilot density equations from the previous publications, can be seen that both equations proposes similar density of pilots, because if subcarriers orthogonality is considered, so the following equality is valid.

$$\Delta df = \frac{1}{T_s - T_{CP}} \tag{5.7}$$

Table 5.7 shows the pilot subcarriers density for the channel models studied ac-

cording to Eq. 5.5 and Eq. 5.6. The number of pilots presented in the OFDM symbol (N_P) is calculated according to the value of D_P.

Table 5.7: Pilot subcarriers density, according to [15] and [19].

CM #	EIRP (dBm)	τ_{max} (ns)	D_p	N_p
1	40	43.20	≤ 5	≥ 71
	20	32.60	≤ 6	≥ 59
2	40	61.70	≤ 4	≥ 88
	20	45.45	≤ 5	≥ 71
9	40	127.65	≤ 1	≥ 352

BER curves for a pilot subcarriers allocation with the parameters presented in Table 5.7 are depicted in Figure 5.15. Analyzing the results, can be concluded that the pilot allocation algorithm proposed by [15] and [19] is not suitable for the channel models considered. CM9 is the only channel model that presents a good BER performance, since it was attributed a excessive number of pilot subcarriers due to the fact that its τ_{max} does not represent properly the channel model characteristics.

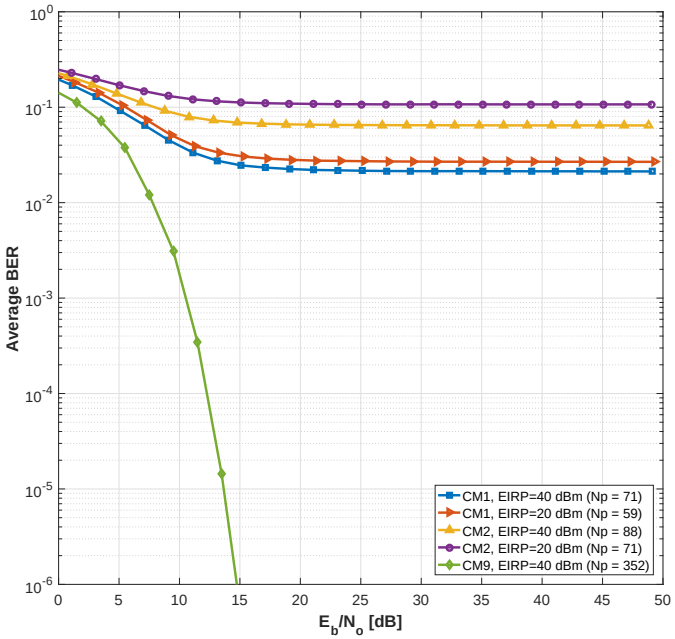

Figure 5.15: BER performance for CM1, CM2 and CM9 for both power regimes considering pilot allocation according to [15] and [19].

In order to find a suitable pilot allocation approach, a parametric study focused on the number of pilots presented in the OFDM symbol was conducted. With this study it is intended to find the minimum number of subcarriers assigned with pilot tones that meets with the system requirements and does not compromises the overall system throughput. It was considered a linear distribution of the pilot subcarriers along with the 352 subcarriers available for data and pilot tones [2]. In this study, 100 simulations were performed for four different number of pilot subcarriers in the symbol (N_P). Note that a $N_P = 352$ means that all the subcarriers are assigned with pilot tones, which means that no data is transmitted in the OFDM symbol.

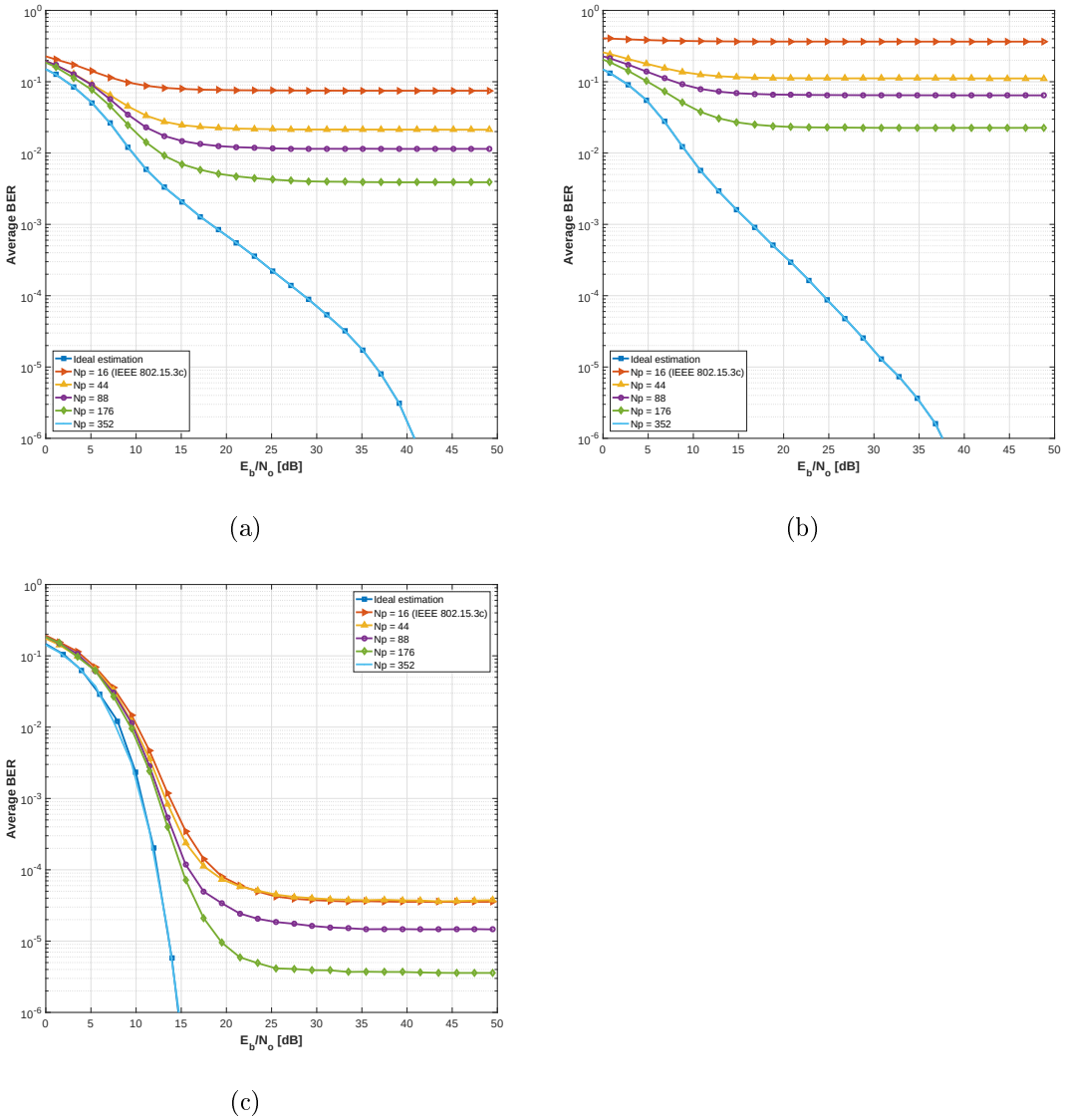

Figure 5.16: Pilot allocation effect on BER performance for: a) CM1, b) CM2 and c) CM9.

From Figure 5.16 can be seen that the BER requirement is only achieved if all sub-

carriers are assigned to pilot tones. Thus, it can be concluded that channel estimation using pilot subcarriers with comb type arrangement (Section 3.4.1) it is not efficient for the environments considered. Therefore, in this work a block type pilot arrangement is proposed for frequency channel estimation. For that, the transmission period of the pilot symbol must be known and should be lower than the coherence time of the channel [45] in order to be able to consider that channel is invariant in time-domain.

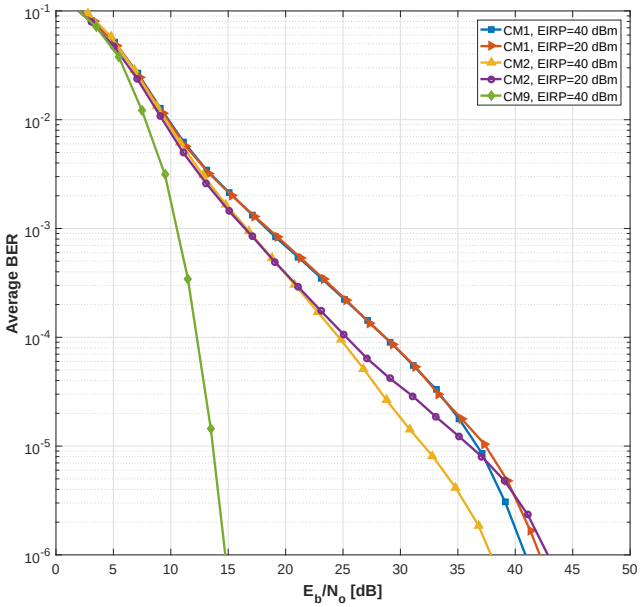

(a)

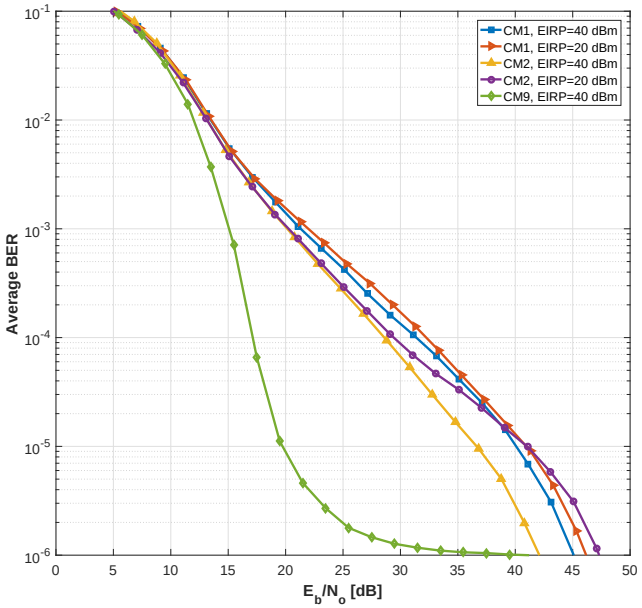

(b)

Figure 5.17: BER performance using pilot subcarriers in block type arrangement for (a) 16 QAM and (b) 64 QAM.

5.3.3 CES-based channel estimation

As stated in Section 3.4.2 and Section 4.7.1.2, for the proposed framework, Golay sequences are used as channel estimation sequences. The structure of the CES considered in the performance evaluation tests, is based on the suggestion of [11] and [7]. As expected, the CES is composed by two parts (Figure 5.18): part a and part b, where each part contains three sequences of length 256, a cyclic prefix and a cyclic postfix. The cyclic prefix corresponds to the the last 128 samples of the sequence, while cyclic postfix contains the remaining samples.

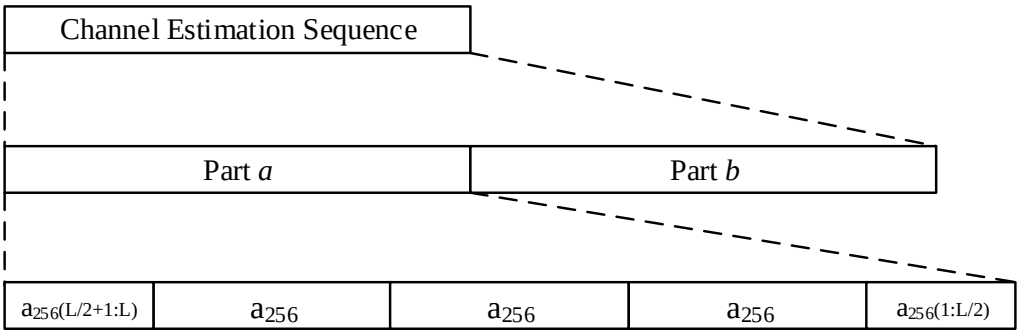

Figure 5.18: Channel estimation sequence structure.

The auto-correlation process proceeds according to the implementation presented in Section 4.7.1.2 and the corresponding performance indicators are analyzed based on BER curves. Figure 5.19 shows the performance of a OFDM transmission considering 16 QAM modulation for the environments under study. From BER results can be concluded that channel estimation based on Golay sequences ensure that the BER requirement of 1 error bit in 1 million is achieved. It can be seen also that, as have been happening in previous results, CM9 ensure the BER target at a much lower noise level ($E_b/N_0 \approx 18dB$) when compared with the other channel models($E_b/N_0 \approx 40dB - 45dB$).

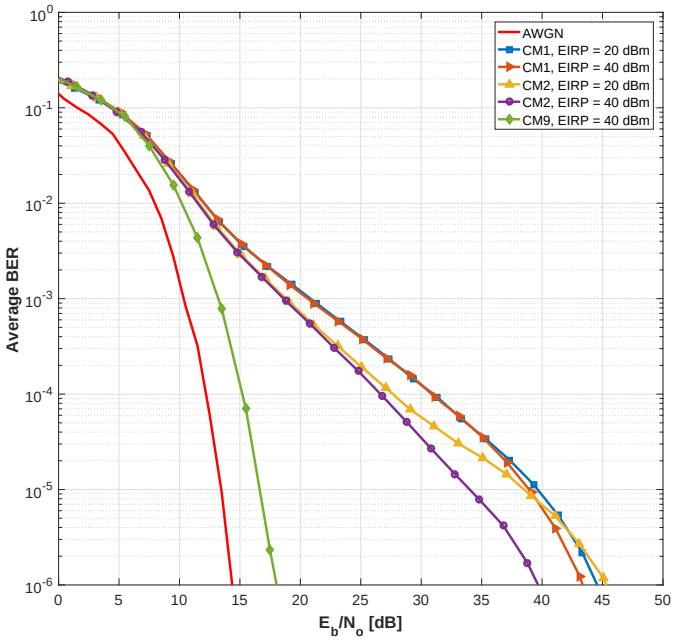

Figure 5.19: BER performance using CES-based channel estimation.

5.4 Coded OFDM system results

In order to implement a realistic coded transmission system, FEC codes proposed in IEEE 802.15.3c standard are considered. Between the code rates proposed by the standard for HSI PHY, rates of 1/2 and 3/4 are used by employing LDPC(336,672) and LDPC(336,672) codes, respectively. Additionally, concatenated codes were also implemented in the proposed framework, as referred in Section 2.3.2.

As explained in Section 4.3, in order to implement LDPC coding technique in the proposed framework, the parity check matrix must be known. The matrix permutation indexes of the parity check matrix is given by the standard and is depicted in Figure A.4 and Figure A.5 for LDPC(336,672) and LDPC(504,672), respectively. The insertion of the matrix permutation into the framework was carried with the procedure explained in Section 2.3.2.

The implementation of concatenated encoder is performed with RS code and convolutional code as presented in Section 4.3.

Figure 5.20 presents the BER results of the three FEC codes considered for each indoor environment, 16 QAM modulation and pilot-based channel estimation. Firstly

it is verified that for all FEC codes it is possible to achieve the BER target of 10^{-6}. It can be seen also that CM9 presents a very good BER performance, since it is close to Shannon limit (Section 4.9). Concerning the other channel models, in Figure 5.20 it is shown that LDPC codes ensures a probability of error of 10^{-6} for values of E_b/N_0 higher than 37 dB. Considering concatenated codes, CM2 clearly outperforms CM1 in both power regimes. With this codes and assuming channel model 2, it is needed a E_b/N_0 of about 23 dB - 24 dB to ensure a ratio of 1 error in 1 million bits transmitted. For CM1 it is required a E_b/N_0 of more than 30 dB.

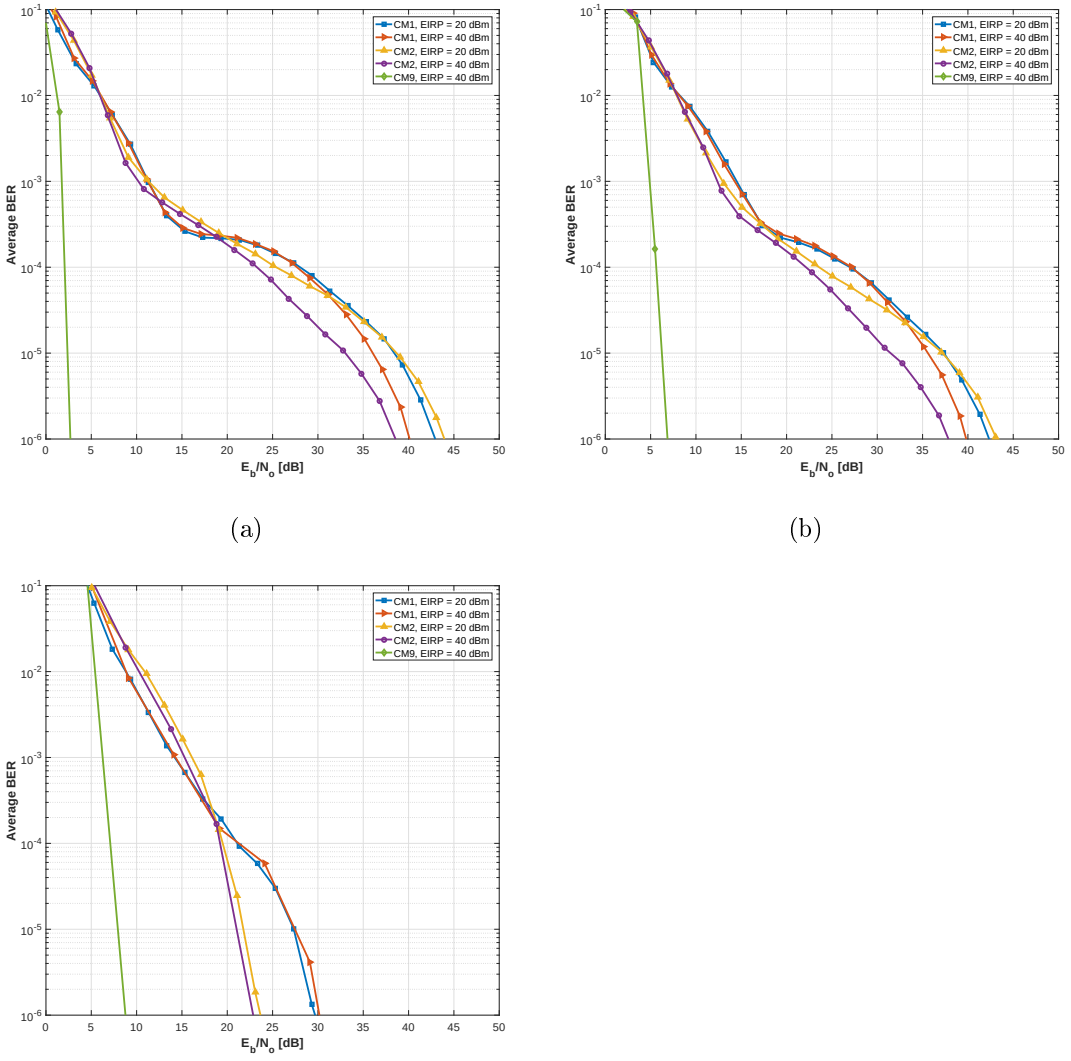

(a)

(b)

(c)

Figure 5.20: BER performance using FEC codes: a) LDPC(336,672), b) LDPC(504,672) and c) concatenated codes.

5.5 Comparative analysis

In this section, a comparative analysis of the simulations above is performed. The aim of this analysis is to compare the channel estimation techniques (pilot-based and with Golay complementary sequences) as well as the FEC codes implemented. After this section it is intended to identify the most suitable configuration for a multigigabit transmission system towards 5G communications.

The comparative analysis is performed for each channel model separately It is considered five different channel models being them CM1 for EIRP = 20 dBm, CM1 for EIRP = 40 dBm, CM2 for EIRP = 20 dBm, CM2 for EIRP = 40 dBm and finally, CM9 for and EIRP of 40 dBm. For each CM will be compiled simulation results for uncoded transmission considered ideal estimation, pilot-based estimation and CES-based (Golay) estimation. The results for coding transmission are presented considering pilot-based channel estimation and three FEC codes are evaluated: LDPC(336,672), LDPC(504,672) and concatenated coding. Both for uncoded or coded transmission, 16 QAM and 64 QAM are selected as modulation scheme. Note that Golay-based channel estimation is considered only for 16 QAM.

The metrics considered for the comparative analysis are based in the BER performance and the throughput achieved for each channel estimation technique or FEC code. From BER analysis it is assessed the required E_b/N_0 in order to ensure a probability of error of 10^{-6}, as well as the differential E_b/N_0 ($\Delta E_b/N_0$) for all studies relatively to uncoded ideal estimation. This last analysis is performed for a probability of error of 10^{-3} and 10^{-6}. The efficiency of each parametrization is assessed through the analysis of throughput.

Figure 5.21 shows the BER performance results of both uncoded and coded transmission employing 16 and 64 QAM modulation scheme for LOS residential environment considering an EIRP of 20 dBm. Comparing the BER curves, can be seen that for a probability of error of 10^{-3} and above, the performance of coded transmission presents better results than uncoded ones. It is in accordance with the simulation results presented in section 4.9. For a BER lower than 10^{-3} the LDPC code performance tends to equalize the uncoded results, for both 16 QAM. This phenomenon it is present also in CM1 for EIRP = 40 dBm (Figure 5.22) and for both power regimes of CM2 (Figure 5.22 and Figure 5.22). Note that, in this range of BER (10^{-3} - 10^{-6}) for all mentioned channel models, the Reed-Solomon codes performs much better than LDPC for both 16 and 64 QAM modulation.

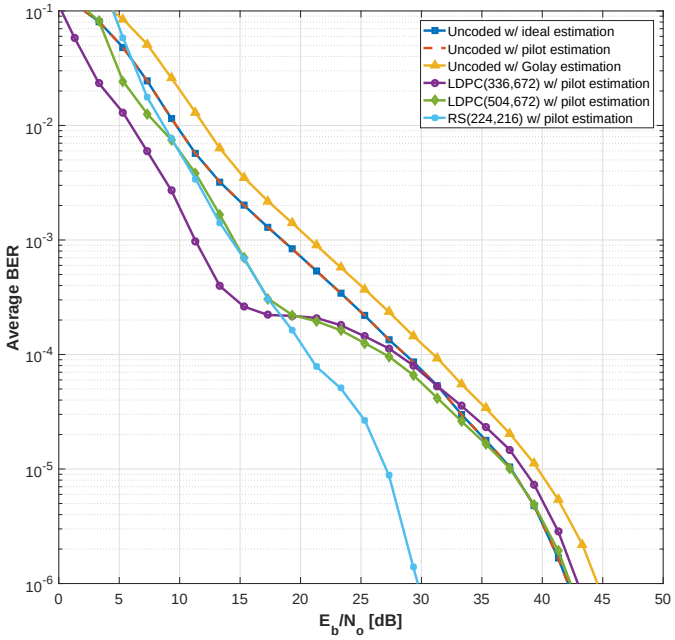

(a)

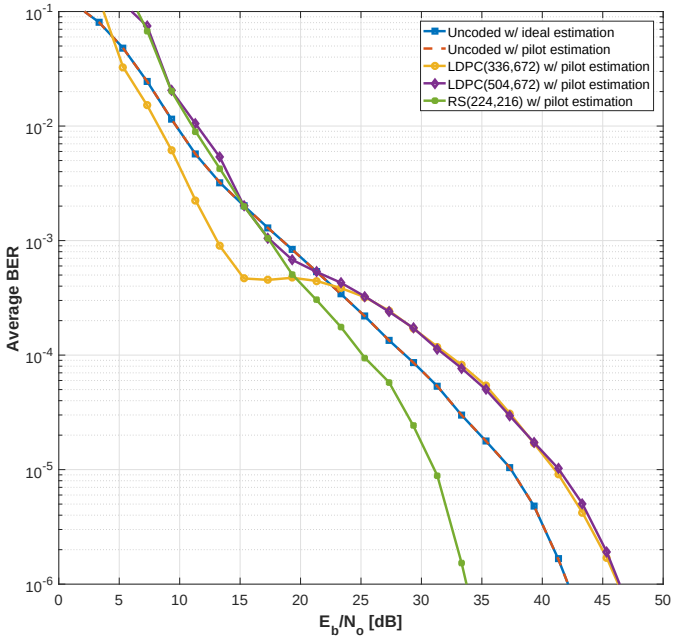

(b)

Figure 5.21: BER results for LOS residential channel mode CM1, considering EIRP = 20 dBm for (a) 16 QAM and (b) 64 QAM.

In order to perform a more objective analysis of CM1 performance results, in Table 5.8 and Table 5.8 a detailed characterization of BER results is exposed for EIRP of 20 dBm and 40 dBm, respectively. It can be found also the obtained throughput for each channel estimation technique or FEC code considered.

Table 5.8: Simulation results for LOS residential channel mode CM1 for EIRP = 20 dBm.

Modulation	Parametrization	E_b/N_0	$\Delta E_b/N_0$ (dB)		Throughput
		(dB)	@BER=10^{-3}	@BER=10^{-6}	(Mbps)
16 QAM	Uncoded Ideal	42	N/A	N/A	6205
	Uncoded Pilot	42	0	0	6186
	Uncoded Golay	45	2.0	3	6129
	LDPC(336,672)	43	-6.0	1	3093
	LDPC(504,672)	42.5	-4.0	0.5	4639
	RS(224,216)	29	-4.2	-12	3976
64 QAM	Uncoded Ideal	42	N/A	N/A	12411
	Uncoded Pilot	42	0	0	12373
	LDPC(336,672)	46.5	-5.5	4.5	6186
	LDPC(504,672)	46.5	-1	4.5	9279
	RS(224,216)	34	-1	-8	7953

Analyzing both table results, it is clear the change on BER performance before and after a probability of error of 10^{-3}. The $\Delta E_b/N_0$ parameter shows that, considering a BER of 1 in 1 million, only Reed-Solomon stands out in terms of performance when compared with uncoded transmission. On the other hand, if it is admitted a higher BER in the wireless system, then LDPC(336,672) codes outperforms RS.

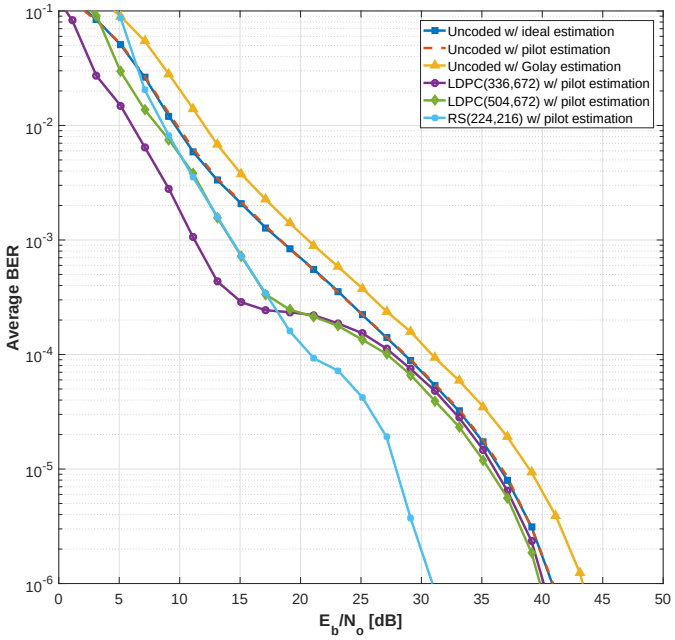

(a)

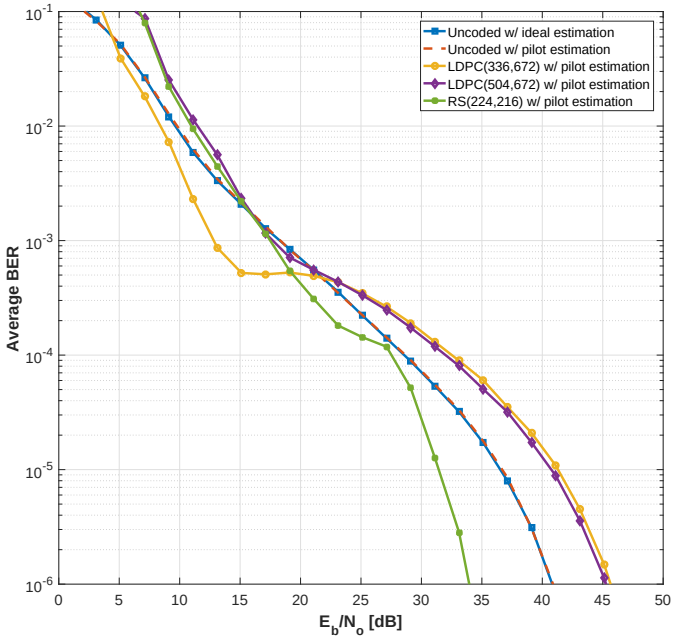

(b)

Figure 5.22: BER results for LOS residential channel mode CM1, considering EIRP = 40 dBm for (a) 16 QAM and (b) 64 QAM.

For both power regimes of LOS residential environment, the uncoded transmission using pilot subcarriers in block type for channel estimation performs closely to the results of uncoded transmission considering ideal estimation. Then, if Golay sequences are used for channel estimation, it is expected to have a BER performance degradation

of 2 up to 3 dB. In terms of throughput, this results shows that the implementation of a multigigabit framework employing pilot-based channel estimation provides a throughput of 6.186 Gbps and 5.9 Gbps for a EIRP of 20 dBm and 40 dBm, respectively. This throughput values when compared with the ones for CES-based channel estimation makes possible to conclude that pilot-based estimation is more efficient for CM1.

Table 5.9: Simulation results for LOS residential channel mode CM1 for EIRP = 40 dBm.

Modulation	Parametrization	E_b/N_0 (dB)	$\Delta E_b/N_0$ (dB)		Throughput (Mbps)
			@BER=10^{-3}	@BER=10^{-6}	
16 QAM	Uncoded Ideal	41	N/A	N/A	5919
	Uncoded Pilot	41	0	0	5900
	Uncoded Golay	43.5	2.0	2.5	5846
	LDPC(336,672)	40.5	-6.0	-0.5	2950
	LDPC(504,672)	40	-4.0	-1	4425
	RS(224,216)	30.5	-4.2	-10.5	3793
64 QAM	Uncoded Ideal	43	N/A	N/A	11838
	Uncoded Pilot	43	0	0	11801
	LDPC(336,672)	45.5	-5.5	2.5	5900
	LDPC(504,672)	45	-1	2	8851
	RS(224,216)	34	-1	-9	7586

In terms of the use of FEC codes for CM1 and 16 QAM, it can be seen that RS(224,216) allows a significant BER performance improvement that varies from 10.5 dB for a EIRP of 40 dBm and goes up to 12 dB improvement if considering EIRP = 20 dBm. In the case of 64 QAM. this difference is not so significant. LDPC(336,672) shows an overall better performance when comparing with LDPC(504,672), which was expected since the last one employs a higher code rate FEC.

In Figure 5.23 and Figure 5.24 is depicted the BER performance simulation of 16 QAM and 64 QAM modulation for NLOS residential environment (CM2) considering EIRP = 20 dBm and 40 dBm, respectively. Note that the offset of the BER curve for Golay-based estimation relatively to pilot estimation remains in both configurations.

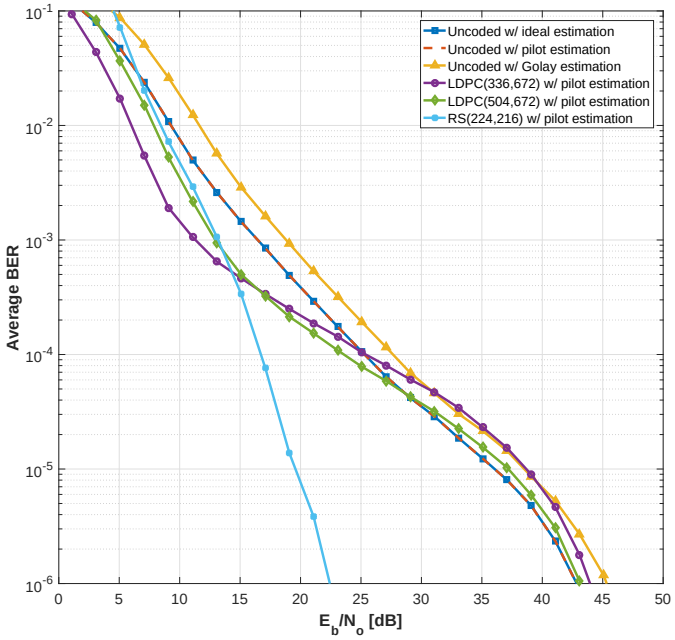

(a)

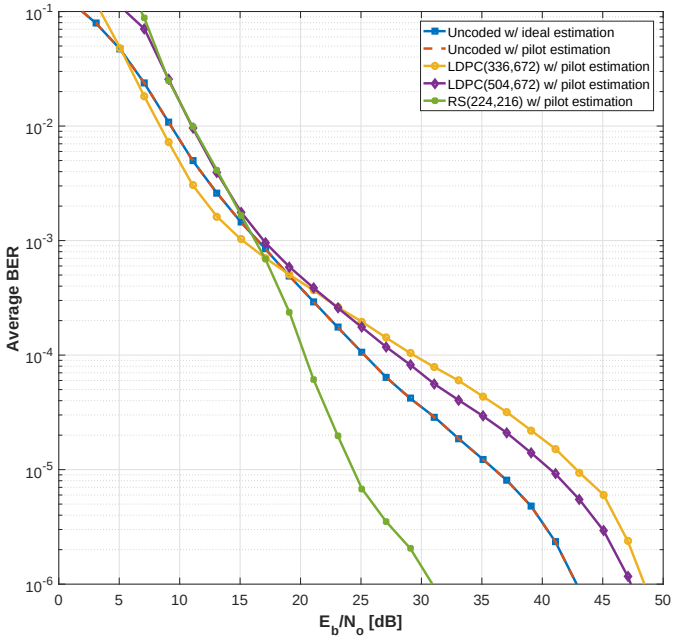

(b)

Figure 5.23: BER results for NLOS residential channel mode CM2, considering EIRP = 20 dBm for (a) 16 QAM and (b) 64 QAM.

Table 5.10 shows that for a BER of 10^{-6}, pilot-based channel estimation is the most suitable parametrization in uncoded mode using both 16 QAM and 64 QAM constellations. In addition to ensuring lower E_b/N_0 (43 dB) for the BER target, pilot-based estimation also provides higher throughput when compared with Golay sequences

for the same setup.

Table 5.10: Simulation results for NLOS residential channel mode CM2 for EIRP = 20 dBm.

Modulation	Parametrization	E_b/N_0 (dB)	$\Delta E_b/N_0$ (dB) @BER=10^{-3}	$\Delta E_b/N_0$ (dB) @BER=10^{-6}	Throughput (Mbps)
16 QAM	Uncoded Ideal	43	N/A	N/A	5872
	Uncoded Pilot	43	0	0	5854
	Uncoded Golay	45.5	2.5	2.5	5800
	LDPC(336,672)	44	-5.5	1	2927
	LDPC(504,672)	43.5	-4.0	0.5	4390
	RS(224,216)	24	0	-19	3763
64 QAM	Uncoded Ideal	43	N/A	N/A	11744
	Uncoded Pilot	43	0	0	11708
	LDPC(336,672)	48	-1	5	5854
	LDPC(504,672)	47	1	4	8781
	RS(224,216)	31	-0.5	-12	7526

As already shown in previous simulations, CM2 for an EIRP of 40 dBm results in a better overall performance compared with EIRP = 20 dBm. This conclusion is confirmed analyzing Table 5.11 since it is obtained a E_b/N_0 of 38 dB for a BER of 10^-6 which corresponds to a improvement of at least 5 dB for uncoded transmission.

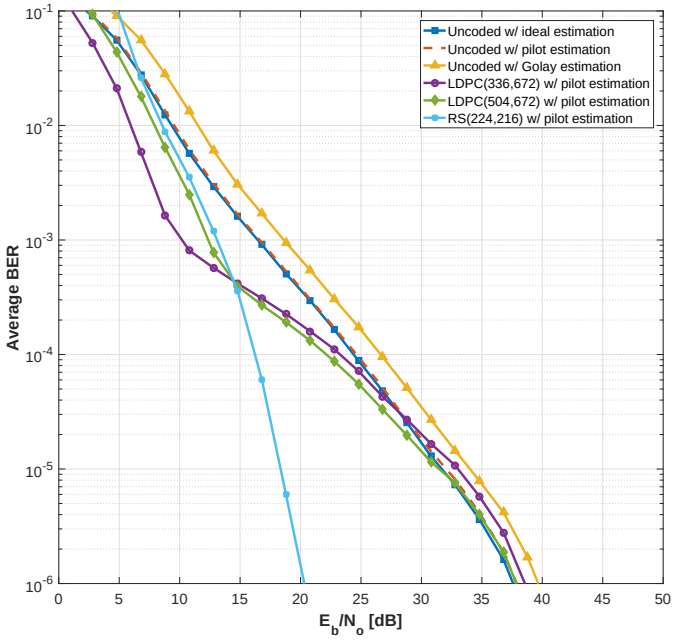

(a)

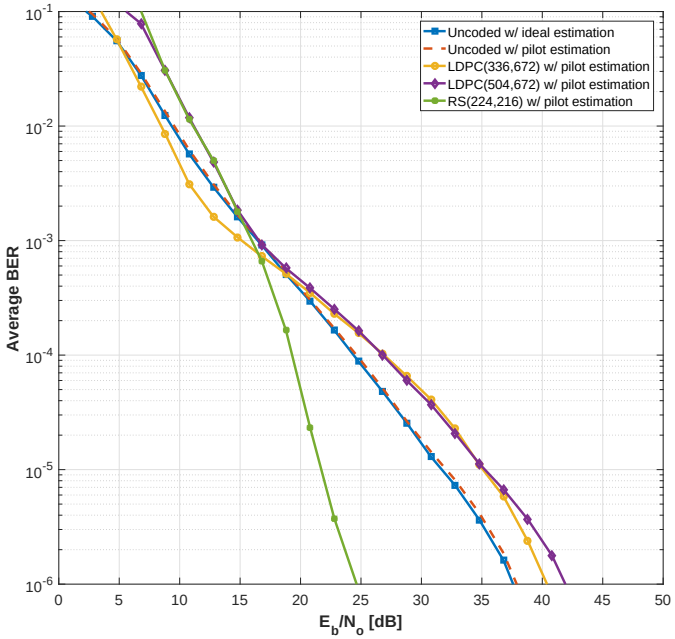

(b)

Figure 5.24: BER results for NLOS residential channel mode CM2, considering EIRP = 40 dBm for (a) 16 QAM and (b) 64 QAM.

In terms of coding performance it is important to refer that despite LDPC results be similar to the ones for uncoded setup, Reed-Solomon codes presents a significant improvement. From Table 5.10 and Table 5.11 can be seen that for the BER target RS(224,216) codes outperforms LDPC codes in 19 and 14.5 dB respectively. However,

for lower BER values, LDPC codes enables better performance.

The expected throughput for uncoded transmission in a NLOS residential environment is about 5.5 Gbps - 6.4 Gbps for 16 QAM modulation while if 64 QAM is used it is possible to achieve data rates of 11 Gbps. If FEC codes are with 16 QAM, throughput can vary from 2.74 Gbps up to 4.39 Gbps, but if 64 QAM modulation is selected it varies from 5.48 Gps up to 8.78 Gbps.

Table 5.11: Simulation results for NLOS residential channel mode CM2 for EIRP = 40 dBm.

Modulation	Parametrization	E_b/N_0 (dB)	$\Delta E_b/N_0$ (dB)		Throughput (Mbps)
			@BER=10^{-3}	@BER=10^{-6}	
16 QAM	Uncoded Ideal	37.5	N/A	N/A	5498
	Uncoded Pilot	38	0	0.5	5481
	Uncoded Golay	40	2	2.5	5431
	LDPC(336,672)	39	-7	1.5	2740
	LDPC(504,672)	38	-4.5	0.5	4111
	RS(224,216)	23	-1.5	-14.5	3523
64 QAM	Uncoded Ideal	38	N/A	N/A	10997
	Uncoded Pilot	38.5	0	0.5	10963
	LDPC(336,672)	40	-1.5	2	5481
	LDPC(504,672)	43	0	5	8222
	RS(224,216)	25	-0.5	-13	7047

Finally in Figure 5.25 and Table 5.12 the results for LOS kiosk environment (CM9) are drawn. It is clear that the performance of this channel is much better then the channel models presented previously. It happens because LOS is considered at very short distance (Section 5.2.1).

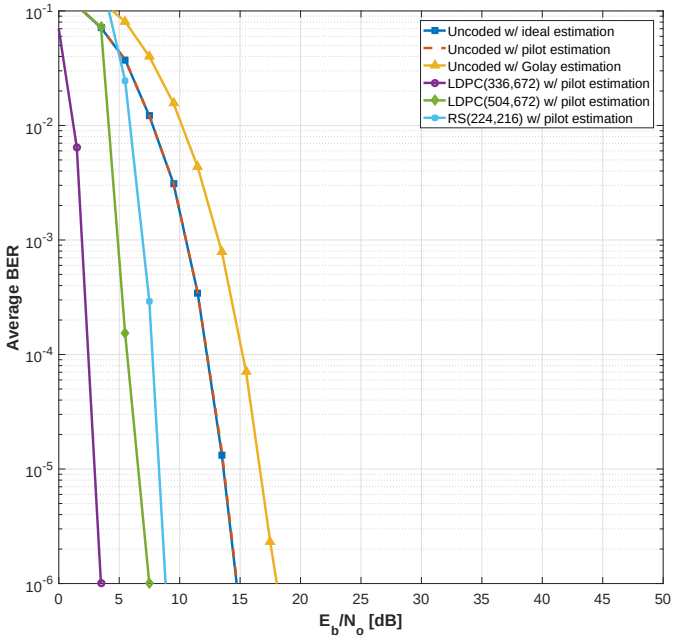

(a)

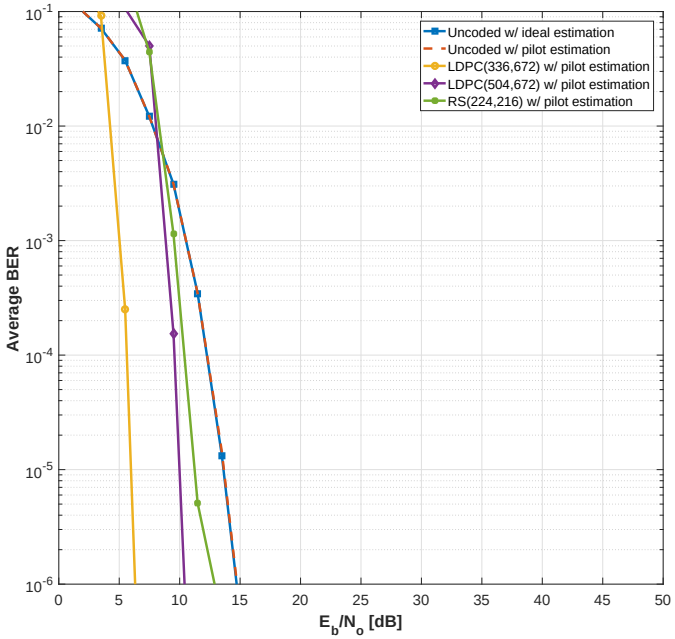

(b)

Figure 5.25: BER results for LOS kiosk channel mode CM9, considering EIRP = 40 dBm for (a) 16 QAM and (b) 64 QAM.

Analyzing BER curves, it is seen that the BER results for different FEC codes do not overlap as happened in the previous channel models. Note that results are in accordance with the ones obtained in Section 4.9 since LDPC(336,672) appears as the best FEC code, before LDPC(504,672) and RS(224,216).

From Table 5.12 can be seen that for CM9 it is possible to obtain a probability of one error in one million transmitted bits ensuring a E_b/N_0 of only 14.5 dB.

Table 5.12: Simulation results for LOS kiosk channel mode CM9 for EIRP = 40 dBm.

Modulation	Parametrization	E_b/N_0 (dB)	$\Delta E_b/N_0$ (dB) @BER=10^{-3}	$\Delta E_b/N_0$ (dB) @BER=10^{-6}	Throughput (Mbps)
16 QAM	Uncoded Ideal	14.5	N/A	N/A	6453
	Uncoded Pilot	14.5	0	0	6433
	Uncoded Golay	18	2.5	-3.5	6374
	LDPC(336,672)	3	-8.5	-11.5	3216
	LDPC(504,672)	7.5	-6	-7	4825
	RS(224,216)	9	-4.5	-5.5	4135
64 QAM	Uncoded Ideal	15	N/A	N/A	12907
	Uncoded Pilot	15	45.45	0	12867
	LDPC(336,672)	6	-5	-9	6433
	LDPC(504,672)	10.5	-2	-4.5	9650
	RS(224,216)	14	-1	-1	8271

Another important conclusion is that since CM9 has a relatively short cyclic prefix (24.24 ns) an higher throughput is achieved when comparing with CM1 and CM2. Therefore the simulation results says that the throughput can vary from 6.43 Gbps up to 12.87 Gbps for uncoded transmission and from 4.14 Gbps up to 9.65 Gbps considering FEC codes.

5.6 Uncompressed video transmission

In this section, uncoded OFDM system performance over the proposed multigigabit framework at 60 GHz is assessed transmitting Full HD uncompressed video [81]. Both 16 and 64 QAM modulation schemes are considered. The quality of the transmitted uncompressed video content is assessed through operation range and PSNR analysis. In addition, it is possible to estimate the minimum value of E_b/N_o to ensure a relatively satisfactory subjective quality of the video frame depicted in Figure 5.26 used for this purpose. This is achieved by using the relation between the PSNR (objective quality

assessment metric) and the subjective quality assessment based on viewer's impression, presented in Table 5.13 [82].

Table 5.13: Relation between subjective and objective quality indicators.

PSNR [dB]	**ITU Quality scale**
> 37	5 - Excellent
$31 - 37$	4 - Good
$25 - 31$	3 - Satisfactory
$20 - 35$	2 - Poor
< 20	1 - Very poor

Figure 5.26: Reference frame from the Full HD Cactus.yuv video sequence for the PSNR calculation.

5.6.1 Uncoded transmission

To estimate the minimum distance between the TX and RX in this particularly application, several parameters presented in (5.2) must be known. For example, when no human blockage is considered, link margin is equal to the shadowing margin, but when it is presented additional losses must be taken into account. According to [83], the losses caused by a person moving and crossing the propagation path varies from 18-36 dB, at 60 GHz in indoor environments. Considering this, the maximum operating range vs E_b/N_o for uncoded OFDM over the considered multipath fading channels when either absence or presence of human shadowing is presented, is given in Figure 5.27.

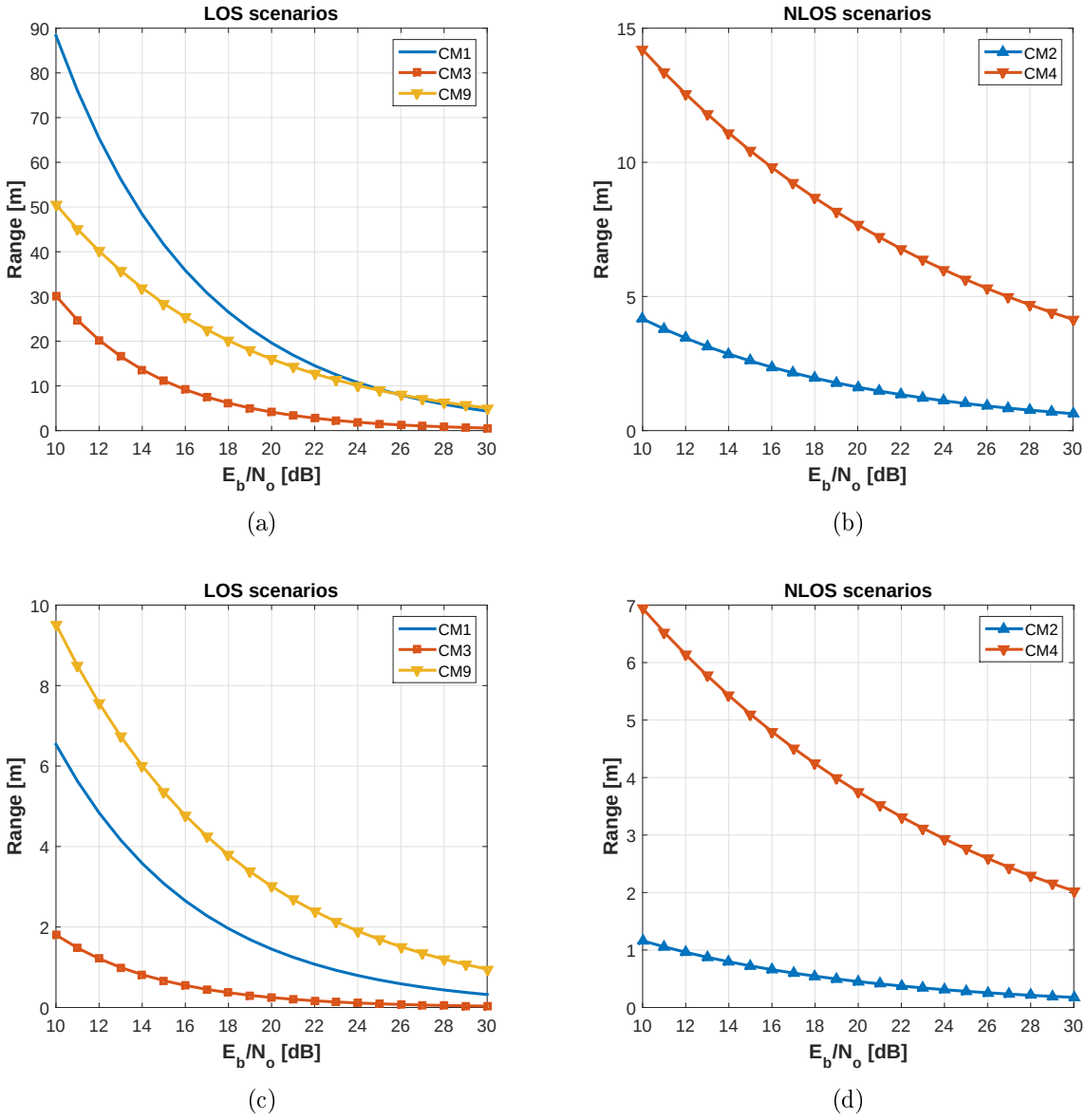

Figure 5.27: Estimated maximum operating range for uncoded OFDM versus E_b/N_o for each channel model: (a) and (b) without human shadowing; (c) and (d) with human blockage.

In order to evaluate the effectiveness of uncoded OFDM for a relatively good Quality of Service (QoS) at appropriate E_b/N_o values, the degradation of the quality of the video frame for CM9 has been studied. The video frame content (Figure 5.26) is divided into several transmitting OFDM symbols and then transmitted over the channel model. PSNR results are depicted in Figure 5.28 using 16 QAM and 64 QAM modulation and considering both AWGN channel and CM9. It be can seen that the effect of CM9 model have not significant impact on the degradation of the quality of reference video frame, with the maximum achievable PSNR of about 60 dB (for a $E_b/N_o = 13$ dB). This characterizes the video frame subjective quality as excellent (Table 5.13), with a

maximum distance between both TX and RX antennas of 34 m and 7 m, for absence and presence of human obstacles in the link, respectively.

(a)

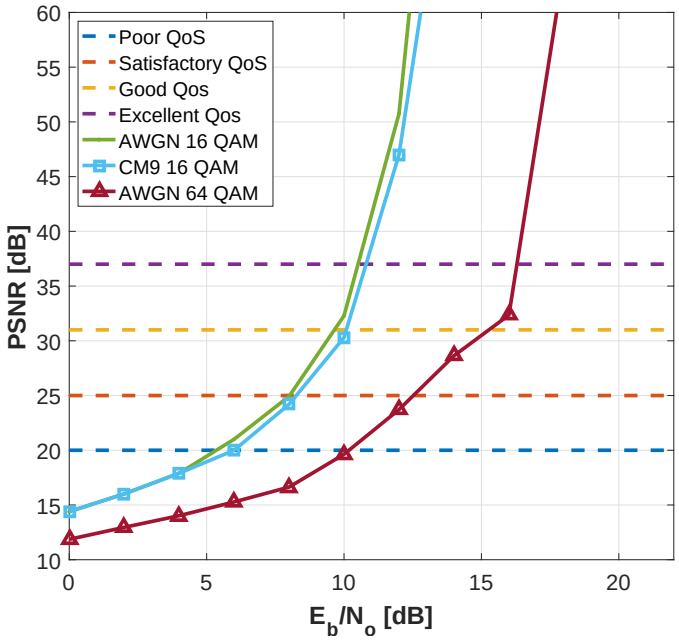

(b)

Figure 5.28: Video quality performance of the received frame transmitted: a) subject video frame quality at PSNR of 14.01 dB b) objective video frame quality vs E_b/N_o.

5.6.2 Coded transmission

In this subsection, similar analysis presented in 5.6.1, are conducted. The maximum operating range vs E_b/N_o for coded OFDM (Figure 5.29) over the considered multi-path fading channels is calculated considering the same parameters, except the system throughput, which varies according to Table 5.14. In addition, in this table is also detailed the type and coding rate of each employed FEC codes.

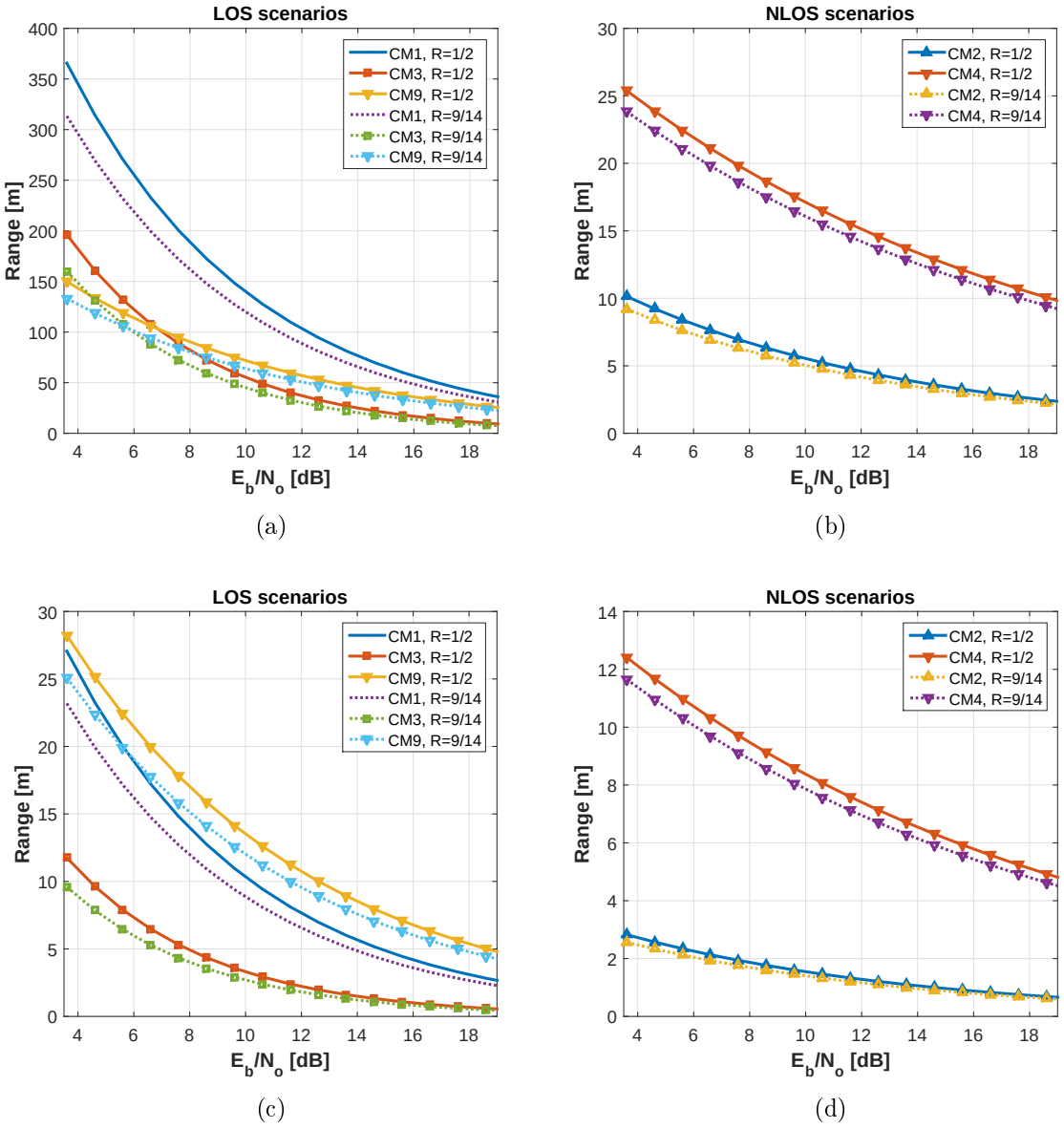

Figure 5.29: Estimated maximum operating range for uncoded OFDM versus E_b/N_o for each channel model: (a) and (b) without human shadowing; (c) and (d) with human blockage.

Table 5.14: Summary of the OFDM FEC schemes.

FEC	**Overall code rate**	**Throughput [Gbps]**
RS (224,216)	9/14	3.96
LDPC (672,336)	1/2	3.08

As shown in 5.4, the use of FEC codes enables the communication at very low

Signal-to-Noise Ratios (SNRs). BER target is achieved for E_b/N_o values of 10 dB and 3.6 dB for RS and LDPC coding, respectively. This allows the TX and RX to be antennas to be apart of 150 m and 28.2 m (this one in the presence of human shadowing) considering a coding rate of 1/2. Similarly, when a coding rate of 9/14 is used, both distances are 133.2 m and 25 m, which means that channel coding make the system more robust against noise and thus its operating range is significantly increased. For example, when LDPC coding is employed this distance increases 121.5 m and 22.8 m, for absence and presence of disturbances in the transmission medium, relatively to the uncoded OFDM system.

5.7 Summary

The fifth chapter reports the performance evaluation of the proposed framework over indoor multipath fading channels and considering the IEEE 802.15.3c standard as reference. First, the study scenarios for the performance assessment are presented. It is considered the indoor environments suggested by TG3c group and the corresponding link budget and mobility considerations. The performance assessment is divided in two main groups: uncoded OFDM system assessment and coded OFDM system assessment. In the first group, a parametric study is reported in order to find the most suitable cyclic prefix length for each channel model. Then, the performance results based on channel estimation using pilot subcarriers and Golay sequences are presented. The second group shows the simulation results of a transmission employing FEC codes. The chapter ends with a comparative analysis of the main results obtained previously.

Chapter 6

Conclusions

6.1 Summary

Chapter 2 presented a review of the main contributions in the literature referring multigigabit prototyping testbeds addressed to 5 G requirements. After a quick description of each project, Table 2.1 compiles the main characteristics of each testbed. the high spectral efficiency is transversal to almost every project since MIMO techniques are used. Among with the presented testbeds, spectral efficiencies of 67.26 and 145.6 bit/s/Hz can be obtained. Despite the good performance in terms of spectral efficiency, non of the projects is implemented in 60 GHz band, which could be even more profitable, due to high bandwidth available. In this Chapter, a overview of two standards operating at 60 GHz is conducted, IEEE 802.11ad and IEEE 802.15.3c. These standards define several PHY layer modes in order to meet with different requirements. Since IEEE 802.15.3c was the first standard addressing multigigabit data rates at 60 GHz, it is the standard taken as reference in the work.

In Chapter 3, the theoretical fundamentals for the work are presented. First, a detailed description of a OFDM system is conducted, as well as the analytic expressions related to it. Next, the concepts related to multipath fading channels are introduced. The fading channel is subdivided in large-scale fading effects and small-scale fading effects and the parameters used to characterize these two categories of fading channel response are detailed. In this Chapter the most commonly used channel coding approaches are presented and the theoretical aspects of channel estimation based on both pilot subcarriers and Golay sequences and frequency domain equalization are discussed.

Chapter 4 aims to present the proposed simulation framework for multigigabit ap-

plications. Initially, the general block diagram of the framework is shown and the overall operation is discussed. Then, each block of general block diagram is detailed. This Chapter also addresses the performance evaluation metric considered for the work. Finally, simulation results are conducted in order to validate the simulation framework.

Chapter 5 refers to performance evaluation of 60 GHz OFDM framework over indoor multipath fading channels. The indoor multipath fading channels are obtained and characterized according to the suggestions of TG3c group. After defining the channel models considered for the performance evaluation, the framework is loaded with the parameters of IEEE 802.15.3c. The performance assessment is divided in two main groups: uncoded OFDM system assessment and coded OFDM system assessment. The chapter ends with a comparative analysis of the main results obtained previously from both uncoded and coded OFDM system assessments.

6.2 Main conclusions

This work presents a simulation framework for multigigabit applications based on OFDM modulation at mmWave frequencies. The main goal of the framework is to provide a modular simulation tool designed for high data rate application in order to be easily adapted to a specific standard or technology, such as 5G. The presented framework allows the employment of 16 QAM or 64 QAM modulation scheme, and the length of the cyclic prefix extension is also configurable. In order to simulate a realistic multipath fading channel, the proposed framework allows the insertion of a channel impulse response defined by the user. The channel estimation can be performed either using pilot subcarriers or Golay sequence as channel estimation sequences. Independently of the channel estimation technique selected, frequency domain equalization is available through ZF approach or MMSE. The simulation framework also allows channel coding techniques in order to provide a more robustness transmission and to improve the link budget.

The performance assessment of the framework is based on IEEE 802.15.3c. From the analysis of the performance indicators returned from the simulation framework, it was concluded that the transmitted symbols were being affected by ISI, which means that the cyclic prefix suggested by the standard is not suitable for the channel models considered. Thus, a parametric study was conducted in order to find the CP length that reduce ISI effect but does not compromise the spectral efficiency of the system. It was defined that a $T_{CP} = \tau_{max}$ is a good approach. Therefore, further simulations

considers the T_{CP} proposed in the parametric study. Other simulations showed that the pilot arrangement suggested by IEEE 802.15.3c does not provide the desired performance since the channel models considered are highly frequency selective. Thus, it was suggested the implementation of a block type pilot arrangement where the pilot symbol transmission period is dependent on the coherence time of the channel.

In terms of comparative analysis of the different channel estimation approaches, it is seen that pilot-based channel estimation in block type arrangement outperforms Golay sequences transmission in terms of BER performance and throughput. It can also be concluded that concatenated codes outperforms LDPC codes for high BER levels, which does not happen for BER values of approximately 10^{-3}. From these analysis it is concluded that for uncoded transmissions, pilot-based is the most suitable approach for channel estimation purposes and for coded transmissions, concatenated codes, composed by Reed Solomon and convolutional codes, are suggested.

6.3 Further work

In this work, the implementation of a simulation framework for multigigabit applications at mmWave frequencies is proposed and described. Nevertheless, there are still some topics that require further investigation work. Next, those topics are described

- **Extension of the simulation framework in order to include RF impairments**. As refereed in Section 4.2, the performance of OFDM at mmWave is severely affected by non-linearities of RF front-end. Thus, in order to compensate these non-linearities, RF impairments, such as phase-noise, mixer IQ imbalances, and power amplifier non-linearities must be considered in the simulation framework.

- **Integration of the 5G PHY layer requirements in the framework**. Due to the scalability of the framework, once defined the standard responsible for supporting 5G mobile communications, it will be possible to integrate the PHY layer requirements in the proposed framework. It will be possible then, to rapidly test and validate new techniques and/or methods.

- **Hardware Prototyping of end-to-end multigigabit OFDM based for 5G communications**. Having a simulation platform able to test and evaluate new techniques for the development of 5G communications, the implementation of a

prototyping testbed addressing 5G becomes easier. Thus, for future work, the implementation of a end-to-end multigigabit platform at mmWave is proposed. This project could be divided in two stages, first the implementation of a SISO system, and after proving their validation, improve the system in order to provide MIMO transmission. In Figure 6.1, a generic block diagram of 2×2 MIMO at 60 GHz is illustrated. The components shown in this Figure represents the hardware already available in the research research group of Antennas and Propagation from the Instituto de Telecomunicações de Leiria, where the author is inserted.

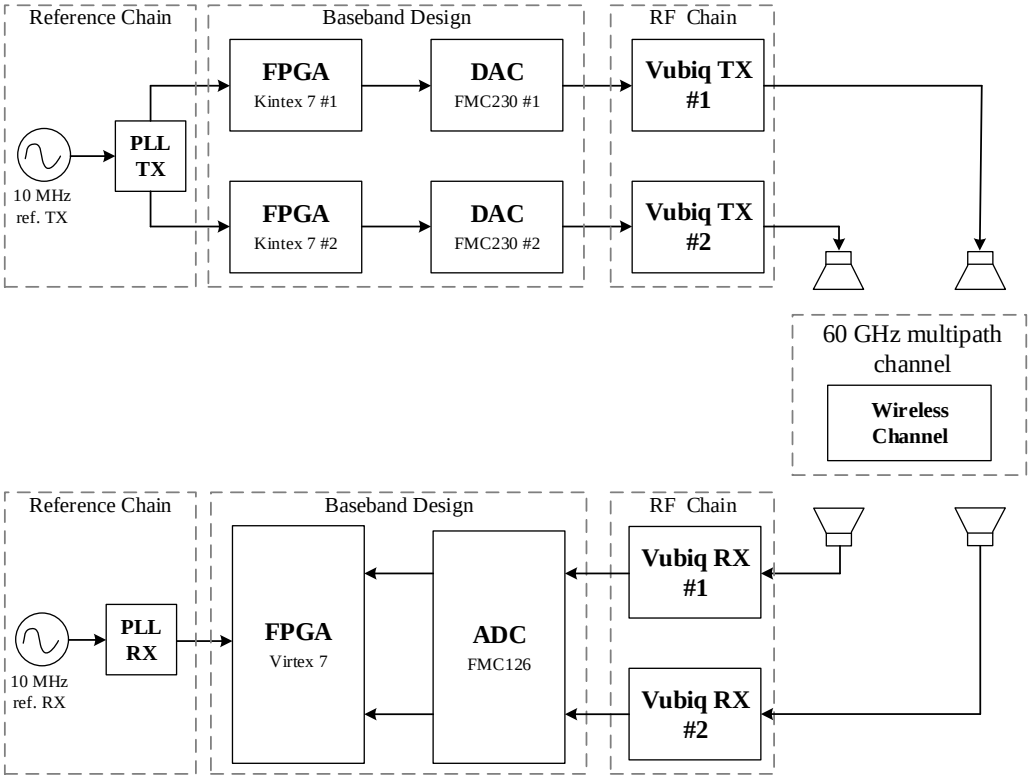

Figure 6.1: 2×2 MIMO mmWave wireless radio system prototype for multigigabit applications.

Bibliography

[1] S.-K. Yong, P. Xia, and A. Valdes-Garcia, *60 GHz TECHNOLOGY FOR GBPS WLAN AND WPAN*. WILEY, 2011.

[2] *802.15.3c-2009 - Physical Layer (PHY) Specifications for High Rate Wireless Personal Area Networks (WPANs) (IEEE 802.15.3c)*.

[3] T. Nitsche, C. Cordeiro, A. B. Flores, E. W. Knightly, E. Perahia, and J. C. Widmer, "IEEE 802.11ad: directional 60 GHz communication for multi-Gigabit-per-second Wi-Fi [Invited Paper]," *IEEE Communications Magazine*, vol. 52, pp. 132–141, December 2014.

[4] A. Younis, N. Abuzgaia, R. Mesleh, and H. Haas, "Quadrature Spatial Modulation for 5G Outdoor Millimeter-Wave Communications: Capacity Analysis," *IEEE Transactions on Wireless Communications*, vol. PP, no. 99, pp. 1–1, 2017.

[5] A. S. Marcano and H. L. Christiansen, "Performance of Non-Orthogonal Multiple Access (NOMA) in mmWave wireless communications for 5G networks," in *2017 International Conference on Computing, Networking and Communications (ICNC)*, pp. 969–974, Jan 2017.

[6] R. V. Nee and R. Prasad, *OFDM for Wireless Communications*. Artech House Publishers, 1999.

[7] M. Lei and Y. Huang, "CFR and SNR Estimation Based on Complementary Golay Sequences for Single-Carrier Block Transmission in 60-GHz WPAN," in *IEEE Wireless Communications and Networking Conference, 2009. WCNC 2009*, pp. 1–5, Apr. 2009.

[8] P. Kumari, N. Gonzalez-Prelcic, and R. W. Heath, "Investigating the IEEE 802.11ad Standard for Millimeter Wave Automotive Radar," in *Vehicular Technology Conference (VTC Fall), 2015 IEEE 82nd*, pp. 1–5, Sept 2015.

[9] W. C. Liu, F. C. Yeh, T. C. Wei, C. D. Chan, and S. J. Jou, "A Digital Golay-MPIC Time Domain Equalizer for SC/OFDM Dual-Modes at 60 GHz Band," *IEEE Transactions on Circuits and Systems I: Regular Papers*, vol. 60, pp. 2730–2739, Oct 2013.

[10] W. C. Liu, T. C. Wei, Y. S. Huang, C. D. Chan, and S. J. Jou, "All-Digital Synchronization for SC/OFDM Mode of IEEE 802.15.3c and IEEE 802.11ad," *IEEE Transactions on Circuits and Systems I: Regular Papers*, vol. 62, pp. 545–553, Feb 2015.

[11] C. F. Wu, W. C. Liu, C. C. Tsui, C. Y. Liu, M. S. Sie, and S. J. Jou, "Golay-Correlator Window-Based Noise Cancellation Equalization Technique for 60-GHz Wireless OFDM/SC Receiver," *IEEE Transactions on Very Large Scale Integration (VLSI) Systems*, vol. PP, no. 99, pp. 1–11, 2016.

[12] L. Chen, G. Yue, X. Cheng, and S. Li, "Time-domain frequency-dependent I/Q imbalance compensation based on golay sequence," in *2014 IEEE 11th Consumer Communications and Networking Conference (CCNC)*, pp. 531–536, Jan 2014.

[13] A. E. Assaf, N. Kandil, N. Hakem, S. Affes, and P. Fortier, "A study of 60 GHz channel estimation techniques using pilot carriers in OFDM systems in a confined area," in *Wireless Communications in Unusual and Confined Areas (ICWCUCA), 2012 International Conference on*, pp. 1–6, Aug 2012.

[14] B. Ye and Z. Zhang, "Improved pilot design and channel estimation for 60GHz OFDM based on IEEE 802.11.ad," in *2013 IEEE Wireless Communications and Networking Conference (WCNC)*, pp. 4129–4133, April 2013.

[15] M. K. Ozdemir and H. Arslan, "Channel Estimation for Wireless OFDM Systems," *IEEE Communications Surveys Tutorials*, vol. 9, pp. 18–48, Second 2007.

[16] L. Li, R. C. de Lamare, and A. G. Burr, "Dynamic pilot allocation with channel estimation in closed-loop multi-input-multi-output orthogonal frequency division multiplexing systems," *IET Communications*, vol. 8, pp. 2017–2025, July 2014.

[17] P. Pakrooh, A. Amini, and F. Marvasti, "OFDM pilot allocation for sparse channel estimation," *CoRR*, vol. abs/1106.4507, 2011.

[18] W. S. H. Z. X. W. J. W. H. Zhang, "Research on Channel Estimation Algorithm in 60GHz System Based on 802.15.3c Standard," *Journal of Communications*, vol. 9, 2014.

[19] J. C. Guey and A. Osseiran, "Adaptive Pilot Allocation in Downlink OFDM," in *2008 IEEE Wireless Communications and Networking Conference*, pp. 840–845, March 2008.

[20] L. U. Khan, S. A. Mahmud, G. M. Khan, M. H. Zafar, and M. Ashraf, "Channel estimation based on Non-Equally Spaced Pilot allocation in OFDM system,"

in *Computer Science and Electronic Engineering Conference (CEEC), 2014 6th*, pp. 139–143, Sept 2014.

[21] B. Rajarshi Banerjee and T. Rao, "Pilot Design based Channel Estimation for IEEE 802.11ad Wireless Communications at 60 GHz," in *International Conference on Signal Processing, Embedded System and Communication Technologies and their applications for Sustainable and Renewable Energy (ICSECSRE), 2014*, pp. 385–391, April 2014.

[22] Su-Khiong Yong, *TG3c Channel Modeling Sub-committee Final Report*. Samsung Advanced Institute of Technology, Mar. 2007.

[23] 5GNOW, "5GNOW: 5th Generation Non-Orthogonal Waveforms for Asynchronous Signalling."

[24] I. T. U. (ITU), "Minimum requirements related to technical performance for IMT-2020 radio interface(s)."

[25] M. Schellmann, Z. Zhao, H. Lin, P. Siohan, N. Rajatheva, V. Luecken, and A. Ishaque, "FBMC-based air interface for 5G mobile: Challenges and proposed solutions," in *2014 9th International Conference on Cognitive Radio Oriented Wireless Networks and Communications (CROWNCOM)*, pp. 102–107, June 2014.

[26] P. Guan, D. Wu, T. Tian, J. Zhou, X. Zhang, L. Gu, A. Benjebbour, M. Iwabuchi, and Y. Kishiyama, "5G Field Trials - OFDM-based Waveforms and Mixed Numerologies," *IEEE Journal on Selected Areas in Communications*, vol. PP, no. 99, pp. 1–1, 2017.

[27] R. MÃ©ndez-Rial, C. Rusu, N. GonzÃ¡lez-Prelcic, A. Alkhateeb, and R. W. Heath, "Hybrid MIMO Architectures for Millimeter Wave Communications: Phase Shifters or Switches?," *IEEE Access*, vol. 4, pp. 247–267, 2016.

[28] T. E. Bogale and L. B. Le, "Beamforming for multiuser massive MIMO systems: Digital versus hybrid analog-digital," in *2014 IEEE Global Communications Conference*, pp. 4066–4071, Dec 2014.

[29] C. Shepard, H. Yu, N. Anand, L. E. Li, T. Marzetta, R. Yang, and L. Zhong, "Argos: Practical Many-Antenna Base Stations," in *MobiCom 12*, Aug 2012.

[30] H. Y. Clayton Shepard and L. Zhong, "ArgosV2: A Flexible Many-Antenna Research Platform," in *MobiCom 13*, Sept 2013.

[31] WARP, "WARP: Wireless Open Access Research Platform."

[32] J. Vieira, S. Malkowsky, K. Nieman, Z. Miers, N. Kundargi, L. Liu, I. Wong, V. Owall, O. Edfors, and F. Tufvesson, "A flexible 100-antenna testbed for Massive MIMO," in *2014 IEEE Globecom Workshops (GC Wkshps)*, pp. 287–293, Dec 2014.

[33] H. Suzuki, R. Kendall, K. Anderson, A. Grancea, D. Humphrey, J. Pathikulangara, K. Bengston, J. Matthews, and C. Russell, "Highly spectrally efficient Ngara Rural Wireless Broadband Access Demonstrator," in *2012 International Symposium on Communications and Information Technologies (ISCIT)*, pp. 914–919, Oct 2012.

[34] W. Zhang, J. Xiang, Y. N. R. Li, Y. Wang, Y. Chen, P. Geng, and Z. Lu, "Field trial and future enhancements for TDD massive MIMO networks," in *2015 IEEE 26th Annual International Symposium on Personal, Indoor, and Mobile Radio Communications (PIMRC)*, pp. 2339–2343, Aug 2015.

[35] Samsung, "Samsung takes first 5g steps with advanced antenna."

[36] P. Harris, W. B. Hasan, S. Malkowsky, J. Vieira, S. Zhang, M. Beach, L. Liu, E. Mellios, A. Nix, S. Armour, A. Doufexi, K. Nieman, and N. Kundargi, "Serving 22 Users in Real-Time with a 128-Antenna Massive MIMO Testbed," in *2016 IEEE International Workshop on Signal Processing Systems (SiPS)*, pp. 266–272, Oct 2016.

[37] University of Bristol, "Communication Systems and Networks Research Group."

[38] A. Tecnhologies, "Wireless LAN at 60 GHz - IEEE 802.11ad Explained," *IEEE Communications Magazine*, May 2013.

[39] A. Sadri, *Summary of the Usage Models for 802.15.3c.* IEEE 802.15-06-0369-09-003c, 2006.

[40] S.-K. Yong, *TG3c Channel Modeling Sub-committee Final Report.* IEEE 802.15-07-0584-01-003c, 2007.

[41] Z. L. J. W. M. A. R. Tuncer Baykas, Chin-Sean Sum and H. Harada, *IEEE 802.15.3c: The First IEEE Wireless Standard for Data Rates over 1 Gb/s.* IEEE Communications Magazine, 2011.

[42] A. F.Molisch, *Wireless Communications.* WILEY, 2011.

[43] W. Yong Soo Cho, Jaekwon Kim and Chung G. Kang, *MIMO-OFDM Wireless Communications with MATLAB.* Wiley.

[44] C. L. Henrik Schulze, *Theory and Applications of OFDM and CDMA.* WILEY.

[45] T. S. Rappaport, *Wireless Communications: Principles and Practice.* Prentice Hall, 2 edition ed., Jan. 2002.

[46] B. Sklar, *Digital Communications: Fundamentaals and Applications.* Prentice Hall, 2 edition ed., 2002.

[47] H. Abdulkarim, "Comparison of Proposals for the Future Aeronautical Communication System LDACS."

[48] C. Anderson and T. Rapapport, "In-building wideband partition loss measurements at 2.5 and 60 GHz," *IEEE transactions on Wireless Communications*, vol. 3, pp. 922–928, 2004.

[49] H. Harada, R. Funada, H. Sawada, and S. Kato, *CM MATLAB Release Support Document.* Mar. 2007.

[50] P. F. M. Smulders, "Statistical Characterization of 60-GHz Indoor Radio Channels," 2009.

[51] A. Saleh and R. Valenzuela, "A Statistical Model for Indoor Multipath Propagation," *IEEE Journal on Selected Areas in Communications*, vol. 5, pp. 128–137, Feb. 1987.

[52] Q. Spencer, B. Jeffs, M. Jensen, and A. Swindlehurst, "Modeling the statistical time and angle of arrival characteristics of an indoor multipath channel," *IEEE Journal on Selected Areas in Communications*, vol. 18, pp. 347–360, Mar. 2000.

[53] J. G. Proakis and M. Salehi, *Digital Communications.* McGraw-Hill, 5 edition ed., 2008.

[54] A. Khlifi and R. Bouallegue, "Performance Analysis of LS and LMMSE Channel Estimation Techniques for LTE Downlink Systems," vol. 58, no. 5, pp. 141–149, 2011.

[55] B. Ye and Z. Zhang, "Improved pilot design and channel estimation for 60GHz OFDM based on IEEE 802.11.ad," in *2013 IEEE Wireless Communications and Networking Conference (WCNC)*, pp. 4129–4133, April 2013.

[56] L. Kewen and XingKe, "Research of MMSE and LS channel estimation in OFDM systems," in *The 2nd International Conference on Information Science and Engineering*, pp. 2308–2311, Dec 2010.

[57] S. Coleri, M. Ergen, A. Puri, and A. Bahai, "Channel estimation techniques based on pilot arrangement in OFDM systems," *IEEE Transactions on Broadcasting*, vol. 48, pp. 223–229, Sep 2002.

[58] F. Wang, "Pilot-based channel estimation in OFDM system."

[59] M. Golay, "Complementary series," *IRE Transactions on Information Theory*, vol. 7, pp. 82–87, April 1961.

[60] B. M. Popovic, "Efficient Golay correlator," *IEE Electron. Lett*, vol. 35, pp. 1427–1428, Aug 1999.

[61] M. Lei, I. Lakkis, H. Harada, and S. Kato, "MMSE-FDE Based on Estimated SNR for Single-Carrier Block Transmission (SCBT) in Multi-Gbps WPAN (IEEE 802.15.3c)," in *IEEE International Conference on Communications Workshops, 2008. ICC Workshops '08*, pp. 52–56, May 2008.

[62] MathWorks, "Simulink."

[63] MathWorks, "DSP System Toolbox."

[64] MathWorks, "Sample- and Frame-Based Concepts."

[65] R. Kimura, R. Funada, Y. Nishiguchi, M. Lei, T. Baykas, C. S. Sum, J. Wang, A. Rahman, Y. Shoji, H. Harada, and S. Kato, "Golay sequence aided channel estimation for millimeter-wave WPAN systems," in *2008 IEEE 19th International Symposium on Personal, Indoor and Mobile Radio Communications*, pp. 1–5, Sept 2008.

[66] N. Instruments, "Peak Signal-to-Noise Ratio as an Image Quality Metric."

[67] C. Shannon, "A mathematical theory of communication," *Bell System Technical Journal, The*, vol. 27, pp. 379–423, July 1948.

[68] N. Bonello, S. Chen, and L. Hanzo, "Design of low-density parity-check codes: An overview," *IEEE VechicularTechnology Magazine*, vol. 6, pp. 16–23, Dec. 2011.

[69] H. Harada, R. Funada, H. Sawada, and S. Kato, *CM MATLAB Release Support Document*. Mar. 2007.

[70] *NICT Propagation Data*, (Hawaii, USA), 2006.

[71] . P. F. M. Smulders, "Broadband Wireless LANs: A Feasibility Study," *Ph.D. Thesis, Eindhoven University*, 1995.

[72] K. K. J. B. J. HÃ$\frac{1}{4}$bner, S. Zeisberg and A. Finger, "Simple Channel Model for 60 GHz Indoor Wireless LAN Design Based on Complex Wideband Measurements," *IEEE VTC 05*, vol. 2, pp. 1004–1008, 1997.

[73] *LOS office channel model based on TSV model*, (Melbourne, Australia), 2006.

[74] *Office 60 GHz Channel Measurements and Model*, (San Diego, USA), 2006.

[75] *A new LOS kiosk channel model based on TSV model*, (Orlando, USA), 2007.

[76] *CM MATLAB Release 1.1 Support Document*, (London, UK), 2007.

[77] *Channel Model Matlab Code Release*, (Orlando, USA), 2007.

[78] R. Daniels, J. Murdock, T. Rappaport, and R. Heath, "60 GHz Wireless: Up Close and Personal," *IEEE Microwave Magazine*, vol. 11, pp. 44–50, Dec. 2010.

[79] S. Alireza and Philips, *TG3C Selection Criteria*. Jan. 2007.

[80] T. Baykas, M. Lei, C.-S. Sum, R. Funada, Y. Nishiguchi, and R. Kimura, "Operation Range Estimation of Reed-Solomon Coded SC-FDE System in 60-GHz WPANs," in *10th International Conference on Advanced Communication Technology, 2008. ICACT 2008*, vol. 1, pp. 167–170, Feb. 2008.

[81] A. H. Rodolfo Gomes, Rafael Caldeirinha and P. Pires, "Performance Evaluation of 60 GHz OFDM Communications under Channel Impairments over Multipath Fading Channels at 60 GHz ," *Sensors & Transducers*, vol. 204, pp. 29–38, Sept. 2016.

[82] H. K. Kim, S.-I. Ao, and B. B. Rieger, *IAENG Transactions on Engineering Technologies: Special Edition of the World Congress on Engineering and Computer Science 2011*. Springer Science & Business Media, Sept. 2012.

[83] P. Gallo, S. Loi, and P. Priotti, "Transmission Range Analysis of IEEE 802.15.3c Technology in Residential Environments," in *Telecommunications: The Infrastructure for the 21st Century (WTC), 2010*, pp. 1–6, Sept. 2010.

Appendix A

IEEE 802.15.3c: SC PHY parameters

A.1 MCS dependent parameters

MCS class	MCS identifier	Data rate (Mb/s) with pilot word length = 0	Data rate (Mb/s) with pilot word length = 64	Modulation	Spreading factor, L_{SF}	FEC type
Class1	0	25.8 (CMS)	—	π/2 BPSK/(G)MSK[a]	64	RS(255,239)
	1	412	361		4	
	2	825	722		2	
	3	1650 (MPR)	1440		1	
	4	1320	1160	π/2 BPSK/(G)MSK	1	LDPC(672,504)
	5	440	385	π/2 BPSK/(G)MSK	2	LDPC(672,336)
	6	880	770		1	
Class2	7	1760	1540	π/2 QPSK	1	LDPC(672,336)
	8	2640	2310	π/2 QPSK	1	LDPC(672,504)
	9	3080	2700	π/2 QPSK	1	LDPC(672,588)
	10	3290	2870	π/2 QPSK	1	LDPC(1440,1344)
	11	3300	2890	π/2 QPSK	1	RS(255,239)
Class3	12	3960	3470	π/2 8-PSK	1	LDPC(672,504)
	13	5280	4620	π/2 16-QAM	1	LDPC(672,504)

Figure A.1: MCS dependent parameters of SC PHY [2].

A.2 Timing-related parameters

Parameter	Description	Value			Unit	Formula
R_c	Chip rate	1760			Mchip/s	
T_c	Chip duration	~0.568			ns	$1/R_c$
$L_{subblock}$	Subblock length	512			chips	
L_{PW}	Pilot word length	0	8[a]	64	chips	
T_{PW}	Pilot word duration	0	4.5	~37.0	ns	
L_{DC}	Length of data chips per subblock	512	56	448	chips	
$T_{subblock}$	Subblock duration	~290.9			ns	$L_{subblock} \times T_c$
$R_{subblock}$	Subblock rate	~3.44			MHz	$1/T_{subblock}$

Figure A.2: Timing-related parameters of SC PHY [2].

A.3 Frame-related parameters

Parameter	Description	Value
N_{SYNC}	Number of code repetitions[a] in the SYNC sequence	14
T_{SYNC}	Duration of the SYNC sequence	~1 µs
N_{SFD}	Number of code repetitions in the SFD	4
T_{SFD}	Duration of the SFD	~0.29 µs
N_{CES}	Number of code repetitions in the CES	9
T_{CES}	Duration of the CES	~0.65 µs
N_{pre}	Number of code repetitions in the PHY preamble	27
T_{pre}	Duration of the PHY preamble	~1.96 µs
L_{hdr}	Length of the base header in octets	33
$N_{subblock\_hdr}$	Number of subblocks in the base frame header	$CEIL[L_{hdr} \times 8 \times L_{SF} / (L_{subblock} - L_{PW}{}^{b})]$
T_{hdr}	Duration of the base frame header	$N_{subblock\_hdr} \times T_{subblock}$
$L_{payload}$	Length of frame payload in octets	variable
L_{FCS}	Length of FCS in octets	4
L_{MFB}	Length of the MAC frame body in octets	$L_{payload} + L_{FCS}$
N_{PCES}	Number of code repetitions in the PCES	9
T_{PCES}	PCES duration	0.65 µs
N_{PCES_frame}	Number of PCESs per frame	$CEIL[(L_{MFB} \times 8) / (L_{subblock} \times 64)]–1$
$T_{PCES\_interval}$	Interval of PCES insertion	$T_{subblock} \times 64 + T_{PW}$
L_{CBPS}	Number of coded bits per subblock in the MAC frame body	$(L_{subblock} - L_{PW}{}^{c}) / L_{SF}$
$N_{subblock\_MFB}$	Number of subblocks in the MAC frame body	$CEIL[(L_{MFB} \times 8) / (R_{FEC} \times L_{CBPS})]$
T_{MFB}	Duration of the MAC frame body	$N_{subblock\_MFB} \times T_{subblock}$
$T_{datafield}$	Duration of the PHY Payload field	$T_{MFB} + (N_{PCES\_frame} + 1) \times T_{PW} + N_{PCES\_frame} \times T_{PCES}$
T_{frame}	Duration of the frame	$T_{pre} + T_{hdr} + T_{datafield}$

Figure A.3: Frame-related parameters of SC PHY [2].

A.4 LDPC code matrix permutation indexes

(672,336), Code rate: 1/2

	1	2	3	4	5	6	7	8	9	10	11	12	13	14	15	16	17	18	19	20	21	22	23	24	25	26	27	28	29	30	31	32
1	-	-	-	5	-	18	-	-	-	-	3	-	10	-	-	-	-	-	-	5	-	-	-	-	-	-	-	5	-	7	-	-
2	0	-	-	-	-	-	16	-	-	-	-	6	-	-	-	0	-	7	-	-	-	-	-	-	-	10	-	-	-	-	-	19
3	-	-	6	-	7	-	-	-	-	2	-	-	-	-	9	-	20	-	-	-	-	-	-	-	-	-	19	-	10	-	-	-
4	-	18	-	-	-	-	-	0	10	-	-	-	-	16	-	-	-	-	9	-	-	-	-	-	4	-	-	-	-	-	17	-
5	5	-	-	-	-	-	18	-	-	-	-	3	-	10	-	-	5	-	-	-	-	-	-	-	-	-	-	-	-	7	-
6	-	0	-	-	-	-	-	16	6	-	-	-	0	-	-	-	-	-	7	-	-	-	-	-	-	-	-	19	-	-	-
7	-	-	-	6	-	7	-	-	-	-	2	-	-	-	-	9	-	20	-	-	-	-	-	-	-	-	-	-	10	-	-
8	-	-	18	-	0	-	-	-	-	10	-	-	-	-	16	-	-	-	-	9	-	-	-	-	-	-	-	-	-	-	17
9	-	5	-	-	-	-	-	18	3	-	-	-	-	-	10	-	-	5	-	-	4	-	-	-	-	5	-	-	-	-	-	7
10	-	-	0	-	16	-	-	-	-	6	-	-	-	0	-	-	-	-	-	7	-	4	-	-	-	-	10	-	19	-	-
11	6	-	-	-	-	-	7	-	-	-	-	2	9	-	-	-	-	-	20	-	-	-	4	-	19	-	-	-	-	10	-
12	-	-	-	18	-	0	-	-	-	-	10	-	-	-	-	16	9	-	-	-	-	-	-	12	-	-	4	-	17	-	-	-
13	-	-	5	-	18	-	-	-	-	3	-	-	-	-	-	10	-	-	5	-	-	-	-	-	-	-	5	-	-	-	-	-
14	-	-	-	0	-	16	-	-	-	-	6	-	-	-	0	-	7	-	-	-	-	-	-	-	10	-	-	-	-	-	-	-
15	-	6	-	-	-	-	-	7	2	-	-	-	-	9	-	-	-	-	-	20	-	-	-	-	-	19	-	-	-	-	-	-
16	18	-	-	-	-	-	0	-	-	-	-	10	16	-	-	-	-	9	-	-	-	-	-	-	-	-	-	4	-	-	-	-

Figure A.4: Matrix permutation indexes of parity check matrix for LDPC(336,672) [2].

(672,504), Code rate: 3/4

	1	2	3	4	5	6	7	8	9	10	11	12	13	14	15	16	17	18	19	20	21	22	23	24	25	26	27	28	29	30	31	32
1	0	-	-	5	-	18	16	-	-	-	3	6	10	-	-	0	-	7	-	5	-	-	4	4	-	10	-	5	-	-	-	-
2	-	18	6	-	7	-	-	0	10	2	-	-	-	16	9	-	20	-	9	-	4	12	-	-	4	-	19	-	-	-	-	-
3	5	0	-	-	-	-	18	16	6	-	-	3	0	10	-	-	5	-	7	-	4	-	-	4	5	-	10	-	19	-	-	-
4	-	-	18	6	0	7	-	-	-	10	2	-	-	-	16	9	-	20	-	9	-	4	12	-	-	4	-	19	-	10	-	-
5	-	5	0	-	16	-	-	18	3	6	-	-	-	0	10	-	-	5	-	7	4	4	-	-	-	5	-	-	-	-	-	-
6	6	-	-	18	-	0	7	-	-	-	10	2	9	-	-	16	9	-	20	-	-	-	4	12	19	-	-	-	-	-	-	-
7	-	-	5	0	18	16	-	-	-	3	6	-	-	-	0	10	7	-	5	-	-	4	4	-	10	-	5	-	7	-	19	-
8	18	6	-	-	-	-	0	7	2	-	-	10	16	9	-	-	-	9	-	20	12	-	-	4	-	19	-	4	-	17	-	10

Figure A.5: Matrix permutation indexes of parity check matrix for LDPC(504,672) [2].

(672,588), Code rate: 7/8

	1	2	3	4	5	6	7	8	9	10	11	12	13	14	15	16	17	18	19	20	21	22	23	24	25	26	27	28	29	30	31	32
1	0	18	6	5	7	18	16	0	10	2	3	6	10	16	9	0	20	7	9	5	4	12	4	4	4	10	19	5	10	-	-	-
2	5	0	18	6	0	7	18	16	6	10	2	3	0	10	16	9	5	20	7	9	4	4	12	4	5	4	10	19	19	10	-	-
3	6	5	0	18	16	0	7	18	3	6	10	2	9	0	10	16	9	5	20	7	4	4	4	12	19	5	4	10	17	19	10	-
4	18	6	5	0	18	16	0	7	2	3	6	10	16	9	0	10	7	9	5	20	12	4	4	4	10	19	5	4	7	17	19	10

Figure A.6: Matrix permutation indexes of parity check matrix for LDPC(588,672) [2].

Appendix B

IEEE 802.15.3c: AV PHY parameters

B.1 HRP data rate

HRP mode index	Coding mode	Modulation	Inner code rate		Data rate (Gb/s)
			MSB	LSB	
			[7] [6] [5] [4]	[3] [2] [1] [0]	
0	EEP	QPSK	1/3		0.952
1		QPSK	2/3		1.904
2		16-QAM	2/3		3.807
3	UEP	QPSK	4/7	4/5	1.904
4		16-QAM	4/7	4/5	3.807
5	MSB-only retransmission	QPSK	1/3	N/A	0.952
6		QPSK	2/3	N/A	1.904

Figure B.1: HRP data rates and coding [2].

B.2 AV PHY layer modulation parameters

Parameter	Value	Symbol
Occupied bandwidth	1.76 GHz	N/A
Reference sampling rate	2.538 GHz	$f_{s(HR)}$
Number of subcarriers	512	$N_{sc(HR)}$
FFT period	$N_{sc(HR)}/f_{s(HR)} \sim 202$ ns	$T_{FFT(HR)}$
Subcarrier spacing	$1/T_{FFT(HR)} \sim 4.96$ MHz	$\Delta f_{SC(HR)}$
Guard interval	$64/f_{s(HR)} \sim 25.2$ ns	$T_{GI(HR)}$
Symbol duration	$T_{FFT(HR)} + T_{GI(HR)} \sim 227$ ns	$T_{S(HR)}$
Number of data subcarriers	336	$N_{dsc(HR)}$

Figure B.2: HRP modulation parameters [2].

Parameter	Value	Symbol
Occupied bandwidth	92 MHz	N/A
Reference sampling rate	317.25 MHz	$f_{s(LR)}$
Number of subcarriers	128	$N_{sc(LR)}$
FFT period	$N_{sc(LR)}/f_{s(LR)} \sim 403$ ns	$T_{FFT(LR)}$
Subcarrier spacing	$1/T_{FFT(LR)} \sim 2.48$ MHz	$\Delta f_{SC(LR)}$
Guard interval	$28/f_{s(LR)} \sim 88.3$ ns	$T_{GI(LR)}$
Symbol duration	$T_{FFT(LR)} + T_{GI(LR)} \sim 492$ ns	$T_{S(LR)}$
Number of data subcarriers	30	$N_{dsc(LR)}$

Figure B.3: LRP modulation parameters [2].

Appendix C

IEEE 802.15.3c: HSI PHY parameters

C.1 MCS dependent parameters

MCS index	Data rate (Mb/s)	Modulation scheme	Spreading factor (L_f)	Coding mode	FEC rate (R_{FEC})	
					msb 8b	lsb 8b
0	32.1	QPSK	48	EEP	1/2	
1	1540	QPSK	1		1/2	
2	2310	QPSK	1		3/4	
3	2695	QPSK	1		7/8	
4	3080	16-QAM	1		1/2	
5	4620	16-QAM	1		3/4	
6	5390	16-QAM	1		7/8	
7	5775	64-QAM	1		5/8	
8	1925	QPSK	1	UEP	1/2	3/4
9	2503	QPSK	1		3/4	7/8
10	3850	16-QAM	1		1/2	3/4
11	5005	16-QAM	1		3/4	7/8

Figure C.1: HSI PHY MCS dependent parameters [2].

C.2 Timing-related parameters

Parameters	Description	Value	Formula
f_s	Reference sampling rate/chip rate	2640 MHz	
T_C	Sample/chip duration	~0.38 ns	$1/f_s$
N_{sc}	Number of subcarriers/FFT size	512	
N_{dsc}	Number of data subcarriers	336	
N_P	Number of pilot subcarriers	16	
N_G	Number of guard subcarriers	141	
N_{DC}	Number of DC subcarriers	3	
N_R	Number of reserved subcarriers	16	
N_U	Number of used subcarriers	352	$N_{dsc} + N_P$
N_{GI}	Guard interval length in samples	64	
Δf_{sc}	Subcarrier frequency spacing	5.15625 MHz	f_s/N_{sc}
BW	Nominal used bandwidth	1815 MHz	$N_U \times \Delta f_{sc}$
T_{FFT}	IFFT and FFT period	~193.94 ns	$1/\Delta f_{sc}$
T_{GI}	Guard interval duration	~24.24 ns	$N_{GI} \times T_C$
T_S	OFDM Symbol duration	~218.18 ns	$T_{FFT} + T_{GI}$
F_S	OFDM Symbol rate	~4.583 MHz	$1/T_S$
N_{CPS}	Number of samples per OFDM symbol	576	$N_{sc} + N_{GI}$

Figure C.2: Timing-related parameters of HSI PHY [2].

C.3 Frame-related parameters

Parameter	Description	Value	
N_{pre}	Number of symbols in the PHY preamble (A preamble symbol is 512 chips long)	Long Preamble	16
		Short Preamble	6.75
T_{pre}	Duration of the PHY preamble	Long Preamble	~3.15 µs
		Short Preamble	~1.31 µs
T_{HDR}	Duration of the header	Main header only for MCS 0	~7.64 µs
		Main header only for MCS 1–11	~0.22 µs
		Main header and optional header for MCS 0	~17.89 µs
		Main header and optional header for MCS 1–11	~0.44 µs
N_{OSMF}	Number of OFDM symbols in the MAC frame body	variable	
T_{OSMF}	Duration of the MAC frame body	$N_{OSMF} \times T_S$	
N_{frame}	Number of OFDM symbols in the frame	$N_{pre} + N_{HDR} + N_{OSMF}$	
T_{frame}	Duration of the frame	$T_{pre} + T_{HDR} + T_{OSMF}$	

Figure C.3: Frame-related parameters of HSI PHY [2].

C.4 LDPC code matrix permutation indexes

	1	2	3	4	5	6	7	8	9	10	11	12	13	14	15	16	17	18	19	20	21	22	23	24	25	26	27	28	29	30	31	32
1	0	-	-	5	-	18	16	-	-	-	3	6	10	-	-	0	-	7	-	5	-	-	4	4	-	10	-	5	-	-	-	-
2	-	-	6	-	7	-	-	-	-	2	-	-	-	-	9	-	20	-	-	-	4	-	-	-	-	-	19	-	-	-	-	-
3	-	18	-	-	-	-	-	0	10	-	-	-	-	16	-	-	-	-	9	-	-	12	-	-	4	-	-	-	-	-	17	-
4	5	0	-	-	-	-	18	16	6	-	-	3	0	10	-	-	5	-	7	-	4	-	-	-	-	-	-	-	-	-	-	-
5	-	-	-	6	-	7	-	-	-	-	2	-	-	-	-	9	-	20	-	-	-	4	-	-	-	-	-	-	-	-	-	-
6	-	-	18	-	0	-	-	-	-	10	-	-	-	-	16	-	-	-	-	9	-	-	12	-	-	-	-	-	-	-	-	-
7	-	5	0	-	16	-	-	18	3	6	-	-	-	0	10	-	-	5	-	7	4	4	-	-	-	5	-	-	-	-	-	-
8	6	-	-	-	-	-	7	-	-	-	-	2	9	-	-	-	-	-	20	-	-	-	4	-	19	-	-	-	-	-	-	-
9	-	-	-	18	-	0	-	-	-	-	10	-	-	-	-	16	9	-	-	-	-	-	-	12	-	-	-	-	-	-	-	-
10	-	-	5	0	18	16	-	-	-	3	6	-	-	-	0	10	7	-	5	-	-	4	4	-	10	-	5	-	7	-	-	-
11	-	6	-	-	-	-	-	7	2	-	-	-	-	9	-	-	-	-	-	20	-	-	-	4	-	19	-	-	-	-	-	10
12	18	-	-	-	-	-	0	-	-	-	-	10	16	-	-	-	-	9	-	-	12	-	-	-	-	-	-	4	-	17	-	-

Figure C.4: Matrix permutation indexes of parity check matrix for LDPC(420,672) [2].

C.5 Constellation mapping

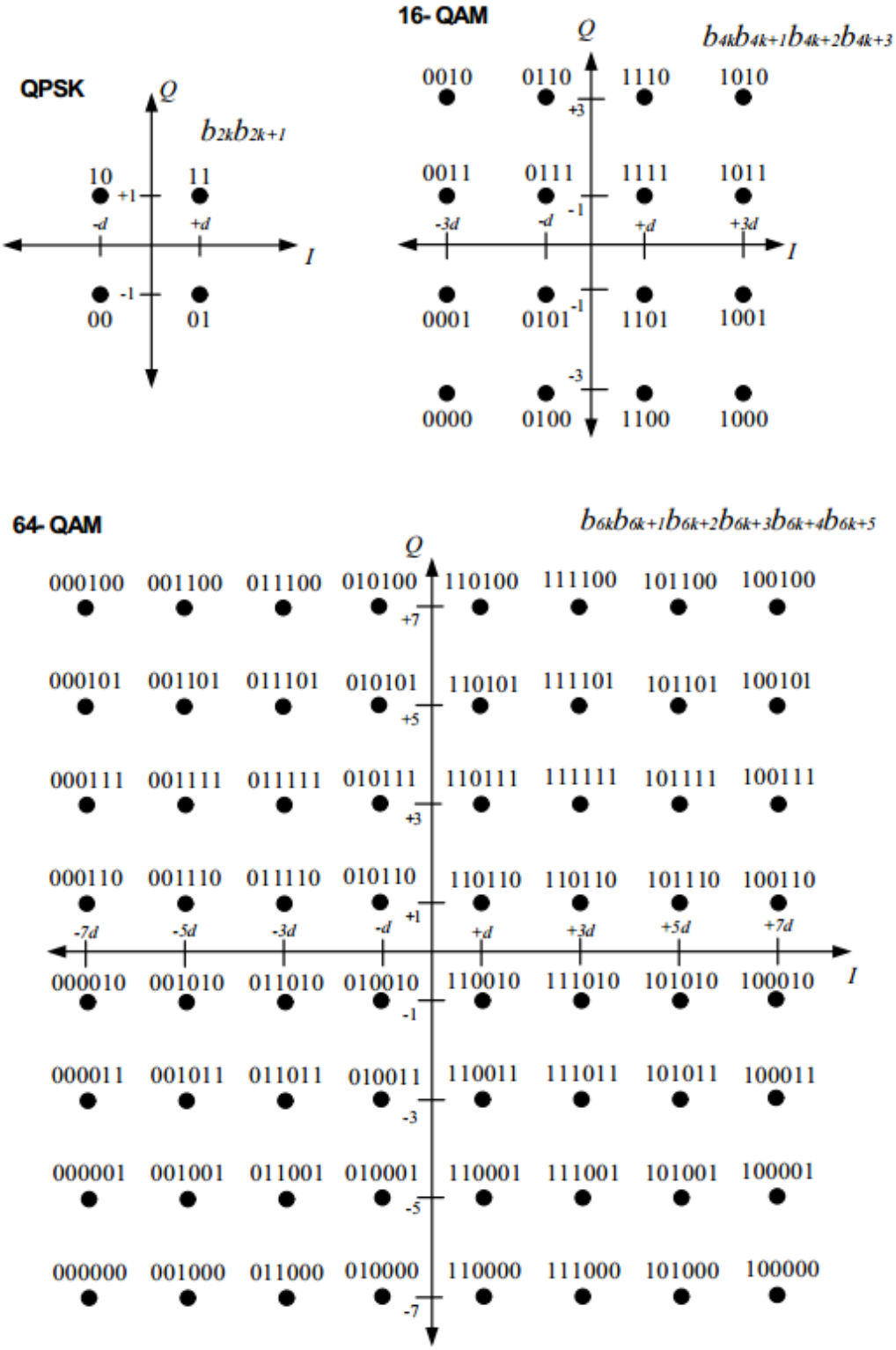

Figure C.5: Constellation bit encoding for HSI PHY layer [2].